ISRES Publishing

The Eurasia Proceedings of Science, Technology, Engineering & Mathematics

EPSTEM

VOLUME 18 ICBASET CONFERENCE

ISSN: 2602-3199

ISBN: 978-605-73797-9-5

ICBASET 2022: International Conference on Basic Sciences, Engineering and Technology (ICBASET)

August 25 - 28, 2022

Istanbul, Turkey

Edited by: Mehmet Ozaslan (Chair), Gaziantep University, Turkey

ICBASET 2022 OCTOBER

Volume 18, Pages 1-101 (October 2022)

The Eurasia Proceedings of Science, Technology, Engineering & Mathematics (EPSTEM)

e-ISSN: 2602-3199

Address: Istanbul C. Cengaver S. No 2 Karatay/Konya/TURKEY

Website: www.isres.org

Contact: isrespublishing@gmail.com

Conference: ICBASET2022: International Conference on Basic Sciences, Engineering and Technology (ICBASET)
Conference website: https://www.2022.icbaset.net
Dates: August 25 – 28, 2022
Location: Istanbul, Turkey
Edited by: Mehmet Ozaslan

About Editor(s)
Prof Dr. Mehmet Ozaslan
Department of Biology, Gaziantep University, Turkey
Website: http://mehmetozaslan.com/
Email: ozaslanmd@gantep.edu.tr

Language Editor(s)
Assoc. Prof. Dr. Kagan Buyukkarci
Department of English Language Education, Suleyman Demirel University, Turkey
Email: kaganbuyukkarci@sdu.edu.tr

ISSN: 2602-3199

Editorial Policies

ISRES Publishing follows the steps below in the procedings book publishing process.
In the first stage, the papers sent to the conferences organized by ISRES are subject to editorial oversight. In the second stage, the papers that pass the first step are reviewed by at least two

international field experts in the conference committee in terms of suitability for the content and subject area. In the third stage, it is reviewed by at least one member of the organizing committee for the suitability of references. In the fourth step, the language editor reviews the language for clarity.

Review Process

Abstracts and full-text reports uploaded to the conference system undergo a review procedure. Authors will be notified of the application results in three weeks. Submitted abstracts will be evaluated on the basis of abstracts/proposals. The conference system allows you to submit the full text if your abstract is accepted. Please upload the abstract of your article to the conference system and wait for the results of the evaluation. If your abstract is accepted, you can upload your full text. Your full text will then be sent to at least two reviewers for review. **The conference has a double-blind peer-review process.** Any paper submitted for the conference is reviewed by at least two international reviewers with expertise in the relevant subject area. Based on the reviewers' comments, papers are accepted, rejected or accepted with revision. If the comments are not addressed well in the improved paper, then the paper is sent back to the authors to make further revisions. The accepted papers are formatted by the conference for publication in the proceedings.

Aims & Scope

Engineering, technology and basic sciences are closely related fields. Developments and innovations in one of them affect the others. Therefore, **the focus of the conference** is on studies related to these three fields. Studies in the fields of engineering, technology and basic science are accepted to the conference even if they are not associated with other fields. The conference committee thinks that a study in only one field (for example, mathematics, physics, etc.) will contribute to other fields (for example, engineering, technology, etc.) in future studies, even if it is not associated with the presentation at the conference. In line with this perspective, studies in the following fields are accepted to the conference: *Biology, Chemistry, Engineering, Mathematics, Physics and Technology*.
The aim of the conference is to bring together researchers and administrators from different countries, and to discuss theoretical and practical issues in all fields of Engineering, Technology and Basic Sciences.

Articles: 1-12

CONTENTS

The Eurasia Proceedings of
Science, Technology, Engineering & Mathematics (EPSTEM)
ISSN: 2602-3199

The Eurasia Proceedings of Science, Technology, Engineering & Mathematics (EPSTEM)
ISSN: 2602-3199

The Eurasia Proceedings of Science, Technology, Engineering & Mathematics (EPSTEM), 2022

Volume 18, Pages 1-6

ICBASET 2022: International Conference on Basic Sciences, Engineering and Technology

Data Analytic for Cyber Security: A Review of Current Framework Solutions, Challenges and Trends

Shereen KHAN
Multimedia University

Tan Swee Leng OLIVIA
Multimedia University

Nasreen KHAN
Multimedia University

Ng Kok WHY
Multimedia University

Tan Swee WEI
Multimedia University

Abstract: In context of technology, cybersecurity has seen vital technological and operational developments in recent years, with information science at the forefront of the revolution. The key in creating a complicated and automatic security system is extracting network activity patterns or cybersecurity information insights and constructing an identical data-driven model. The applying of a spread of scientific methodology, machine learning techniques, processes, and systems; information science is to grasp and analyse actual occurrences with information. During this analysis, the researchers consider and in short justify cybersecurity information science, during which information is obtained from relevant cybersecurity sources as well as legislations and analytics are wont to supplement the most recent data-driven trends to supply more practical security solutions. The paradigm of cybersecurity information science, in distinction to standard cybersecurity computing techniques, permits for more practical and complex computing. Researchers check and highlight variety of connected analysis topics and future directions. Additionally, researchers propose a multi-layered framework for cybersecurity modelling. Overall the target is to target the connection of data-driven deciding framework model for safeguarding systems from cyber-attacks, instead of simply discussing cybersecurity information science and applicable approaches.

Keywords: Cyber security, cybercrime, data analytic, legislations

Introduction

Data analytics is a strategy for ensuring accurate data analysis, cleansing, altering, and modelling via the application of proper analysis. Data analysis aids in the discovery of important nuances and leads to a positive outcome. Cybercrime is now a factor in all projects, as part of Malaysia's National Policy on Industry 4.0, which aims to improve the country's industrial capacity by enacting appropriate legislation to combat the use of ICTs for illegal purposes. Assuming that the cybercrime data is thoroughly investigated, the outcome might be quickly concluded, allowing better judgments to be made about combating cybercriminals through appropriate laws. Cybercrime is sometimes confused with a presentation that focuses solely on computers and the internet. However, not all cybercrime is limited to computers and the internet; for example, the instance of Joseph Marie

- Selection and peer-review under responsibility of the Organizing Committee of the Conference

Jacquard and another common model would be dumpster diving , which is a tactic for recovering data that might be used to launch an attack on a computer network. Their presentation includes not just scanning the trash for valuables, but also getting access and a secret key written on scribbled notes (Lew, 2020).

Vizom is a popular video conferencing programme that is now important to companies and social life as a result of the coronavirus outbreak (Brewer, 2021). The danger with such attacks is that they can eventually lead to a cascade breakdown of interbank finance, perhaps sparking a bigger systemic liquidity crisis. In all of these circumstances, the companies' activities are so linked with those of other organisations in their respective countries that their collapse will certainly cause those other or connected businesses to fail as well. As a result, protecting such infrastructures, also known as key information infrastructures, is considered a national security concern.

Background of the study

Cyber-attacks are frequently in the news, posing a security risk to governments, sectors, and enterprises. Things might grow even worse with society's dependency on technology and the emergence of the internet of things. As seen by the devastating malware they employ to target enterprises, cyber thieves are becoming more intelligent and sophisticated.

This paper focuses on the current tend challenges of data analytic on cybersecurity in Malaysia and Malaysia is chosen to be the country for this research due to its strategic economic geographical location and Malaysia has been classified among the top ten nations with a strong commitment to cybersecurity in the International Telecommunications Union's Global Cybersecurity Index 2020 study (ITU). Malaysia faces many challenges in defending its cybersecurity domain. The information was gathered through interviews with experts in the field of cybersecurity. The findings indicated that in order to incorporate a cybersecurity aspect in the organisation, awareness and funding are critical. Due to the Prime Minister's digital economy blueprint, YAB Tan Sri Dato' Haji Mahiaddin container Haji Mohd, Yassin in 2021, a substantial increase in cyberisation would be 81 percent of Malaysians are now dynamic via web-based media in 2020, and 90 percent of government is now online (Mok, 2021). Simultaneously, concerns about cyber security approaches on advancement toward administrative arrangements command and updating outdated legislation are needed to provide robustness in combating cyber-attacks as Malaysia's cyberization progresses.

Literature Review

Industry 4.0 offers great benefits to businesses in terms of long-term viability. Internet of things, big data, supply chain, cloud computing, horizontal and vertical integration, autonomous robot, addictive manufacturing, cyber security, simulation, and augmented reality are the nine pillars in total. However, cyber security is the most significant problem in this digitalization era. The privacy and security of data will always be top security priorities for every firm.

All individuals, professionals, legislators, and, more broadly, all decision makers are concerned about cybersecurity. It has also become a big problem for societies that must protect itself against cyber-attacks using both preventative and reactive methods, which include a lot of monitoring, while still preserving their independence and avoiding widespread surveillance. Computer security, often known as cyber security or IT security, is the safeguarding of computer systems against harm to their hardware, software, or information, as well as disruption or misdirection of services they offer (Roca , 2019). Data integrity is a challenge in cyber security management. Due to the vast amount of information and data, securing data integrity in an IoT context has proven to be rather difficult. Data from many sources has a wide range of ideas and forms, making it challenging for analysts to combine it. Furthermore, a lack of monitoring and security against unauthorised modifications or alteration will result in undesirable data alterations. During peak hours, when enterprises may lack the internal competence and systems to manage and safeguard data, malicious data searchers are continually seeking for new methods to steal it (Campos et al., 2016).

Cybersecurity Data Analytic

The ultimate objective of cybersecurity data science is to use security data to make data-driven intelligent decisions for smart cybersecurity solutions. Cybersecurity data represents a partial paradigm change away from old well-known security solutions like firewalls, user authentication and access control, encryption systems, and so on, which may or may not be successful in today's cyber business. The issues are that these are often handled statically by a few competent security analysts, with ad-hoc data management.

However, as the frequency of cybersecurity events in the various forms indicated above continues to rise, traditional solutions have proven ineffective in managing such cyber dangers. As a result, a large number of complex assaults are developed and disseminated swiftly throughout the Internet. Although several researchers use various data analysis and learning techniques to build cybersecurity models, as summarised in the section "Framework model in cybersecurity," a comprehensive security model based on the effective discovery of security insights and latest security patterns may be more useful. To overcome this problem, we need to create more flexible and efficient security systems that can respond to attacks and change security rules in a timely manner to mitigate them intelligently.

Table 1. Statistics on types of cybercrime in Malaysia 2022

	January	February	March	April	May	June	July	August	September	October	November	December	Total
Spam	8	5	6	15	0	0	0	0	0	0	0	0	34
Intrusion Attemp	15	12	4	6	0	0	0	0	0	0	0	0	37
Vulnerabilities Report	6	3	3	4	0	0	0	0	0	0	0	0	16
Malicious Codes	62	68	174	103	0	0	0	0	0	0	0	0	407
Content Related	2	0	0	2	0	0	0	0	0	0	0	0	4
Denial of Service	0	2	1	1	0	0	0	0	0	0	0	0	4
Intrusion	68	54	50	74	0	0	0	0	0	0	0	0	246
Fraud	431	423	388	396	0	0	0	0	0	0	0	0	1638
	592	567	626	601	0	0	0	0	0	0	0	0	2386

Table 1, data indicates the statistic on types of cybercrimes in Malaysia 2022. In order to analyse the data coherently to reflect the accuracy, it is necessary to evaluate a large quantity of important cybersecurity data collected from many sources, such as network and system sources, and to identify insights or correct security policies in an automated way with little human interaction. Analyzing cybersecurity data and developing the necessary tools and methods to effectively guard against cybersecurity events entails more than a basic set of functional requirements and understanding of risks, threats, and vulnerabilities.

Proposed framework to safeguard data analytic for cybersecurity

As previously stated, cybersecurity data science is data-driven, employs machine learning techniques, attempts to quantify cyber risks, employs inferential techniques to analyse behavioural patterns, focuses on generating security response alerts, and ultimately seeks to optimise cybersecurity operations. As a result, the researchers briefly explain a layered data processing architecture that can be utilised to extract security insights from raw data and develop smart cybersecurity systems, such as dynamic policy rule-based access control or intrusion detection and prevention systems.

Collecting relevant cybersecurity data is a critical stage that serves as a link between cyber infrastructure security issues and data-driven solution processes in this methodology. As a result, the question is how to gather relevant and unique requirements data in order to construct data-driven security models. A strict framework, such as proposed policies and legislations, should play an essential role in safeguarding pure cybersecurity data for analysis.

This layer in this framework is responsible for finalising the resulting security model by including new intelligence as needed. This might be accomplished by additional processing in numerous modules, such as recency mining and security model updating, which is responsible for keeping the security model up-to-date for improved performance by extracting the most recent data-driven security patterns.

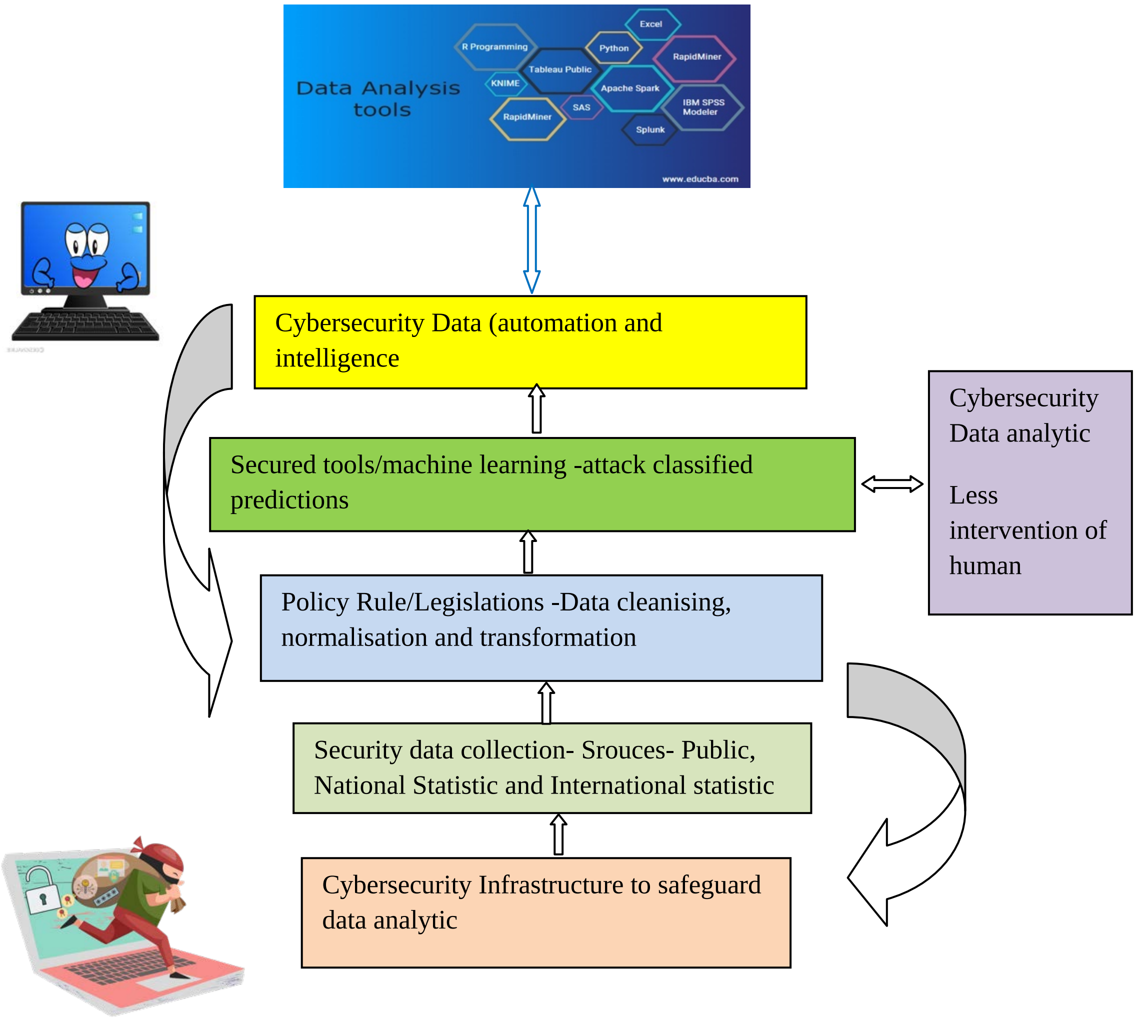

Figure 1. Cybersecurity layered data processing architecture framework

Results and Discussion

Data from computer networks, telecommunication networks, banking, healthcare, social media networks, bioinformatics, E-Commerce, surveillance, and other sources are some of the most common sources of big data transactions. The absence of security software that can be upgraded for protection is the next issue (Yaaqob et al., 2017). Due to a scarcity of equipment, tools, and systems, this is the case. An organization's software upgradeability is also expensive. On the one hand, most businesses are unable to organise unstructured data (Campos et al., 2016).

From the proposed framework in Fig.1, it is predicted that with this high level proposed data cleaning , normalisation and a comprehensive policy and legislation in place, the cybersecurity of Malaysia will be fully protected and moreover data-driven intelligent decision making in smart cybersecurity systems and services is what cybersecurity data science is all about.

Conclusion

Finally, the researchers have emphasised the current state of the art difficulties confronting the cybersecurity area in the face of data analytics. Traditional security solutions, employing traditional tools and methodologies, are no longer capable of embracing real-time large data network streams. Security analytics, or the use of structured data analytics to derive actionable knowledge and insights from streams in real time while adhering to governing rules, has been demonstrated by researchers to be a growing necessity for cybersecurity installations. Although the present usage of analytical solutions is far from revolutionary (as demonstrated by this Teradata research from 2013), awareness of adoption is gradually growing.

Recommendations

The discussion of this research was centred on two objectives: (1) analysing Malaysia's cyber security difficulties, and (2) proposing a holistic cybersecurity data analysis methodology for Malaysia to address cyber security challenges. Although Malaysia has cyberlaws in place to combat cybersecurity breaches, such as the Computer Crimes Act 1997, the Communications and Multimedia Act 1998, the Penal Code,the National Cyber Security Agency (NACSA) and the Malaysia CyberSecurity Strategy 2020-2024 , the topic of cybercrime and cyber security is still very popular, and free data sets for analysis in this field are still scarce. Data analysis for cybersecurity will be more accurate to forecast and prevent cybercrime in Malaysia if more data in this industry becomes available and extracted with minimal human interaction.

Scientific Ethics Declaration

The authors declare that the scientific ethical and legal responsibility of this article published in EPSTEM journal belongs to the authors.

Acknowledgements or Notes

This article was presented as an oral presentation at the International Conference on Basic Sciences, Engineering and Technology (www.icbaset.net) conference held in Istanbul/Turkey on August 25-28, 2022.

*This research is funded by the Malaysian Ministry of Education (MOE) through the Fundamental Research Grant Scheme (FRGS) FRGS/1/2019/SSI10/MMU/03/15. The authors alone are responsible for the views expressed in this article, which does not necessarily represent the views, decisions, or policies of MOE or the institutions with which the authors are affiliated. The funder had no role in study design, data collection and analysis, or preparation of the manuscript.

References

Brewer, R. (2015). Cyber threats: reducing the time to detection and response. *Network Security*, *5*, pp.5-8.

Communications and Multimedia Act (1998). *National Cyber Security Agency (NACSA)*. https://www.nacsa.gov.my/

Malaysia CyberSecurity Strategy 2020-2024 Compressed.pdf https://asset.mkn.gov.my/web/wp-content/uploads/sites/3/2019/08/MalaysiaCyberSecurityStrategy2020-2024Compressed.pdf

Global Cybersecurity Index (2020). https://www.itu.int/en/ITU-D/Cybersecurity/Pages/global-cybersecurity-index.aspx

Campos, J., Sharma, P., Jantunen, E., Baglee, D., & Fumagalli, L. (2016). The challenges of cybersecurity frameworks to protect data required for the development of advanced maintenance. *Procedia Cirp, 47*, 222-227.

Lew, H. (2020, January 29). *Why malaysia should amend its cyber security laws*. Asia Law Portal

Mok, O. (2021, February 19). *MyDIGITAL and Malaysia digital economy blueprint: how we can achieve 100pc internet access.* Malaysia | Malay Mail

Roca, S. K.-L.-D.-V. (2019). Cybersecurity current challenges and Inria's research directions. *Le Chesnay Cedex, France: Inria*

Teradata and Ponemon Institute (2013). Big data analytics in cyber defense, February. http://www.ponemon.org/local/upload/file/Big_Data_Analytics_in_Cyb er_Defense_V12.pdf

Yaqoob, I., Ahmed, E., ur Rehman, M. H., Ahmed, A. I. A., Al-garadi, M. A., Imran, M., & Guizani, M. (2017). The rise of ransomware and emerging security challenges in the Internet of Things. *Computer Networks, 129*, 444-458.

Author Information

Shereen Khan
Multimedia University
Persiaran Multimedia , Cyberjaya 63100, Selangor, Malaysia
Contact e-mail:*shereen.khan@mmu.edu.my*

Tan Swee Leng Olivia
Multimedia University
Jalan Ayer Keroh Lama, 75450 Bukit Beruang, Melaka, Malaysia

Nasreen Khan
Multimedia University, Malaysia
Persiaran Multimedia , Cyberjaya 63100, Selangor, Malaysia

Ng Kok Why
Multimedia University, Malaysia
Persiaran Multimedia , Cyberjaya 63100, Selangor, Malaysia

Swee Wei Tan
Multimedia University
Persiaran Multimedia , Cyberjaya 63100, Selangor, Malaysia

To cite this article:

Khan, S., Olivia, T.S.L., Khan, N., Why, N.K. & Tan, S. W. (2022). Data analytic for cyber security: a review of current framework solutions, challenges and trends. *The Eurasia Proceedings of Science, Technology, Engineering & Mathematics (EPSTEM), 18,* 1-6.

The Eurasia Proceedings of Science, Technology, Engineering & Mathematics (EPSTEM)
ISSN: 2602-3199

The Eurasia Proceedings of Science, Technology, Engineering & Mathematics (EPSTEM), 2022

Volume 18, Pages 7-15

ICBASET 2022: International Conference on Basic Sciences, Engineering and Technology

On a Geometric Programming Approach to Profit Maximization: The Case of CES Technology

Vedran KOJIĆ
University of Zagreb

Abstract: The profit maximization problem takes a central place in the theory of the firm, especially when conditions for perfect competition hold. In this paper, we solve the profit maximization problem of a perfectly competitive firm when the constant elasticity of substitution (CES) production function with $n \geq 2$ inputs describes its technology. Commonly, this problem is solved by using multivariable differential calculus. However, to avoid tedious algebraic manipulations and bypass checking nontrivial necessary and sufficient conditions, we employ geometric programming (GP), and the power mean inequality (PMI) as an elegant complementary tool to multivariable calculus. Since the GP and the PMI are simple optimization techniques without derivatives, they can provide new insights into the given problem to managers, students, and other audiences who may be unfamiliar with multivariable differential calculus. Additionally, by using the properties of limits, we show that the solution to the profit maximization problem with Cobb-Douglas technology is a limiting case of our result.

Keywords: Profit maximization, Cobb-Douglas technology, CES technology, Geometric programming

Introduction

Since finding the optimum using differential calculus may be nontrivial and inelegant, the signomial geometric programming (SGP) technique with zero degrees of difficulty was proposed by (Liu, 2006) as a complementary approach to solving the profit maximization problem with Cobb-Douglas production function (CDPF). Further, (Kojić & Lukač, 2018) showed how the results from (Liu, 2006) can be obtained by solving an equivalent geometric programming (GP) problem with zero degrees of difficulty, providing proof that the (global) maximum profit in the case of CDPF has been achieved.

In this note, we solve a profit maximization problem where the firm's technology is given by the CES production function (CESPF). Furthermore, since the CESPF is a generalization of the CDPF, we show how the results by (Liu, 2006) and (Kojić & Lukač, 2018) can be derived from our results.

The paper is organized as follows. After the introduction, the notation and preliminaries are presented in the second section. The solution to the profit maximization problem with CESPF is the main result of the paper and it is given in the third section. The fourth section shows that the solution to the profit maximization problem with CDPF is a limiting case of our result. The fifth section concludes the paper.

Notations and preliminaries

Notations have been adopted from (Avvakumov et al., 2010), (Jehle & Reny, 2011), and (Liu, 2006):

- Selection and peer-review under responsibility of the Organizing Committee of the Conference

p	market price per unit, $p>0$
A	scale of production, $A>0$
x_i	input quantities, $x_i>0$
v_i	input prices, $v_i>0$ for all i
φ_i	elasticities of Cobb-Douglas production function (CDPF) $\varphi_i>0$ for all i
x_i^{C-D}	the i^{th} component of the maximizer
$\pi^{C\text{-}D}$	maximum profit in the case of CDPF (i.e. Cobb-Douglas technology)
α_i	allocation coefficients of CES production function (CESPF, i.e. CES technology), $\alpha_i>0$ for all i
σ	degree of homogeneity of CESPF
ρ	substitution coefficient of CESPF
x_i^{CES}	the i^{th} component of the maximizer
π^{CES}	maximum profit in the case of CESPF

Considering CDPF with n inputs ($n\geq2$), given by

$$f\left(x_1, x_2, \ldots, x_n\right) = A\prod_{i=1}^{n} x_i^{\varphi_i} \ , \tag{1}$$

the profit maximization problem becomes

$$\pi^{C-D} = \max_{x_1, x_2, \ldots, x_n > 0} p\left(A\prod_{i=1}^{n} x_i^{\varphi_i}\right) - \sum_{i=1}^{n} v_i x_i \ , \tag{2}$$

where

$$\sum_{i=1}^{n} \varphi_i < 1 \, . \tag{3}$$

By using SGP, (Liu, 2006) obtained the result of problem (2) as follows:

$$\pi^{C-D} = \left(1 - \sum_{i=1}^{n} \varphi_i\right)\left(pA\right)^{1\left/\left(1-\sum_{i=1}^{n}\varphi_i\right)\right.} \prod_{i=1}^{n}\left(\frac{v_i}{\varphi_i}\right)^{-\varphi_i\left/\left(1-\sum_{i=1}^{n}\varphi_i\right)\right.} , \tag{4}$$

$$x_i^{C-D} = \frac{\pi^{C-D}\varphi_i}{v_i\left(1-\sum_{j=1}^{n}\varphi_j\right)} \, , \tag{5}$$

for all i=1, 2, …, n. However, problem (2) can be converted into a GP problem with zero degrees of difficulty, and the same result (4)-(5) was obtained by (Kojić & Lukač, 2018).
Now, let us introduce CESPF as in (Avvakumov et al., 2010), defined by

$$\psi\left(x_1, x_2, \ldots, x_n\right) = A\left(\sum_{i=1}^{n} \alpha_i x_i^{-\rho}\right)^{-\sigma/\rho} \ , \tag{6}$$

Where

$$\sum_{i=1}^{n} \alpha_i = 1 \, , \tag{7}$$

$$\sigma > 0 \, , \tag{8}$$

$$\rho > -1, \ \rho \neq 0 \, . \tag{9}$$

Considering CESPF, the profit maximization problem of a perfectly competitive firm with CES technology becomes (Jehle & Reny, 2011):

$$\pi^{CES} = \max_{y,x_1,x_2,\ldots,x_n>0} py - \sum_{i=1}^{n} v_i x_i$$
$$\text{s.t. } A\left(\sum_{i=1}^{n} \alpha_i x_i^{-\rho}\right)^{-\sigma/\rho} \geq y. \tag{10}$$

To solve (10), we will use a power mean inequality (see (Bullen, 2003)).

Lemma 1. (Power mean inequality) Let $n\geq 2$, $n\in\mathbb{N}$, $x_i>0$, and $w_i>0$, $i=1, 2, \ldots, n$, such that $w=\sum_{i=1}^{n} w_i$. Then, for all $r>0$, the following inequality holds

$$\prod_{i=1}^{n} x_i^{w_i} \leq \left(\sum_{i=1}^{n} \frac{w_i}{w} x_i^r\right)^{w/r}. \tag{11}$$

Equality in (11) holds if and only if $x_1=x_2=\ldots=x_n$.

The profit maximization problem with CES technology

Since the very discovery of geometric programming, it has been applied to various optimization problems in science and industry. In the economic theory of production, (Reklaitis et al., 1975) applied geometric programming to solve the firm's cost minimization problem with Cobb-Douglas and CES production functions. Mainly, they used power mean inequality in solving the cost minimization problem with CESPF using geometric programming. However, they didn't comment on the sign of the substitution coefficient ρ, which makes their analysis incomplete.

Another important problem in the theory of the firm is the profit maximization problem for the perfectly competitive firm. The profit maximization problems with Cobb-Douglas and CES production function and their solutions are very well known in the literature (Zevelev, 2014). These problems are usually solved using multivariable calculus (Avvakumov et al., 2010). Still, a geometric programming approach to the profit maximization problem with CESPF is the main result of this paper since, to the best of our knowledge, such an approach is unknown in the literature.

According to (Duffin et al., 1967), (Beightler & Philips, 1976) and (Boyd et al., 2007), problem (10) is equivalent to the following problem:

$$\max_{z,y,x_1,\ldots,x_n>0} \quad z \tag{12}$$

$$\text{s.t.} \quad py - \sum_{i=1}^{n} v_i x_i \geq z, \tag{13}$$

$$A\left(\sum_{i=1}^{n} \alpha_i x_i^{-\rho}\right)^{-\sigma/\rho} \geq y. \tag{14}$$

Since max f = 1/(min (1/f)) for a positive function f, instead of the problem (12)-(14) we will solve the problem (15)-(17):

$$\min_{z,y,x_1,\ldots,x_n>0} \quad z^{-1} \tag{15}$$

$$\text{s.t.} \quad p^{-1}y^{-1}z + \sum_{i=1}^{n} p^{-1} v_i x_i y^{-1} \leq 1, \tag{16}$$

$$A\left(\sum_{i=1}^{n} \alpha_i x_i^{-\rho}\right)^{-\sigma/\rho} \geq y. \tag{17}$$

Let us consider two cases regarding the value of the substitution coefficient of CESPF ρ from (9).

Case 1. ρ>0

Since the degree of homogeneity σ is defined as a positive number (see (8)), and when $\rho>0$, the function $x \mapsto x^{-\rho/\sigma}$ is decreasing (for all $x>0$). In this case, the inequality (17) is equivalent to

$$A^{-\frac{\rho}{\sigma}}\left(\sum_{i=1}^{n}\alpha_i x_i^{-\rho}\right) \le y^{-\frac{\rho}{\sigma}} \;\Leftrightarrow\; \sum_{i=1}^{n} A^{-\frac{\rho}{\sigma}}\alpha_i x_i^{-\rho} y^{\frac{\rho}{\sigma}} \le 1, \tag{18}$$

which transforms the problem (15)-(17) into a GP problem (15)-(16) and (18) written in standard form. According to (Boyd et al., 2007) and (Duffin et al., 1967), the corresponding dual of (15)-(16) and (18) is the following problem:

$$M = \max_{\substack{\beta,\gamma,\delta_i,\varepsilon_i>0\\ i=1,2,\dots,n}} \left(\frac{1}{\beta}\right)^{\beta}\cdot\left(\frac{p^{-1}}{\gamma}\right)^{\gamma}\cdot\prod_{i=1}^{n}\left(\left(\frac{p^{-1}v_i}{\delta_i}\right)^{\delta_i}\left(\frac{A^{-\rho/\sigma}\alpha_i}{\varepsilon_i}\right)^{\varepsilon_i}\right)\cdot\left(\gamma+\sum_{i=1}^{n}\delta_i\right)^{\gamma+\sum_{i=1}^{n}\delta_i}\cdot\left(\sum_{i=1}^{n}\varepsilon_i\right)^{\sum_{i=1}^{n}\varepsilon_i}, \tag{19}$$

s.t. $\beta=1$

$$\begin{bmatrix} -1 & 1 & 0 & 0 & \cdots & 0 & 0 & 0 & \cdots & 0\\ 0 & -1 & -1 & -1 & \cdots & -1 & \rho/\sigma & \rho/\sigma & \cdots & \rho/\sigma\\ 0 & 0 & 1 & 0 & \cdots & 0 & -\rho & 0 & \cdots & 0\\ 0 & 0 & 0 & 1 & \cdots & 0 & 0 & -\rho & \cdots & 0\\ \vdots & \vdots & \vdots & \vdots & \ddots & \vdots & \vdots & \vdots & \ddots & \vdots\\ 0 & 0 & 0 & 0 & \cdots & 1 & 0 & 0 & 0 & -\rho \end{bmatrix}_{(n+2)\times(2n+2)} \cdot \begin{bmatrix}\beta\\ \gamma\\ \delta_1\\ \vdots\\ \delta_n\\ \varepsilon_1\\ \vdots\\ \varepsilon_n\end{bmatrix}_{(2n+2)\times 1} = \mathbf{0}, \tag{20}$$

where a null vector **0** in (20) has $n+2$ components, and $\beta>0$, $\gamma>0$, $\delta_i>0$, $\varepsilon_i>0$, $i = 1, 2, \dots, n$, are dual variables. From (20) we get

$$\beta=\gamma=1, \tag{21}$$

$$\varepsilon_i=\frac{\delta_i}{\rho},\; i=1,2,\dots,n, \tag{22}$$

$$\sum_{i=1}^{n}\delta_i=\frac{\sigma}{1-\sigma}, \tag{23}$$

$$\sum_{i=1}^{n}\varepsilon_i=\frac{\sigma}{\rho(1-\sigma)}. \tag{24}$$

Note that from (8), (23) and the positivity of dual variables, it follows that the degree of homogeneity of CESPF must satisfy the following condition:

$$0<\sigma<1. \tag{25}$$

Furthermore, using (21)-(24), (19)-(20) becomes an unconstrained maximization problem

$$M = \max_{\substack{\delta_i>0\\ i=1,2,\dots,n}} \left(\frac{p^{-1}A^{-1}}{1-\sigma}\right)^{\frac{1}{1-\sigma}}\left(\frac{\sigma}{1-\sigma}\right)^{\frac{\sigma}{\rho(1-\sigma)}}\prod_{i=1}^{n}\left(\frac{v_i\alpha_i^{1/\rho}}{\delta_i^{(\rho+1)/\rho}}\right)^{\delta_i}. \tag{26}$$

Let us solve (26) by using Lemma 1. Let

$$x_i = \frac{v_i \alpha_i^{1/\rho}}{\delta_i^{(\rho+1)/\rho}}, \ \ w_i = \delta_i, \ \ i = 1, 2, ..., n, \tag{27}$$

$$w = w_1 + w_2 + \cdots + w_n = \sum_{i=1}^{n} \delta_i \overset{(23)}{=} \frac{\sigma}{1-\sigma}. \tag{28}$$

According to (11), for all r>0, the following inequality holds

$$\prod_{i=1}^{n} \left(\frac{v_i \alpha_i^{1/\rho}}{\delta_i^{(\rho+1)/\rho}} \right)^{\delta_i} \overset{(11)}{\leq} \left(\sum_{i=1}^{n} \frac{\delta_i}{\delta_1 + \cdots \delta_n} \left(\frac{v_i \alpha_i^{1/\rho}}{\delta_i^{(\rho+1)/\rho}} \right)^{r} \right)^{\frac{\delta_1 + \cdots \delta_n}{r}} = \left(\frac{1-\sigma}{\sigma} \right)^{\frac{\sigma}{r(1-\sigma)}} \left(\sum_{i=1}^{n} \left(v_i \alpha_i^{1/\rho} \right)^{r} \delta_i^{1 - r \cdot \frac{\rho+1}{\rho}} \right)^{\frac{\sigma}{r(1-\sigma)}}. \tag{29}$$

By choosing r=ρ/(ρ+1), the right-hand side of (29) becomes the constant. Thus, from (26) and (29), we get

$$\left(\frac{p^{-1} A^{-1}}{1-\sigma} \right)^{\frac{1}{1-\sigma}} \left(\frac{\sigma}{1-\sigma} \right)^{\frac{\sigma}{\rho(1-\sigma)}} \prod_{i=1}^{n} \left(\frac{v_i \alpha_i^{1/\rho}}{\delta_i^{(\rho+1)/\rho}} \right)^{\delta_i} \leq \left(\frac{p^{-1} A^{-1}}{1-\sigma} \right)^{\frac{1}{1-\sigma}} \left(\frac{\sigma}{1-\sigma} \right)^{\frac{-\sigma}{1-\sigma}} \left(\sum_{i=1}^{n} v_i^{\frac{\rho}{\rho+1}} \alpha_i^{\frac{1}{\rho+1}} \right)^{\frac{(\rho+1)\sigma}{\rho(1-\sigma)}}. \tag{30}$$

Equality in (29)-(30) holds if and only if

$$\frac{v_i \alpha_i^{1/\rho}}{\delta_i^{(\rho+1)/\rho}} = \frac{v_1 \alpha_1^{1/\rho}}{\delta_1^{(\rho+1)/\rho}}, \ \ i = 1, 2, ..., n. \tag{31}$$

From (23) and (31) we get

$$\delta_i = \frac{\frac{\sigma}{1-\sigma} v_i^{\frac{\rho}{\rho+1}} \alpha_i^{\frac{1}{\rho+1}}}{\sum_{j=1}^{n} v_j^{\frac{\rho}{\rho+1}} \alpha_j^{\frac{1}{\rho+1}}}. \tag{32}$$

Thus, by definition of the strict global optimum, the strict global maximum M of (26), and at the same time of (19), is equal to the right-hand side of (30), and it is achieved if and only if δ_i, i=1,2,…,n, satisfy (32). In addition, M represents the strict global minimum of (15)-(17). Furthermore, since max f = 1/(min (1/f)) for a positive function f, we can find π^{CES} from (10) via (12)-(17) as follows:

$$\pi^{CES} = M^{-1} = \left(pA(1-\sigma) \right)^{1/(1-\sigma)} \left(\frac{\sigma}{1-\sigma} \right)^{\frac{\sigma}{1-\sigma}} \left(\sum_{i=1}^{n} v_i^{\frac{\rho}{1+\rho}} \alpha_i^{\frac{1}{1+\rho}} \right)^{\frac{-(1+\rho)\sigma}{\rho(1-\sigma)}}. \tag{33}$$

According to (Duffin et al., 1967), from (15)-(18) and (21)-(24), we have

$$z^{-1} = \beta M = M \ \ \Rightarrow \ \ z = M^{-1}, \tag{34}$$

$$p^{-1} y^{-1} z = \frac{\gamma}{\gamma + \sum_{j=1}^{n} \delta_j} = \frac{1}{1 + \sum_{j=1}^{n} \delta_j}, \tag{35}$$

$$p^{-1} v_i x_i y^{-1} = \frac{\delta_i}{\gamma + \sum_{j=1}^{n} \delta_j}, \ i = 1, 2, ..., n, \tag{36}$$

$$A^{-\rho/\sigma} \alpha_i x_i^{-\rho} y^{\rho/\sigma} = \frac{\varepsilon_i}{\sum_{j=1}^{n} \varepsilon_j}, \ i = 1, 2, ..., n, \tag{37}$$

from where we get

$$x_i^{CES} = \frac{\frac{\sigma}{1-\sigma}\left(\frac{\alpha_i}{v_i}\right)^{\frac{1}{\rho+1}}}{\sum_{k=1}^{n} v_k^{\frac{\rho}{\rho+1}} \alpha_k^{\frac{1}{\rho+1}}} \cdot \pi^{CES},\ i = 1, 2, \ldots, n\,. \tag{38}$$

Thus, the strict global maximum of the profit maximization problem with CES technology π^{CES} is given by (33), and it is achieved for the input values given by (38).

Case 2. -1<ρ<0

If -1<ρ<0, then the function $x \mapsto x^{-\rho/\sigma}$ is increasing (for all x>0). In this case, inequality (17) is equivalent to

$$A^{-\frac{\rho}{\sigma}}\left(\sum_{i=1}^{n} \alpha_i x_i^{-\rho}\right) \geq y^{-\frac{\rho}{\sigma}} \;\Leftrightarrow\; -\sum_{i=1}^{n} A^{-\frac{\rho}{\sigma}} \alpha_i x_i^{-\rho} y^{\frac{\rho}{\sigma}} \leq -1, \tag{39}$$

so (15)-(17) becomes a signomial geometric programming problem (15)-(16) and (39). SGP problem (15)-(16) and (39) can be solved similarly to (15)-(16) and (18). The only difference is changing parameter ρ<0 by $-\rho$>0 into equations (19)-(24). From that, by doing some algebraic calculations, it follows that the solution in this case is

$$\pi^{CES} = \left(pA(1-\sigma)\right)^{1/(1-\sigma)} \left(\frac{\sigma}{1-\sigma}\right)^{\frac{\sigma}{1-\sigma}} \left(\sum_{i=1}^{n} v_i^{\frac{-\rho}{1-\rho}} \alpha_i^{\frac{1}{1-\rho}}\right)^{\frac{-(1-\rho)\sigma}{-\rho(1-\sigma)}}, \tag{40}$$

$$x_i^{CES} = \frac{\frac{\sigma}{1-\sigma}\left(\frac{\alpha_i}{v_i}\right)^{\frac{1}{-\rho+1}}}{\sum_{k=1}^{n} v_k^{\frac{-\rho}{-\rho+1}} \alpha_k^{\frac{1}{-\rho+1}}} \cdot \pi^{CES},\ i = 1, 2, \ldots, n\,. \tag{41}$$

Note that (40) and (41) have the same form as (33) and (38), respectively, where the only difference is the change of parameter ρ with $-\rho$.

The profit maximization problem with Cobb-Douglas technology

In this section, we show that the solution to the profit maximization problem with Cobb-Douglas technology given by (4)-(5) is the limiting case of (33) and (38) when ρ>0, i.e. the limiting case of (40)-(41) when -1<ρ<0. Let us first show how the Cobb-Douglas production function can be obtained from the CES production function. Let CDPF be given by (1) where (3) holds. Let us define

$$\sigma = \sum_{i=1}^{n} \varphi_i\ , \tag{42}$$

$$\alpha_i = \frac{\varphi_i}{\sigma},\ i = 1, 2, \ldots, n\,. \tag{43}$$

Note that (3) and (42) imply (25). Furthermore, note that

$$\sum_{i=1}^{n} \alpha_i \overset{(43)}{=} \sum_{i=1}^{n} \frac{\varphi_i}{\sigma} = \frac{1}{\sigma} \sum_{i=1}^{n} \varphi_i \overset{(42)}{=} 1\,. \tag{44}$$

Let

$$U = \lim_{\rho \to 0} A\left(\sum_{j=1}^{n} \alpha_j x_j^{-\rho}\right)^{-\frac{\sigma}{\rho}}. \tag{45}$$

Since (44) holds, by taking a natural logarithm and after applying L'Hospital's rule, from (45) we have

$$\begin{aligned} \ln U &= \ln A + \lim_{\rho \to 0} \frac{-\sigma \ln\left(\sum_{i=1}^{n} \alpha_i x_i^{-\rho}\right)}{\rho} \overset{L'H}{=} \ln A + \lim_{\rho \to 0} \frac{\sigma \sum_{i=1}^{n}\left(x_i^{-\rho} \ln x_i^{\alpha_i}\right)}{\sum_{i=1}^{n} \alpha_i x_i^{-\rho}} = \\ &= \ln A + \frac{\sigma \sum_{i=1}^{n} \ln x_i^{\alpha_i}}{\sum_{i=1}^{n} \alpha_i} = \ln A + \frac{\sum_{i=1}^{n} \ln x_i^{\sigma\alpha_i}}{1} = \ln\left(A \prod_{i=1}^{n} x_i^{\sigma\alpha_i}\right) \overset{(43)}{=} \ln\left(A \prod_{i=1}^{n} x_i^{\varphi_i}\right). \end{aligned} \tag{46}$$

Then, from (46) we have

$$U = \lim_{\rho \to 0} A\left(\sum_{i=1}^{n} \alpha_i x_i^{-\rho}\right)^{-\frac{\sigma}{\rho}} = A \prod_{i=1}^{n} x_i^{\varphi_i}. \tag{47}$$

Thus, the Cobb-Douglas production function given by (1) is the limit when $\rho \to 0$ of the CES production function given by (6).

Further, let us show how $\pi^{C\text{-}D}$ from (4) can be obtained from π^{CES}. From (33) we have

$$\begin{aligned} \lim_{\rho \to 0^+} \pi^{CES} &= \lim_{\rho \to 0}\left(pA(1-\sigma)\right)^{\frac{1}{1-\sigma}} \left(\frac{\sigma}{1-\sigma}\right)^{\frac{\sigma}{1-\sigma}} \left(\sum_{i=1}^{n} v_i^{\frac{\rho}{\rho+1}} \alpha^{\frac{1}{\rho+1}}\right)^{\frac{-(\rho+1)\sigma}{\rho(1-\sigma)}} \\ &= \left(pA(1-\sigma)\right)^{\frac{1}{1-\sigma}} \left(\frac{\sigma}{1-\sigma}\right)^{\frac{\sigma}{1-\sigma}} \cdot \Lambda, \end{aligned} \tag{48}$$

where

$$\Lambda = \lim_{\rho \to 0^+} \left(\sum_{i=1}^{n} v_i^{\frac{\rho}{\rho+1}} \alpha^{\frac{1}{\rho+1}}\right)^{\frac{-(1+\rho)\sigma}{\rho(1-\sigma)}}. \tag{49}$$

Since (44) holds, by taking a natural logarithm and after applying L'Hospital's rule, from (49) we have

$$\begin{aligned} \ln \Lambda &= \lim_{\rho \to 0^+} \frac{-(\rho+1)\sigma \ln\left(\sum_{i=1}^{n} v_i^{\frac{\rho}{\rho+1}} \alpha_i^{\frac{1}{\rho+1}}\right)}{\rho(1-\sigma)} = \\ &\overset{L'H}{=} \lim_{\rho \to 0^+} \frac{-\sigma \ln\left(\sum_{i=1}^{n} v_i^{\frac{\rho}{\rho+1}} \alpha_i^{\frac{1}{\rho+1}}\right) - (\rho+1)\sigma\left(\frac{1}{(\rho+1)^2} \sum_{i=1}^{n} v_i^{\frac{\rho}{\rho+1}} \alpha_i^{\frac{1}{\rho+1}} \ln \frac{v_i}{\alpha_i}\right) \Big/ \left(\sum_{i=1}^{n} v_i^{\frac{\rho}{\rho+1}} \alpha_i^{\frac{1}{\rho+1}}\right)}{1-\sigma} \\ &= -\frac{\sigma}{1-\sigma} \sum_{i=1}^{n} \alpha_i \ln \frac{v_i}{\alpha_i} = \ln \prod_{i=1}^{n} \left(\frac{v_i}{\alpha_i}\right)^{-\frac{\sigma\alpha_i}{1-\sigma}}. \end{aligned} \tag{50}$$

Thus, from (42)-(43) and (48)-(50) we have

$$\begin{aligned}\lim_{\rho\to 0^+}\pi^{CES} &= \left(pA(1-\sigma)\right)^{\frac{1}{1-\sigma}}\left(\frac{\sigma}{1-\sigma}\right)^{\frac{\sigma}{1-\sigma}}\prod_{i=1}^{n}\left(\frac{v_i}{\alpha_i}\right)^{-\frac{\sigma\alpha_i}{1-\sigma}} \\ &= (pA)^{1/\left(1-\sum_{i=1}^{n}\varphi_i\right)}(1-\sigma)\sigma^{\frac{\sigma}{1-\sigma}}\prod_{i=1}^{n}\left(\frac{v_i}{\varphi_i/\sigma}\right)^{\frac{-\varphi_i}{1-\sum_{i=1}^{n}\varphi_i}} \\ &= (pA)^{1/\left(1-\sum_{i=1}^{n}\varphi_i\right)}(1-\sigma)\sigma^{\frac{\sigma}{1-\sigma}}\sigma^{\frac{-\sigma}{1-\sigma}}\prod_{i=1}^{n}\left(\frac{v_i}{\varphi_i}\right)^{\frac{-\varphi_i}{1-\sum_{i=1}^{n}\varphi_i}} \\ &= (pA)^{1/\left(1-\sum_{i=1}^{n}\varphi_i\right)}\left(1-\sum_{i=1}^{n}\varphi_i\right)\prod_{i=1}^{n}\left(\frac{v_i}{\varphi_i}\right)^{\frac{-\varphi_i}{1-\sum_{i=1}^{n}\varphi_i}} \\ &= \pi^{C-D}.\end{aligned} \tag{51}$$

Thus, the profit $\pi^{C\text{-}D}$ from (4) is the limit when $\rho\to 0^+$ of the profit π^{CES} from (33). When $-1<\rho<0$, by using a similar procedure, we can show that the profit $\pi^{C\text{-}D}$ from (4) is the limit when $\rho\to 0^-$ of the profit π^{CES} from (40).

Finally, let us show how x_i^{C-D} from (5) can be obtained from x_i^{CES}, $i=1,2,...,n$. Let

$$V_i = \lim_{\rho\to 0^+} x_i^{CES},\ i=1,2,...,n. \tag{52}$$

Since (43)-(44) hold, from (38), (51) and (52) we have

$$\begin{aligned}V_i &= \lim_{\rho\to 0^+}\frac{\frac{\sigma}{1-\sigma}\left(\frac{\alpha_i}{v_i}\right)^{\frac{1}{\rho+1}}}{\sum_{k=1}^{n}v_k^{\frac{\rho}{\rho+1}}\alpha_k^{\frac{1}{\rho+1}}}\cdot\pi^{CES} = \lim_{\rho\to 0^+}\frac{\frac{\sigma}{1-\sigma}\left(\frac{\alpha_i}{v_i}\right)^{\frac{1}{\rho+1}}}{\sum_{k=1}^{n}v_k^{\frac{\rho}{\rho+1}}\alpha_k^{\frac{1}{\rho+1}}}\cdot\lim_{\rho\to 0^+}\pi^{CES} = \\ &= \frac{\frac{\sigma}{1-\sigma}\cdot\frac{\alpha_i}{v_i}}{\sum_{k=1}^{n}1\cdot\alpha_k^1}\cdot\pi^{C-D} = \frac{\sigma}{1-\sigma}\cdot\frac{\varphi_i/\sigma}{v_i}\cdot\pi^{C-D} = \frac{\pi^{C-D}\varphi_i}{v_i\left(1-\sum_{k=1}^{n}\varphi_k\right)} \\ &= x_i^{C-D}.\end{aligned} \tag{53}$$

Thus, x_i^{C-D} from (5) is the limit when $\rho\to 0^+$ of x_i^{CES}, $i=1,2,...,n$, from (38). When $-1<\rho<0$, by using a similar procedure, we can show that x_i^{C-D} from (5) is the limit when $\rho\to 0^-$ of x_i^{CES}, $i=1,2,...,n$ from (41).

Conclusion

One of the most important problems in economics is the firm's profit maximization problem. In this paper, we solved the profit maximization problem with CES technology with $n\geq 2$ inputs using a geometric programming approach and power mean inequality. Unlike multivariable calculus, this procedure does not require checking nontrivial necessary and sufficient conditions. Instead, a unique solution followed by power mean inequality and the definition of a strict global maximum directly. Finally, by using L'Hospital rule only, we showed how the solution to the profit maximization problem with Cobb-Douglas technology could be derived from the CES technology case.

Recommendations

Given that the geometric programming approach to the profit maximization problem bypasses checking nontrivial necessary and sufficient conditions when multivariable calculus is used, educators could incorporate this technique into classrooms to present this important topic in a complementary way. Since geometric programming and the power mean inequality are simple optimization techniques without derivatives, they can provide new insights into the given problem to managers, students, and other audiences who may be unfamiliar with multivariable calculus.

Scientific Ethics Declaration

The author declares that the scientific ethical and legal responsibility of this article published in EPSTEM journal belongs to the author.

Acknowledgements or Notes

This article was presented as an oral presentation at the International Conference on Basic Sciences, Engineering and Technology (www.icbaset.net) conference held in Istanbul/Turkey on August 25-28, 2022.

No funding was received for conducting this study.

References

Avvakumov, S. N., Kiselev, Yu. N., Orlov, M. V., & Taras'ev, A. M. (2010). Profit maximization problem for cobb-douglas and CES production function. *Computational Mathematics and Modeling*, *21*, 336-378.

Angeli, E., Wagner, J., Lawrick, E., Moore, K., Anderson, M., Soderland, L., & Brizee, A. (2010, May 5). General format. http://owl.english.purdue.edu/owl/resource/560/01/ https://doi.org/10.1007/s10598-010-9075-5

Boyd, S., Kim, S.-J., Vanderberghe, L., & Hassibi, A. (2007). A tutorial on geometric programming. *Optimization and Engineering*, *8*, 67-127. https://doi.org/10.1007/s11081-007-9001-7

Beightler, C. S., & Philips, D. T. (1976). Applied geometric programming. New York: John Wiley & Sons.

Bullen, P. S. (2003). *Handbook of means and their inequalities*. Springer Dordrecht. https://doi.org/10.1007/978-94-017-0399-4

Duffin, R. J., Peterson, E. L., & Zener, C. (1967). *Geometric programming – theory and applications*. New York: John Wiley & Sons.

Jehle, G. A., & Reny, P. J. (2011). *Advanced microeconomic theory*. New Jersey: FT Prentice.

Kojić, V. & Lukač, Z. (2018). Solving profit maximization problem in case of the Cobb-Douglas production function via weighted AG inequality and geometric programming. Proceedings from: *2018 IEEE International Conference on Industrial Engineering and Engineering Management (IEEM)*, Bangkok, Thailand, 1900-1903. https://doi.org/10.1109/IEEM.2018.8607446

Liu, S. T. (2006). A geometric programming approach to profit maximization. *Applied Mathematics and Computation*, *182*, 1093-1097. https://doi.org/10.1016/j.amc.2006.04.061

Reklaitis G., Salas, V., & Whinston, A. (1975). *Duality and geometric programming*. https://pure.iiasa.ac.at/id/eprint/283/1/WP-75-145.pdf

Zevelev, A. A. (2014, November). *Closed form solutions in economics*. https://ssrn.com/abstract=2354226

Author Information

Vedran Kojić
Faculty of Economics and Business, University of Zagreb
Trg J. F. Kennedyja 6, 10000 Zagreb, Croatia
Contact e-mail: *vkojic@efzg.hr*

To cite this article:

Kojić, V. (2022). On a geometric programming approach to profit maximization: the case of CES technology. *The Eurasia Proceedings of Science, Technology, Engineering & Mathematics (EPSTEM), 18,* 7-15.

The Eurasia Proceedings of Science, Technology, Engineering & Mathematics (EPSTEM)
ISSN: 2602-3199

The Eurasia Proceedings of Science, Technology, Engineering & Mathematics (EPSTEM), 2022

Volume 18, Pages 16-21

ICBASET 2022: International Conference on Basic Sciences, Engineering and Technology

De Novo Gold Nanoparticles Activate P53 by Inhibiting NF-Kb Signalling in Breast Cancer Cells

Muhammad SAFDAR
Gaziantep University

Mehmet OZASLAN
Gaziantep University

Abstract: The aim of this study was to make de novo gold nanoparticles (Au(0)NPs) that turn on p53 and turn off NF-kB signaling in SKBR3 breast cancer cells. The chemical method was used to make the erythromycin-based Au(0)NPs. Authentic techniques were used to figure out what these Au(0)NPs were like. In the end, relative gene expression studies were used to treat SKBR3 breast cancer cells with these Au(0)NPs as a nanomedicine. When Au(0)NPs were present, the levels of caspases 3, 8, and 9 changed, p53 was turned on, and NF-kB was turned off at the same time. Compared to normal breast cells, the number of breast cancer cells (SKBR3) that could live was cut down (CRL-4010). Gene expressions of caspases also showed that the data were correct. When AuNPs were used to treat breast cancer cells, it was found that p53 and NF-kB had the opposite relationship. The study laid out a first step for using newly made AuNPs as a chemotherapeutic agent to treat SKBR3 cells.

Keywords: Gold nanoparticles, Erythromycin, Gene expression, Cell Viability, Breast Cancer

Introduction

Patients with breast cancer are also more likely to become resistant to chemotherapy, and relapses of the disease are widely accepted (Sung et al., 2021). Following the development of multidrug resistance that is complicated due to many factors that cause, is a major problem for breast cancer treatment (Nedeljkovic & Damjanovic, 2019).

Researchers are interested in chemotherapies that use nanoparticles. When gold nanoparticles (AuNPs) are used to treat cancer, the results have been very positive (Mousavi et al., 2007; Shreyash et al., 2021). Not only do these particles stop the growth of cancers (Safdar et al., 2022; Safdar et al., 2019) other than normal cells, but they induce apoptosis that is the main goal of cancer drugs (López-Barrera et al., 2021), and you can easily see how they work by looking at caspases. Also, the action of gold nanoparticles on the tumour suppressor p53 (López-Barrera et al., 2021) that is involved in the apoptosis pathways (Kanamori et al., 2021). It is also known that NF-kB work inversely to p53, and breast cancer cells have too much of it (Ge et al., 2021). So, stopping NF-kB could be used as a chemotherapeutic target. Also, in some studies it is found that the p53 and NF-kB followed different pathways due to change of drugs in the tumor cells (Gottstein et al., 2013). Furthermore, it had been seen that if gene expression changes had been done in the p53 gene then it led to change NF-kB and finally induce different cancers (Fadaka et al., 2021). Even though there are some drugs that selectively turn on p53 or turn off NF-kB with multiple side effects. Therefore, it is a need of time for specific nano-drugs that can control different pathways to inhibit breast cancers. So, a major goal for making new cancer drugs is to turn on p53 and shut down the NF-kB pathway (Arshad et al., 2019; Safdar & Ozaslan, 2022; Safdar et al., 2021).
The purpose of this study was to synthesize de novo gold nanoparticles activate p53 by inhibiting NF-kB signalling in breast cancer cell lines by using MTT and qRT-PCR assays.

- Selection and peer-review under responsibility of the Organizing Committee of the Conference

Method

Preparation of gold nanoparticles

For the first time, it was shown that the er-AuNPs were made with the help of erythromycin (er) as a reducing agent and a capping agent. For the making of er-AuNPs, 0.5 mL of a 0.01 M solution of HAuCl4 salts was put in a glass beaker and put on a hotplate at 100 °C for 20 minutes. Then, 0.1 mL of a 0.01 M solution of NaOH was added, and the mixture was left for 1 hour to develop its properties. The solution proceeded from yellow to purple, which shows that the AuNPs were there. Also, UV Vis, XRD, and FT-IR were used to find out more about these newly made AuNPs. Lastly, SKBR3 cell lines were used to test the cytotoxicity of these nanoparticles. The average size of AuNPs was between 10 and 50 nm. These particles were made in culture media with 0–200 g/mL of serum or no supplements.

Cell Culture

Human breast epithelium CRL-4010 and breast cancer cell line SKBR3 were grown in Dulbecco's modified Eagle's medium with 10% foetal calf serum and antibiotic-antimycotic solution (100 U/mL penicillin, 0.1 mg/ml streptomycin, and 0.25 g/mL amphotericin B). Cells were grown in a sterile, humidified, 37°C environment with 5% CO2 until they reached full growth.

Cell Viability

Researchers used the MTT assay to measure how alive the cells were. In a 96-well plate with 3000 cells per well, er-AuNP was put in front of cells for 24 hours. Used media was thrown away and replaced with 10 mg/mL of MTT reagent and 100 L of new media (1:9). Another hour of incubation at 37 °C was given to the chromogen reaction to take place. The cells were washed with PBS, and 100 L/well of dimethyl sulfoxide was added to dissolve the formazan crystals. A microplate spectrophotometer was used to measure the absorbance at a wavelength of 505 nm (Molecular Devices). At least three separate experiments with at least duplicate samples were done.

qRT-PCR

Cells were grown in a 25 cm^2 flask, and the NucleoZOL method was used to get the total RNA from the cells (Macherey-Nagel, Germany). In a PCR thermal cycler, a "Precision Reverse Transcription Kit" (made by Qiagen in Germany) was used to do the reverse transcription (Applied BioSystems, USA). By comparing the transcript levels of NF-kB, p53, and caspases to the level of the housekeeping gene GAPDH, real-time PCR was used to find out how these levels changed. The reactions went through 40 cycles with 94 °C for 30 sec, 55-60°C for 45 sec, and 72 °C for 45 sec along with a final extension step of 72 °C for 4 min. Changes in gene expression between groups were found using the method called $2^{-\Delta\Delta CT}$.

Results

After 24 hours, the amount of AuNP were used to treat CRL-4010 and SKBR3 cells induced and evaluate the cell viability. But the response to treatment was stronger in SKBR2 cancer cells than in normal cells. Starting at a concentration of 50 g/ml, when AuNP was added to SKBR3 cells, the IC50 of the cells went down. Cancer cells treated with AuNP showed clear signs of cell death, while normal breast cells lost much less cell viability (Fig. 1). So, we knew that AuNPs were selective for cancer cells because at a higher dose of 150 µg/ml, only 50% of the normal CRL-4010 cells were still alive.

In this study, we investigated how er-AuNP affected the various genes including p53, NF-kB and caspases in CRL-4010 and SKBR3 cell lines. These results showed that Casp3, Casp8, and Casp9 were higher in er-AuNP treated CRL-4010 cells compared to untreated control cells, but p53 and NF-kB gene expression was almost the same in both groups of cells. On the other hand, the mRNA transcripts for p53, Casp3, Casp8, and Casp9 went up a lot in the SKBR3 cells. But when AuNP was added to SKBR3 cells, NF-kB expression went down (Fig. 2). All of the genes selected were affected by the change in mRNA levels in SKBR3 cells.

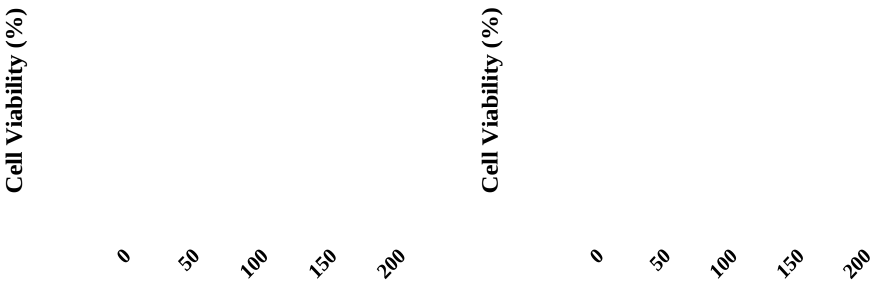

Figure. 1. Compared to CRL-4010 cell line, SKBR3 cell line was decreased when AuNPs were added. MTT showed that SKBR3 were more decreased than CRL-4010 and after being exposed to 0-200g/mL AuNP concentrations. All the data is represented in the form of *P 0.01; **P 0.001; ***P 0.0001.

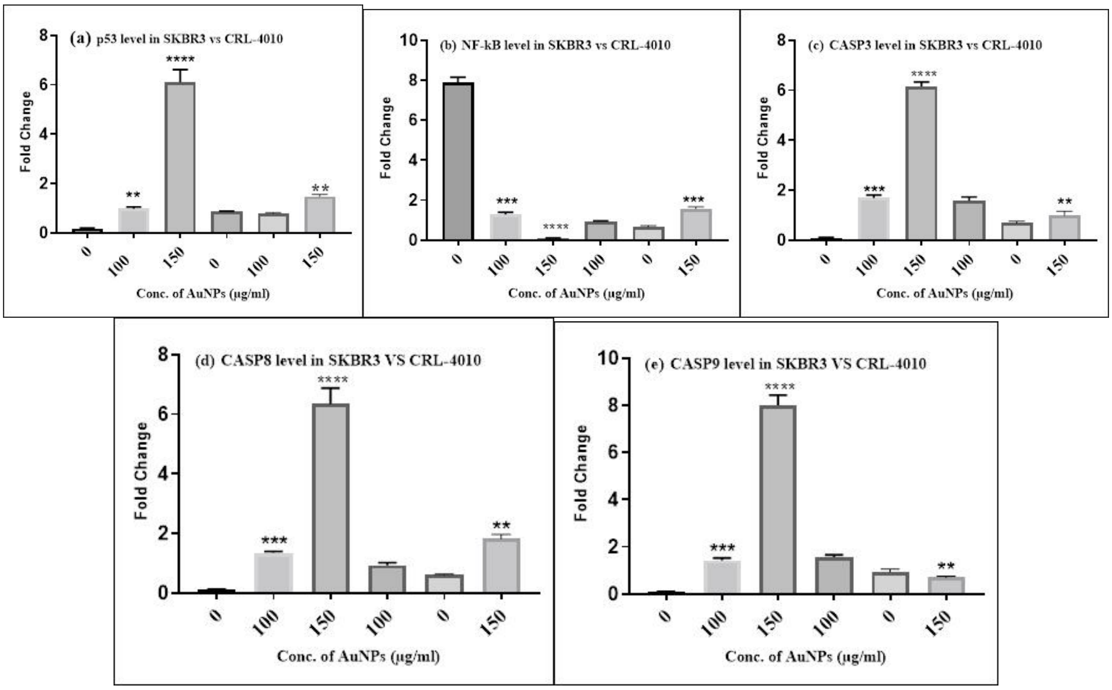

Figure. 2. When AuNP was added to SKBR3 for 24 hours, the p53 gene gene expression increased and the NF-kB gene expression dropped down. The amounts of targeted genes (p53, caspases 3, 8, and 9, and NF-kB) mRNA transcript continued to persist in CRL-4010 (control) cells. The levels of p53, caspases 3, 8, and 9, as well as the levels of NF-kB mRNA gene transcripts, were significantly changed in SKBR3 breast cancer cells. *P≤0.05, **P≤0.01 (Figure. 2a-e).

Discussion

Due to their unique ability to sense tumours, AuNPs have become very promising materials for treating malignant tumours. Because of this, AuNPs have been thought of for a long time as a possible tool for diagnosing and treating different types of cancer. In this study, we talked about the likely way that newly made er-AuNPs induce apoptosis in SKBR3 cells and how exposure to er-AuNPs changes in the targeted genes particularly p53 and NF-kB (Fig. 1&2). Previously, different nanoparticles were used by some researchers to show that these mechanisms were at work in human hepatocellular carcinoma cells (Ahmadian et al., 2018). It is also known that AuNPs have less toxicity as compared to other nanoparticles so they can be used as chemotherapeutics (Khan et al., 2021). Also, this study made it clear that 50-99 ug/ml concentrations of these nanoparticles were best on SKBR3 cells at the same concentration (cancer cells). Other concentrations, like 150 and 200 ug/ml, were very harmful to both healthy and cancerous cells. That was the real reason we did not used them in gene expression studies on both normal and cancer cells. Researchers may need to look into this more.

Nanomaterials also have a special property called cell-dependent cytotoxicity, which has been seen in HT29 and HeLa (Shejawal et al., 2021), MCF-7 (Uzma et al., 2020), and A459 (Niloy et al., 2021) cancer cells.

It is a known fact that the apoptosis is followed by both pathways (intrinsic and extrinsic) (Rajendran et al., 2021) that led to the planned death of the cells. The cytochrome C is a key protein that attach to Apaf-1 (Bock & Tait, 2020) that is released when a cell dies through the intrinsic pathway. Apaf1 turns on caspase 9, which turns on caspase 3, which is a very important part of cell death (Bock & Tait, 2020). Death receptors, on the other hand, turn on caspase 8, which then turns on caspase 3 (Muscari et al., 2020). The intrinsic pathway is now turned on by caspase 3 (Muscari et al., 2020; Safdar et al., 2020; Vo-Dinh et al., 2005). In this study, mRNA expression (caspase 9, 8, and 3) of the targeted genes were very low in normal CRL-4010 cells but it was more than four folds in cancerous SKBR3 cells. This shows that AuNPs work more specifically on cancer cells (Fig. 2). This meant that AuNPs sped up both the internal and external apoptotic cascades in breast cancer cells, which led to the death of the cells. Even when cancer cells were only exposed to 50 M of AuNPs, the expression of caspase 3 went up by a large amount (Safdar et al., 2021). So far as we know, this is the first report that shows how er-AuNPs affect both apoptotic cascades in breast cancer cells. Still, more research is needed to figure out how AuNPs cause cell death at the molecular level. One problem with this study was that it only used in-vitro experiments. More research will be needed to see how AuNPs work in in-vivo models before they can be used as a treatment for breast cancer.

Conclusion

So, these results showed that the newly synthesised and characterised er-AuNPs are a new and promising nanomaterial for a robust evidence-based analysis of chemotherapeutics. Using er-AuNPs could be a smart way to figure out where breast cancer could be spreading. Using relative gene expression studies, changes in caspases 3, 8, and 9 as well as dependence on p53 and NF-kB were found to be higher in SKBR3 than in normal breast cells (CRL-4010).

Recommendations

The study laid out the first step toward using er-AuNPs as a chemotherapeutic and suggested that more research to be done. Also, we recommend the nano-ELISA for further protein analysis.

Scientific Ethics Declaration

The authors declare that the scientific ethical and legal responsibility of this article published in EPSTEM journal belongs to the authors.

Acknowledgements or Notes

* This article was presented as an oral presentation at the International Conference on Basic Sciences, Engineering and Technology (www.icbaset.net) conference held in Istanbul/Turkey on August 25-28, 2022.

References

Ahmadian, E., Dizaj, S. M., Rahimpour, E., Hasanzadeh, A., Eftekhari, A., Halajzadeh, J., & Ahmadian, H. (2018). Effect of silver nanoparticles in the induction of apoptosis on human hepatocellular carcinoma (HepG2) cell line. *Materials Science and Engineering: C, 93*, 465-471.

Arshad, M., Ozaslan, M., Ali, H., Safdar, M., Junejo, Y., & Babar, M. (2019). Molecular investigation of gold nanoparticles toxicity in mice model and p53 activation. *J Biol Sci*, *19*, 391-395.

Bock, F. J., & Tait, S. W. (2020). Mitochondria as multifaceted regulators of cell death. *Nature Reviews Molecular Cell Biology*, *21*(2), 85-100.

Fadaka, A., Aluko, O., Awawu, S. & Theledi, K. (2021). Green synthesis of gold nanoparticles using Pimenta dioica leaves aqueous extract and their application as photocatalyst, antioxidant, and antibacterial agents. *Journal of Multidisciplinary Applied Natural Science*, *1*(2).

Ge, W., Wang, Y., Zheng, S., Zhao, D., Wang, X., Zhang, X., & Hu, Y. (2021). Nuclear iASPP determines cell fate by selectively inhibiting either p53 or NF-κB. *Cell Death Discovery*, *7*(1), 1-10.

Gottstein, C., Wu, G., Wong, B. J., & Zasadzinski, J. A. (2013). Precise quantification of nanoparticle internalization. *ACS Nano*, *7*(6), 4933-4945.

Kanamori, Y., Finotti, A., Magno, L. D., Canettieri, G., Tahara, T., Timeus, F., . . . Fino, P. (2021). Enzymatic spermine metabolites induce apoptosis associated with increase of p53, caspase-3 and miR-34a in both neuroblastoma cells, SJNKP and the N-Myc-amplified form IMR5. *Cells*, *10*(8), 1950.

Khan, M. A., Singh, D., Ahmad, A., & Siddique, H. R. (2021). Revisiting inorganic nanoparticles as promising therapeutic agents: a paradigm shift in oncological theranostics. *European Journal of Pharmaceutical Sciences*, *164*, 105892.

López-Barrera, L. D., Díaz-Torres, R., Martínez-Rosas, J. R., Salazar, A. M., Rosales, C., & Ramírez-Noguera, P. (2021). Modification of proliferation and apoptosis in breast cancer cells by exposure of antioxidant nanoparticles due to modulation of the cellular redox state induced by doxorubicin exposure. *Pharmaceutics*, *13*(8), 1251.

Mousavi, S. M., Montazeri, A., Mohagheghi, M. A., Jarrahi, A. M., Harirchi, I., Najafi, M., & Ebrahimi, M. J. T. b. j. (2007). Breast cancer in Iran: an epidemiological review. *The Breast Journal, 13*(4), 383-391.

Muscari, I., Adorisio, S., Liberati, A. M., Thuy, T. T., Van Sung, T., Cannarile, L., . . . Delfino, D. V. (2020). Bcl-xL overexpression decreases GILZ levels and inhibits glucocorticoid-induced activation of caspase-8 and caspase-3 in mouse thymocytes. *Journal of Translational Autoimmunity*, *3*, 100035.

Nedeljkovic, M., & Damjanovic, A. (2019). Mechanisms of chemotherapy resistance in triple-negative breast cancer-how we can rise to the challenge. *Cells*, *8*(9). https://doi.org/10.3390/cells8090957

Niloy, M. S., Shakil, M., Hossen, M., Alam, M., & Rosengren, R. J. (2021). Promise of gold nanomaterials as a lung cancer theranostic agent: a systematic review. *International Nano Letters*, *11*(2), 93-111.

Rajendran, I., Ponrasu, T., Rajaram, R., & Suguna, L. (2021). The apoptotic effect of ferulic acid-synthesized gold nanoparticles against human epidermoid carcinoma (A431) cells via activation of caspase-3 pathway. *Journal of Drug Delivery Science and Technology*, *63*, 102478.

Safdar, M., & Ozaslan, M. (2022). Enhanced catalytic, antibacterial and anti-cancer activities of erythromycin capped gold nanoparticles. *Journal of Inorganic and Organometallic Polymers and Materials*, 1-9.

Safdar, M., Ozaslan, M., Junejo, Y., & Channa, I. S. (2022). Cytotoxic and anticancer activity of a novel synthesized tet-AuNPs simultaneously activates p53 and inhibits NF-kB signaling in SKBR3 cell line. *Toxicology and Environmental Health Sciences*, *14*(1), 69-76.

Safdar, M., Ozaslan, M., Junejo, Y., & Channa, I. S. (2022). Cytotoxic and anticancer activity of a novel synthesized tet-AuNPs simultaneously activates p53 and inhibits NF-kB signaling in SKBR3 cell line. *Toxicology and Environmental Health Sciences, 14*(1), 69-76.

,Safdar, M., Ozaslan, M., Khailany, R. A., Latif, S., Junejo, Y., Saeed, M., . . . Kanabe, B. O. (2019). Synthesis, characterization and applications of a novel platinum-based nanoparticles: catalytic, antibacterial and cytotoxic Studies. *Journal of Inorganic and Organometallic Polymers and Materials*. https://doi.org/10.1007/s10904-019-01387-7

Safdar, M., Ozaslan, M., Khailany, R. A., Latif, S., Junejo, Y., Saeed, M., . . . Materials. (2020). Synthesis, characterization and applications of a novel platinum-based nanoparticles: catalytic, antibacterial and cytotoxic studies. *30*(7), 2430-2439.

Shejawal, K. P., Randive, D. S., Bhinge, S. D., Bhutkar, M. A., Todkar, S. S., Mulla, A. S., & Jadhav, N. R. (2021). Green synthesis of silver, iron and gold nanoparticles of lycopene extracted from tomato: their characterization and cytotoxicity against COLO320DM, HT29 and Hella cell. *Journal of Materials Science: Materials in Medicine*, *32*(2), 1-12.

Shreyash, N., Sonker, M., Bajpai, S., & Tiwary, S. K. (2021). Review of the mechanism of nanocarriers and technological developments in the field of nanoparticles for applications in cancer theragnostics. *ACS Appl Bio Mater*, *4*(3), 2307-2334. https://doi.org/10.1021/acsabm.1c00020

Sung, H., Ferlay, J., Siegel, R. L., Laversanne, M., Soerjomataram, I., Jemal, A., & Bray, F. (2021). Global cancer statistics 2020: globocan estimates of incidence and mortality worldwide for 36 cancers in 185 countries. *CA Cancer J Clin*, *71*(3), 209-249. https://doi.org/10.3322/caac.21660

Uzma, M., Sunayana, N., Raghavendra, V. B., Madhu, C. S., Shanmuganathan, R., & Brindhadevi, K. (2020). Biogenic synthesis of gold nanoparticles using commiphora wightii and their cytotoxic effects on breast cancer cell line (MCF-7). *Process Biochemistry*, *92*, 269-276.

Vo-Dinh, T., Yan, F., & Wabuyele, M. B. (2005). Surface-enhanced Raman scattering for medical diagnostics and biological imaging. *Journal of Raman Spectroscopy: An International Journal for Original Work in all Aspects of Raman Spectroscopy, Including Higher Order Processes, and also Brillouin and Rayleigh Scattering, 36*(6-7), 640-647..

Author Information

Muhammad Safdar
Department of Biology, Gaziantep University
Gaziantep 27310, Turkey

Mehmet Ozaslan
Department of Biology, Gaziantep University
Gaziantep 27310, Turkey
Contact e-mail: *ozaslanmd@yahoo.com*

To cite this article:

Safdar, M. & Ozaslan, M. (2022). De novo gold nanoparticles activate P53 by inhibiting NF-Kb signalling in breast cancer cells. *The Eurasia Proceedings of Science, Technology, Engineering & Mathematics (EPSTEM), 18*, 16-21.

The Eurasia Proceedings of Science, Technology, Engineering & Mathematics (EPSTEM)
ISSN: 2602-3199

The Eurasia Proceedings of Science, Technology, Engineering & Mathematics (EPSTEM), 2022

Volume 18, Pages 22-27

ICBASET 2022: International Conference on Basic Sciences, Engineering and Technology

Mineralogical and Elemental Characterization of Conventional Asphalt of Peruvian Roadways by X-Ray Diffraction and Energy Dispersive X-ray Fluorescence

Jenny Aleida MONTOYA-BURGA
Universidad César Vallejo

Jorge Aurelio BRAVO-CABREJOS
Universidad Nacional Mayor de San Marcos (UNMSM)

Marlon Gastón FARFÁN-CÓRDOVA
Universidad César Vallejo

María Luisa CERÓN-LOAYZA
Universidad Nacional Mayor de San Marcos (UNMSM)

Felipe Américo REYES-NAVARRO
Universidad Nacional Mayor de San Marcos (UNMSM)

Abstract: This research deals with the characterization of a sample of conventional asphalt, which is used for the manufacture of roadways in the city of Trujillo, Peru. The sample has been designed by using the Marshall method, through which the optimal content of the asphalt mixture was determined for an adequate combination of the aggregates. This method includes the determination of the optimum content of asphalt cement, stability, unit weight, air voids, flow, voids in the mineral aggregate, and flow stability. The Marshall test was carried out after dosing for the traditional mixture. We have used two techniques: energy dispersive X-ray fluorescence and X-ray diffractometry. The identification and quantification of the chemical elements present was carried out by using energy dispersive X-ray fluorescence, and the mineralogical analysis, by using X-ray diffractometry. This work is useful as a source of reference information. Subsequently, it will allow the implementation of procedures for modifying asphalt mixtures to optimize their performance.

Keywords: Asphalt, Marshall method, X-ray diffraction, Energy dispersive, X-ray fluorescence

Introduction

All over the world, there is no human activity that does not require the use of communication routes, whether road, rail, sea, lake, river, or air. The importance and improvement of these routes keep close parallelism with the cultural, commercial, and industrial development of each country; they are the means by which religion, culture and commerce are introduced into the regions of primitive civilization of a country (Vignolo, 1943). There are two concepts closely related to roadways: bitumen and asphalt. Bitumen or bitumen asphalt is a black to dark brown, semi-solid organic material that gradually liquefies when heated. It is usually obtained as a residue from petroleum distillation by using atmospheric or vacuum distillation units. Asphalt is a natural or commercial mixture of bitumen and inert mineral matter. Natural asphalt occurs as surface deposits, or as a colloidal crude oil system near the surface. In America, the term *asphalt* is often synonymous with the material known in England as asphaltic bitumen or bitumen (Whitehead, 2005).

- Selection and peer-review under responsibility of the Organizing Committee of the Conference

Trujillo is the third most important city in Peru; however, due to various factors, it has a road infrastructure in poor conditions. This could improve with a detailed knowledge of the constituents of roads, which would allow defining asphalt modification mechanisms, and consequently, provide better performance to the roads.

The durability of asphalt pavements is directly influenced by the climate of the place where they are located. In addition, other parameters must be considered, such as the magnitude and frequency of the traffic loads, the properties of the materials that compose it, the characteristics of the subgrade, humidity, and the construction process, among others. Together, these parameters greatly affect pavement performance as well as increase its potential to develop permanent deformation failure (Warrior and Chang, 2015).

Due to the importance of pavements in population dynamics, all its components must comply with technical specifications that guarantee their good performance: from their preparation to the different tests to which they are subjected, depending on the function for which they are intended. In Peru, these tests are regulated by the Ministry of Transport and Communications. Thereupon, it is necessary to delve into the different aspects that are associated with the lifespan of pavements. In this work, we carried out elemental and mineralogical analyses of a conventional asphalt sample obtained by the Marshall method. We expect that the information obtained can serve as a reference for the elaboration of modified asphalts.

Materials and Methods

Before the analysis of the sample, we proceeded as indicated below.

Preparation of the Asphalt Mixture

The aggregates to be used in the asphalt mixture manufacturing are dried at a constant weight, that is, the sample is heated at 105 ± 0.5 ^{o}C for a certain time, after which it is weighed and then the procedure is repeated until no variation in mass is seen. After drying, the aggregates will be separated by dry sieving into suitable fractions. A detailed procedure for obtaining the asphalt mixture can be found in the Peruvian technical standard MTC E 504.

Method and Physical Techniques Applied

We have used the Marshall method to design the asphalt mixture. Also, the modified asphalt sample has been characterized by using the two techniques indicated below.

Marshall Method

We applied the Marshall test to the conventional mixture because it is the standard method of asphalt mixture design. The asphalt design content in the final paving mixture is determined by the following parameters: stability, unit weight, air void, flow, VMA, and stability/flow; VMA means Voids in Mineral Aggregate. The method is as follows: First, the asphalt content is determined for which the void content is 4%, and then the other parameters calculated and measured for this asphalt content are evaluated and compared with the design criteria. If all the criteria are met, the asphalt design content is optimal. Otherwise, we should make some readjustments or redesign the mix.

Energy Dispersive X-ray Fluorescence (*EDXRF*)

This technique allows detecting the presence of chemical elements with atomic number Z equal to and greater than 13 by detecting the characteristic X-rays emitted by atoms. The energy of these rays increases with Z, and they can be detected as long as they have enough energy to penetrate the window in the detector. Due to this limitation, the Na (Z=11) and Mg (Z=12) peaks cannot be recorded in the EDXRF spectrum. The source used emits X-rays in two components: one spectrum with a continuous distribution from 0 to 30 keV, and the other containing the L and M characteristic X-rays from silver atoms, which are produced by the bombardment of the silver anode by energetic electrons. Consequently, the EDXRF spectrum have three main components: a continuous component provoked by the scattering of the x-rays from the continuous component of the source, a discrete spectrum produced by the scattering of the silver characteristic X-rays from the source, and a discrete spectrum of the characteristic X-rays emitted by the sample according to the elements it contains.

In the Archaeometry Laboratory of the Faculty of Physical Sciences (UNMSM), we determined the chemical composition of the sample by using a portable EDXRF equipment, Amptek brand, with a silver anode that operated at 30 kV and 15 μA. Irradiation was carried out with the following setting: (a) incidence and exit angles of around 45º, (b) distance from sample to X-ray source: 4 cm, and (c) distance from sample to detector: 2 cm approx. The operating voltage and the applied current were regulated so that the counting rate did not exceed 5000 cts/s.

X-ray Diffraction (*XRD*)

This technique allows for the identification of the mineralogical phases in the sample. It is also known as X-ray crystallography and is based on the diffraction of X-rays by matter, especially when it is crystalline. This diffraction is an elastic scattering, which originates interferences. This technique uses a beam of X-rays which, upon encountering a crystal, are reflected in specific directions determined by the wavelength of the X-rays, lattice parameters, and orientation of the crystal.

Thus, we conveyed the sample to the Bizalab private laboratory, where the measurements on the sample carried out by using an Endeavor D4 diffractometer, Bruker model, with a copper tube that operated at 40kV and 40 mA. Likewise, a 2θ angular scan from 5^o to 70^o and a step of 0.02^o/s was used. After obtaining the data, we identified the mineral phases by using the JCPDS-ICDD database. JCPDS means Joint Committee of Powder Diffraction Standards, and ICDD, International Center for Diffraction Data.

Discussion and Results

Table 1 shows the corresponding results of applying the Marshall method. Therein it is specified the parameters of Optimum Asphalt Content, stability, Unit Weight, Air Voids, Flow, VMA, Stability/Flow. The data are suitable so that the asphalt design content is optimal.

Table 1: Data from the Marshall test for the conventional asphalt mixture

Characterıstıcs of the Asphalt Mıxture	
Optimum Asphalt Content (%)	5.30
Stability (kg.)	1215
Unit Weight (kg/m^3)	2.342
Air Voids (%)	4.00
Flow (mm)	3.35
VMA (%)	14.78
Stability/Flow (kg/cm)	3626.87

In the EDXRF spectra, we observe that the peaks are positioned at certain energy values which indicate the presence of the chemical element in the sample. Symbols for the corresponding chemical elements are identified on top of the peaks. The height of the peaks is an indicator of the concentration of the chemical element in the sample. The EDXRF spectrum of the sample is presented in Figure 1. Table 2 details the corresponding quantitative elemental analysis. Figure 2 shows graphically the results of elemental concentration for the sample studied.

Figure 3 shows the X-ray diffractogram of the sample, which. concerning its mineralogical composition, registers the presence of quartz (SiO_2), clinochlore $(Mg,Fe^{2+})_5Al_2Si_3O_{10}(OH)_8$, albite $Na_{0,986}(Al_{1,005}Si_{2,995}O_8)$, and muscovite $KAl_3Si_3O_{10}(OH)_2$. The presence of Muscovite is not desirable, since, from the point of view of road construction, the presence of clay minerals results in greater use of bitumen. In addition, the lifespan of the pavement is reduced due to the low mechanical resistance of clay minerals (Geber and Gömze, 2015). An additional and important consequence of the small particle size is the high surface area to volume ratio (Parker & Rae, 1998). An indicator of the relative importance of surface effects is the specific surface area of a grain, which increases as the particle size decreases (Kaliakin et al., 2014). Thus, the presence of albite is not convenient either, since feldspars increase the specific surface area and decrease the mechanical resistance of the pavement (Geber & Gömze, 2015).

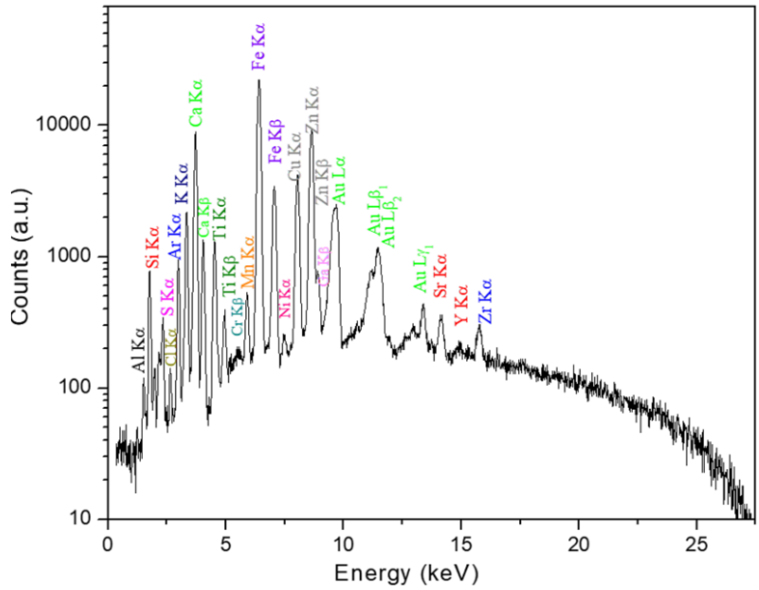

Figure 1. Energy dispersive X-ray fluorescence spectrum of the sample studied.

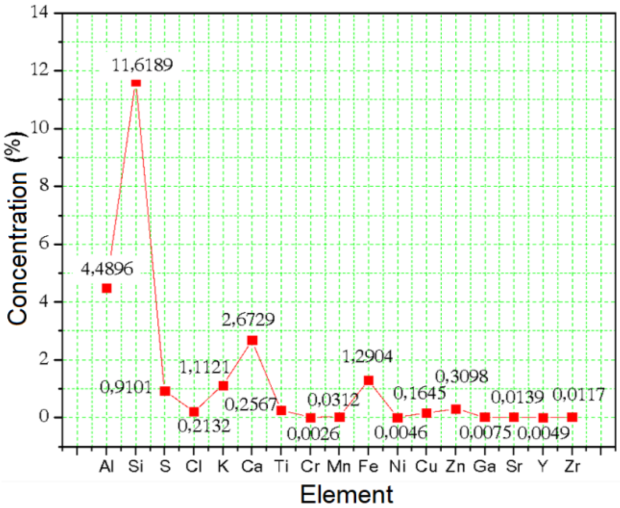

Figure 2. Graphic representation of quantitative analysis of the sample studied.

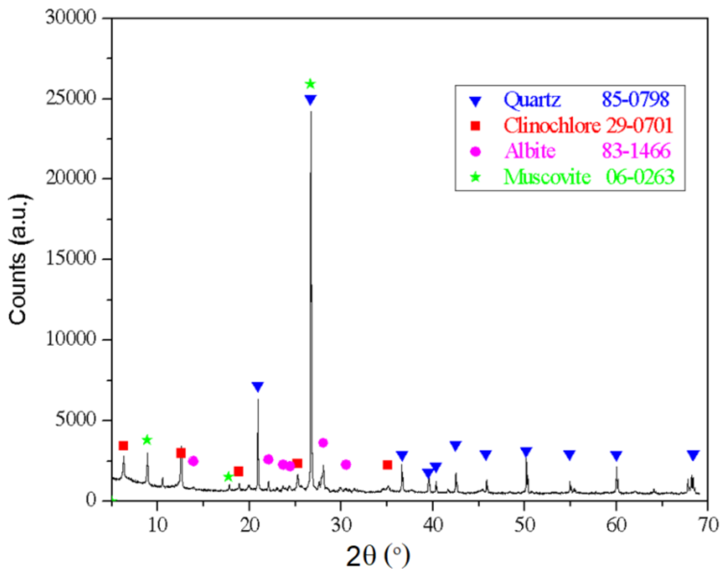

Figure 3. X-ray diffractogram of the sample. We noted the mineral composition and the codes from the JCPDS.

Conclusions

The sample studied presents aluminium, silicon, and calcium as major elements; to a lesser extent, sulphur, potassium, and iron are observed. Chlorine, titanium, chromium, manganese, nickel, copper, zinc, gallium, strontium, yttrium, and zirconium are minor elements. The mineralogical composition of the sample is formed by quartz, clinochlore, albite, and muscovite. We expect that the information obtained is useful so that modification procedures for asphalt mixtures are subsequently implemented to optimize their performance.

Recommendations

This work can be extended with the manufacturing of additional samples by the Marshal method, which have other percentages of optimum asphalt content and VMA.

Scientific Ethics Declaration

The authors declare that the scientific ethical and legal responsibility of this article published in EPSTEM journal belongs to the authors.

Acknowledgements

This article was presented as a poster presentation at the International Conference on Basic Sciences, Engineering and Technology (www.icbaset.net) conference held in Istanbul/Turkey on August 25-28, 2022.

References

Cáceres, C. (2007). *Análisis de la metodología Superpave para el diseño de mezclas asfálticas en México* (Analysis of the Superpave methodology for the design of asphalt mixtures in Mexico), (Licentiate thesis). Universidad de las Américas Puebla. http://catarina.udlap.mx/u_dl_a/tales/documentos/lic/caceres_m_ca/

Geber, R., & Gömze, L. (2010). Characterization of mineral materials as asphalt fillers. *Materials Science Forum*, 659, 471-476. https://doi.org/10.4028/www.scientific.net/MSF.659.471

Huamán, N., & Chang, C. (2016). *La deformación permanente en las mezclas y el consecuente deterioro de los pavimentos asfálticos en el Perú* (Permanent deformation in mixtures and the consequent deterioration of asphalt pavements in Peru). *Perfiles de ingeniería*, 11 (11), 23-31. https://doi.org/10.31381/perfiles_ingenieria.v2i11.402

Kaliakin, V., Mashayekhi, M., & Nieto-Leal, A. (2014). The time- and temperature-related behavior of clays: Microscopic considerations and macroscopic modelling. In L. R. Wesley (Ed.), Clays and clay minerals: Geological origin, mechanical properties and industrial applications (pp 1-44), Nova Publishers.

Minaya, S., & Ordoñez, A. (2001). *Manual de laboratorio — Ensayos para pavimentos: Ensayos y agregados para pavimentos* (Laboratory manual — tests for pavements: Tests and aggregates for pavements). Universidad Nacional de ingeniería (UNI), Lima, Perú. https://www.academia.edu/6949875/MANUAL_DE_ENSAYOS_PARA_PAVIMENTOS

Rae, J., & Parker, A. (1998). Environmental Interactions of Clays: Clays in Environmental Studies. IN J. Rae and A. Parker (Eds.), Environmental Interactions of Clays: Clays and the Environment. (pp 1-5). Springer.

Vignolo, C. (1943). *Vías de comunicación en el Perú* (Communication routes in Peru). *Revista de la Universidad Católica del Perú*, 2, 81-91. https://repositorio.pucp.edu.pe/index/bitstream/handle/123456789/53462/vias%20de%20comunicacion%20en%20el%20peru.pdf?sequence=1&isAllowed=y

Whitehead, E. V. (2005). Asphaltenes and asphalts. In T. F. Yen and G. V. Chilingarian (Eds.), Fuel oil chemistry and asphaltenes (pp 95-108), Elsevier.

Author Information

Jenny Aleida Montoya Burga
[1]*Universidad César Vallejo*.
Av. Víctor Larco 1770, Trujillo, La libertad, Perú.
[2]*Laboratorio de Análisis de Suelos, Facultad de Ciencias Físicas, UNMSM*.
Av. Germán Amézaga 375, Cercado de Lima, Perú.
Contact e-mail:*jmontoyab@ucvvirtual.edu.pe*

Jorge Aurelio Bravo Cabrejos
Laboratorio de Análisis de Suelos, Facultad de Ciencias Físicas, UNMSM.
Av. Germán Amézaga 375, Cercado de Lima, Perú.

Marlon Gastón Farfán-Córdova
Universidad César Vallejo.
Instituto de Investigación en Ciencia y Tecnología.
Av. Víctor Larco 1770, Trujillo, La libertad, Perú.

María Luisa Cerón Loayza
Laboratorio de Análisis de Suelos, Facultad de Ciencias Físicas, UNMSM. Av. Germán Amézaga 375, Cercado de Lima, Perú

Felipe Américo Reyes Navarro
Laboratorio de Análisis de Suelos, Facultad de Ciencias Físicas, UNMSM.
Av. Germán Amézaga 375, Cercado de Lima, Perú.

To cite this article:

Montoya Burga, J.A., Bravo Cabrejos, J.A., Farfán-Córdova, M.G., Cerón Loayza, M.L., & Reyes Navarro, F.A. (2022). Mineralogical and elemental characterization of conventional asphalt of Peruvian roadways by x-ray diffractometry and energy dispersive x-ray fluorescence. *The Eurasia Proceedings of Science, Technology, Engineering & Mathematics (EPSTEM), 18,* 22-27.

The Eurasia Proceedings of Science, Technology, Engineering & Mathematics (EPSTEM)
ISSN: 2602-3199

The Eurasia Proceedings of Science, Technology, Engineering & Mathematics (EPSTEM), 2022

Volume 18, Pages 28-36

ICBASET 2022: International Conference on Basic Sciences, Engineering and Technology

Development of Two-Dimensional Thermal Analysis Code for the Analysis of 3D Printed PLA Parts

Buryan APACOGLU-TURAN
İstanbul Technical University

Kadir KIRKKOPRU
İstanbul Technical University

Abstract: Fused Deposition Modelling is one of the main 3D printing methods to manufacture plastic parts. The strength of the printed part by FDM is dependent on polymer diffusion between printed layers. The polymer diffusion between two neighboring layers occur not only during the extrusion of the hot top layer, but also during the production of consecutive layers due to thermal conduction. The heat diffusion from upper layers enhances the curing of polymers, which consequently affects the strength of the part. Therefore, the history of the temperature variations - curing time and curing temperature - should be analyzed to predict the strength of the part. The goal of this study is to develop a two-dimensional transient thermal analysis solver for the investigation of time-dependent thermal changes during the printing process. This solver is developed with the use of finite difference method employed under implicit scheme. The transient temperature pattern is qualitatively compatible to the experimental results in literature. The solver can be utilized for further thermal analyses to correlate temperature, polymer diffusion and strength with the inclusion of deposition path in the third dimension.

Keywords: Heat transfer, Simulation, Computational methods, Additive manufacturing, Polymers

Introduction

Additive manufacturing technologies have been developing in recent years. In three-dimensional printers, which can be of different types for different types of materials, Fused-Deposition Modeling (FDM) is widely used to produce plastic parts. In this method, plastic filaments are melted through a moving nozzle and laid in layers on a surface. The polymer structures inside the plastic layers provide this adhesion by diffusing from one layer to the next (Wool & O'Connor, 1981).

Thanks to this approach, rapid prototyping can be performed with low costs. When compared to traditional manufacturing technologies such as CNC, it is seen that FDM method is a production method that consumes much less energy and generates much less waste (Faludi, Bayley, Boghal, & Iribarne, 2015). On the other hand; quality problems are observed in parts produced with FDM (Bikas, Stavropoulos, & Chryssolouris, 2016). The high durability of the part that comes out at the end of the production process depends on the completion of the diffusion of polymers (Bartolai, Simpson, & Xie, 2018). The ratio of the strength (σ_{weld}) of the part produced by FDM to the strength (σ_∞) of the bulk part with fully developed bonds gives the Bonding Degree (D_h) (Yang & Pitchumani, 2002):

$$D_h(t) = \frac{\sigma}{\sigma_\infty} \qquad (1)$$

According to Edward; a polymer is contained in a virtual tube where it does not interact with other polymers around it (Edward, 1988). The time required for the polymer to come out of this tube is called the reptation time (τ_{rep}). Materials that exceed the reptation time are able to form bonds that provide strength. According to Edward's Tube Theory; the shorter the reptation time, the faster the binding occurs. The reptation time is affected by the temperature of the polymer-polymer interlayer and the time-dependent variation of its temperature. The correlation showing this situation is as follows (Bartolai, Simpson, & Xie, 2018) :

$$D_h(t) = \frac{\sigma_{weld}}{\sigma_{UTS}} \quad (2)$$

In polymer-polymer interlayers that do not reach the reptation time, the durability (σ_{weld}) becomes lower. The welding time of the parts that cannot reach the reptation time is shown with t_{weld}. σ_{weld} is proportional to $(t_{weld})1/4$ (Jud, Kausch, & Williams, 1981). With the help of this relation, the expression for the degree of bonding can be written in terms of times as follows:

$$\frac{\sigma_{weld}}{\sigma_{UTS}} = \left(\frac{t_{weld}}{\tau_{rep}}\right)^{1/4} \quad (3)$$

The main reason for quality problems is the variation of interlayer bond strength (polymer diffusion) depending on temperature and time-dependent changes in temperature (Yang & Pitchumani, 2002). In addition, the temperature in the interlayers and the history of temperature change affect the t_{weld}. For example; while the manufacturing process is at layer 30, how the temperature in layer 5 changes or rises above the glass transition temperature (T_g) will affect bonding. Hence, it is important to monitor the temperature of each layer during the production process. Time intervals above T_g at different layers should be examined for the estimation of bonding degree. It is expected that the layer with the shortest binding time will have the weakest point.

In an experimental study (Coogan & Kazmer, Bond and part strength in fused deposition modeling, 2017) it was observed that the strength of the upper layers was higher in the production scenario tested. It is stated that a comprehensive heat transfer analysis model and software is needed to predict which layer is the weakest in different scenarios. The authors in another study (Coogan & Kazmer, Healing simulation for bond strength prediction of FDM, 2017) modeled the top 2 layers by making 1-dimensional heat transfer calculation and stated that a two-dimensional analysis including fiber thickness should be performed. In scope of this study, a two-dimensional transient heat transfer analysis code is developed. The effect of parameters related to heat transfer during FDM, such as extrusion temperature, layer thickness, heating-cooling profile, production speed, substrate (base platform) surface temperature, should be examined.

Computational Methodology

Governing Equation and Discretization

Time-dependent heat diffusion equation is used to calculate transient temperature values inside a solid domain (Equation 4) (Bergman & Adrienne, 2017). Note that below equation assumes that conductivity of the material is constant and uniform.

$$\frac{\partial^2 T}{\partial x^2} + \frac{\partial^2 T}{\partial y^2} + \frac{\partial^2 T}{\partial z^2} + \frac{q}{k} = \frac{\rho c_p}{k}\frac{\partial T}{\partial t} \quad (4)$$

Here *x, y, z, T, ρ,* c_p*, q, k, t* denotes x-coordinate, y-coordinate, z-coordinate, temperature, density of the polymer, specific heat of the polymer, volumetric heat generation rate, conductivity of the polymer and time, respectively.

Simplified version of this equation with no-heat generation assumption and two-dimensional approximation, the equation reduces to Equation 5:

$$\frac{\partial^2 T}{\partial x^2} + \frac{\partial^2 T}{\partial y^2} = \frac{\rho c_p}{k}\frac{\partial T}{\partial t} \quad (5)$$

With second-order central difference discretization in space, first-order backward difference in time, and implicit solution scheme, discretized form of the equation is obtained as follows:

$$\frac{T^n_{i-1,j} - 2T^n_{i,j} + T^n_{i+1,j}}{(\Delta x)^2} + \frac{T^n_{i,j-1} - 2T^n_{i,j} + T^n_{i,j+1}}{(\Delta y)^2} = \frac{\rho c_p}{k}\frac{T^n_{i,j} - T^{n-1}_{i,j}}{\Delta t} \qquad (6)$$

Equation 6 contains *i* and *j* indices for the nodes representing discretization on x and y coordinates as shown in Figure 1. The superscripted index *n* denotes discretion in time. *Δx*, *Δy* and *Δt* are mesh sizes on x-direction, y-direction, and time.

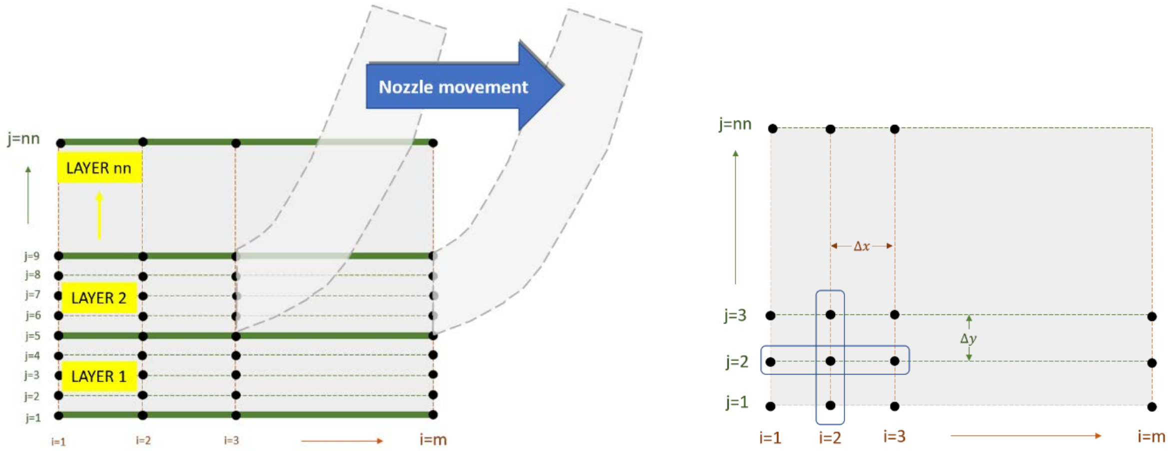

(a) (b)

Figure 1. Domain and nozzle movement (a), Stencil of discretization (b)

With the help of the scheme in Equation 6 for discretization at all nodal locations, multiple equations are obtained. Total number of unknowns (nodal temperatures) are equal to the total number of equations and these equations constructs a matrix system. Note that coefficients of nodal temperatures at nth time, so called *a*, *b*, *c* in Equation 4, and nodal temperature at (n-1)th time step are known values.

$$a\,T^n_{i,j} + b\,T^n_{i-1,j} + b\,T^n_{i+1,j} + c\,T^n_{i,j-1} + c\,T^n_{i,j+1} = T^{n-1}_{i,j} \qquad (7)$$

$$\begin{bmatrix} a & b & & & & c & . & c & \\ b & a & b & & & & c & . & c \\ & b & a & b & & & & c & . \\ & & b & a & b & & & & c \\ c & & & b & a & b & & & \\ . & c & & & b & a & b & & \\ c & . & c & & & . & . & . & \\ & . & . & . & & & . & . & . \\ & & c & . & c & & & b & a \end{bmatrix} \begin{bmatrix} T^n_{1,1} \\ T^n_{2,1} \\ T^n_{3,1} \\ \vdots \\ \vdots \\ . \\ T^n_{m,nn} \end{bmatrix} = \begin{bmatrix} T^{n-1}_{1,1} \\ T^{n-1}_{2,1} \\ T^{n-1}_{3,1} \\ \vdots \\ \vdots \\ . \\ T^{n-1}_{m,nn} \end{bmatrix} \qquad (8)$$

Where $a = (1 + 2Fo_x + 2Fo_y)$, $b = -Fo_x$, $c = -Fo_y$.

Dimensionless numbers in these coefficients are defined as $Fo_x = \frac{\alpha\Delta t}{(\Delta x)^2}$, $Fo_y = \frac{\alpha\Delta t}{(\Delta y)^2}$ where $\frac{k}{\rho c_p} = \alpha$.

The matrix system in Equation 8 has a form A X = B, where A is the coefficient matrix, X is unknown vector and B is known vector. Solving this matrix equation, nodal temperatures at nth time are obtained by using the temperature values in the previous time step (n-1). The calculation procedure starts with the utilization of initial temperature at t=0 sec as an initial condition and progresses until the end time of the simulation. In other words, by replacing the newly obtained X-vector with the B-vector, the solution advances in time (using n=0 as starting point for n=1, using n=1 for n=2, and so on).

The coefficient matrix (A) can be created with the help of a code and the matrix equation can be solved in a computer environment with the do-loops as marching in time. In scope of this study, a special code is developed by using Fortran 90 programming language to analyze heat transfer in a growing solid domain continuously changing boundaries and boundary conditions. In addition, the GMRES matrix solver (Turan & Ecder, 2011), which employs Newton-Krylov Method (Brown & Saad, 1989), is utilized to speed up the calculation process.

Initial and Boundary Conditions

The general representation of the applied boundary conditions is depicted in Figure 2.

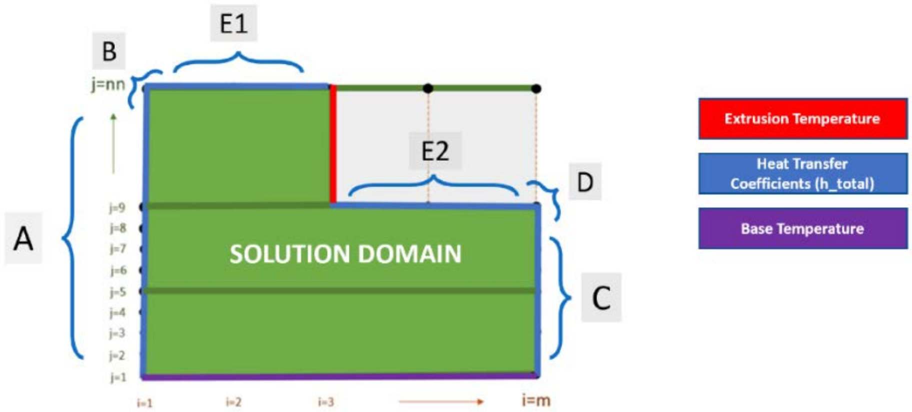

Figure 2. Boundary conditions

Blue lines in Figure 2, which consists of A, B, C, D, E1, E2 edges and corners, are subjected to an effective heat transfer coefficient that embodies convection and radiation heat transfer coefficients. After some algebraic manipulation, the concluding boundary equations are given in Table 1.

$$Q = h_{effective}A\left(T_{i,j}^{n} - T_{\infty}\right) \tag{9}$$

$$h_{effective} = h_{radiation} + h_{convection} \tag{10}$$

$$h_{radiation} = \left(T_{i,j}^{n-1} + T_{\infty}\right)\left[\left(T_{i,j}^{n-1}\right) + T_{\infty}^{2}\right] \tag{11}$$

$$Bi_x = \frac{h_{effective}\Delta x}{k} \tag{12}$$

$$Bi_y = \frac{h_{effective}\Delta y}{k} \tag{13}$$

Table 1. Equations at boundaries with heat transfer coefficients

1. A 2. Left Edge	3. 4. $\left(2Fo_x + 2Fo_y + 2Bi_xFo_x + 1\right)T_{i,j}^{n} - 2Fo_xT_{i+1,j}^{n} - Fo_yT_{i,j-1}^{n} - Fo_yT_{i,j+1}^{n} = 2Bi_xFo_x\,T_{\infty} + T_{i,j}^{n-1}$ 5.
6. B 7. Top-Left Corne	8.

	9. $\left(2Fo_x + 2Fo_y + 2Bi_xFo_x + 2Bi_yFo_y + 1\right)T_{i,j}^{n} - 2Fo_xT_{i+1,j}^{n} - 2Fo_yT_{i,j-1}^{n} = 2Bi_xFo_xT_{\infty} + 2Bi_yFo_yT_{\infty} + T_{i,j}^{n-}$ 10.
11. C 12. Right Edge	13. 14. $\left(2Fo_x + 2Fo_y + 2Bi_xFo_x + 1\right)T_{i,j}^{n} - 2Fo_xT_{i-1,j}^{n} - Fo_yT_{i,j-1}^{n} - Fo_yT_{i,j+1}^{n} = 2Bi_xFo_xT_{\infty} + T_{i,j}^{n-1}$ 15.
16. D 17. Top-Right Corner	18. 19. $\left(2Fo_x + 2Fo_y + 2Bi_xFo_x + 2Bi_yFo_y + 1\right)T_{i,j}^{n} - 2Fo_xT_{i-1,j}^{n} - 2Fo_yT_{i,j-1}^{n} = 2Bi_xFo_xT_{\infty} + 2Bi_yFo_yT_{\infty} + T_{i,j}^{n}$ 20.
21. E1 & E2 22. Top Edge	23. 24. $\left(2Fo_x + 2Fo_y + 2Bi_yFo_y + 1\right)T_{i,j}^{n} - Fo_xT_{i+1,j}^{n} - Fo_xT_{i-1,j}^{n} - 2Fo_yT_{i,j-1}^{n} = 2Bi_yFo_yT_{\infty} + T_{i,j}^{n-1}$ 25.

Note that radiative heat transfer coefficient is calculated by using the nodal temperature in previous time step.

In Figure 2, the extrusion temperature is shown as red line to define primary heat source. The boundary condition on this edge is applied as $T_{i,j}^{n} = T_{extrusion}$ Same approach is employed for the base temperature, which is a constant value, $T_{i,j}^{n} = T_{base}$

Parameters for Preliminary Analysis

Assumptions:

- The temperature of the melted plastic coming from the nozzle is constant.
- Material properties are homogenous inside the solution domain.

Boundary Conditions:

- The extrusion temperature is equal to 210 ℃.
- Base temperature is 60 ℃.
- Air temperature is assumed to be 20 ℃.
- The speed of nozzle (production speed) is 60 mm/s.

Material Properties:

Temperature-dependent material properties are used for the accurate calculation of matrix coefficients. Fitted equations to the property data provided in literature (Sin, Rahmat, & Rahman, 2012) are as follows:

- Conductivity (T in Kelvin), k=0.130 W/m-K
- Specific Heat of PLA;
  For T > 330 K; c_p (J/kg-K) = 1.031698*T + 1677.2415
  For T < 330 K; c_p (J/kg-K) = 3.969*T + 159.72
- Density of PLA (T in Celsius);
  ρ (kg/m^3) = 1240 kg/m^3

The Geometry and Computational Parameters:

- X-direction: Width of the part is 19 mm, and it is divided into 10 segments (Δx=1.9 mm).
- Y-direction: Layer thickness is 0.3 mm, and the total height is 25 mm which approximately corresponds to printing of 80 layers. Each layer (0.3 mm) is discretized by 3 nodes to resolve layer thickness (Δy=0.10 mm).
- Time: The algorithm is designed to advance 1 node at every time step. The time step size, Δt=Δx/speed, is calculated as 0.03167 seconds.

Between consecutive layers, a time delay is defined to allow cooling process taking place during the production in third dimension. Intra-layer printing time is calculated with considering total area to be printed at each layer. With using the geometrical parameters, intra-layer delay is estimated as 3.8 seconds that corresponds to 120 time steps/layer. Following the completion of the printing process, an ultimate cooling time of 1,600 steps (~50 seconds between 10,280th and 11,880th time steps) is defined after the completion of the printing to observe cool down.

Results and Discussion

Preliminary Simulation Results

Preliminary results are obtained with the assumption that convective heat transfer coefficient is equal to 500 W/m^2-K and T_{base}=60 ℃. Contour plots in Figure 3 visualize temperature changes inside the printed part at different timesteps. Heat diffusion inside the domain, cooling effects from top, left and right boundaries are clearly observed. Thermal energy deposited during the printing process keeps layers above T_g at hotter locations. Note that T_g is between 50 ℃ and 80 ℃ for PLA (Matyjaszewski & Möller, 2012).

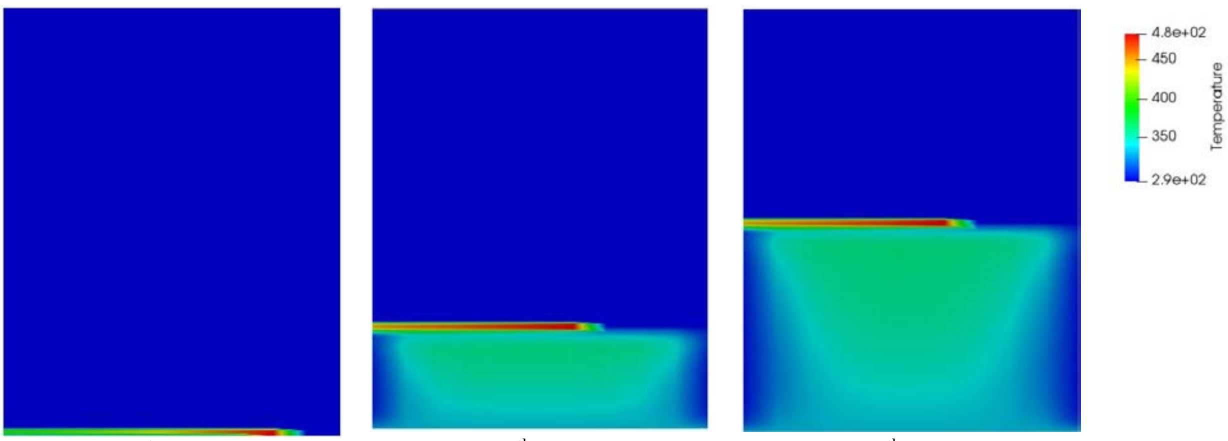

1st layer 20th layer 40th layer

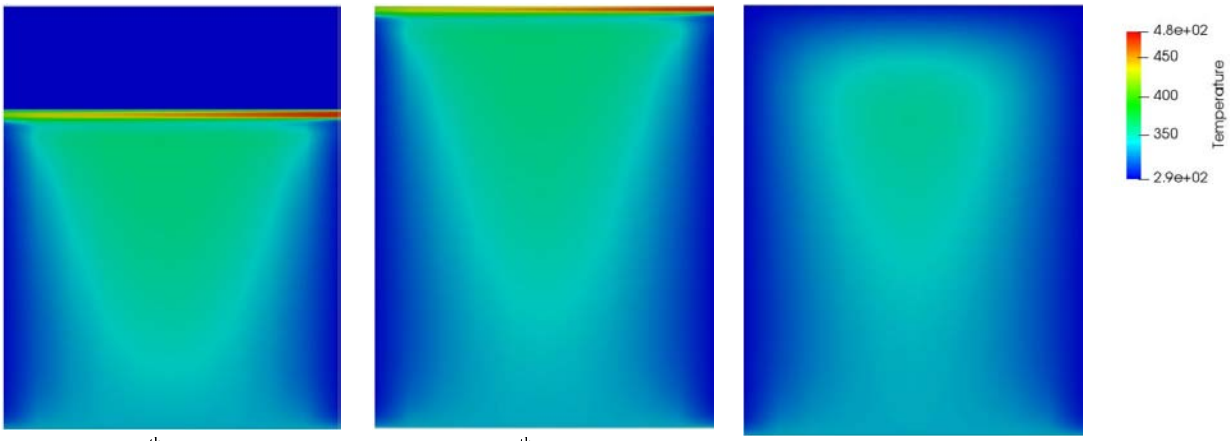

60th layer 80th layer Cool down for 50 sec.

Figure 3. Computed temperature contour plots at different time steps (T in Kelvins)

Time history of nodal temperatures at the center of 2nd, 20th, 40th and 60th layers are given in Figure 4.

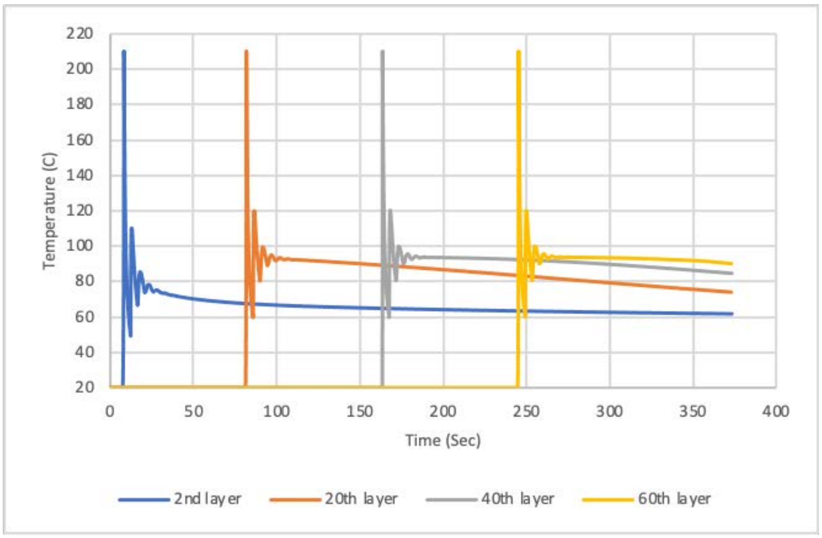

Figure 4. Nodal temperatures at the center node of layers

An experimental study in literature experimentally analyzed the effect of processing conditions on the bonding quality of FDM polymer filaments (Sun, Rizvi, Bellehumeur, & Gu, 2008). The time history of temperature data shows peaks with frequencies dependent on the printing speed and the printing path.

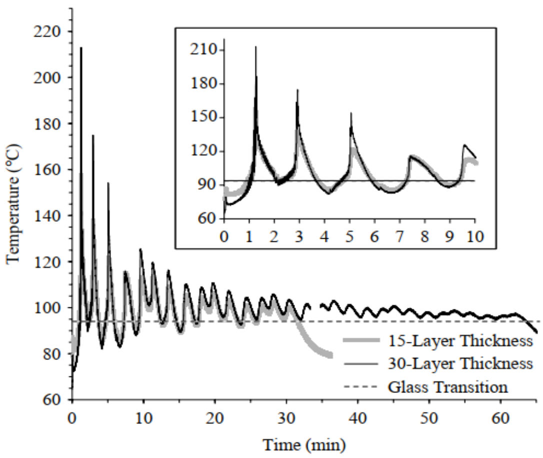

Figure 5. The time history of the measured temperature by k-type thermocouple during FDM (Sun, Rizvi, Bellehumeur, & Gu, 2008)

Conclusion

In scope of this study, a Fortran code is developed for the modeling of transient two-dimensional heat diffusion equation to understand history of temperature during 3D printing process via FDM. A matrix equation is obtained at each time step due to implicit time scheme which assures convergence of the solution regardless of the mesh size. The matrix is solved with the help of Newton-Krylov algorithm at each time step. A delay time is defined between layers and matrix is solved under convection and radiation boundary conditions at this time interval to consider the cool down period due to continuing extrusion process in the third dimension at the same layer.

During the simulation of the printing process, convection and radiation boundary conditions are applied to capture accurate cooling rate. 500 W/m^2-K as the convective heat transfer coefficient (HTC) is applied to see the cooling pattern clearly. This number is the upper limit of the generic range of convection coefficients of air; 2.5-25 W/m^2-K for natural convection, and 100-500 W/m^2-K for forced convection (Kosky, Balmer, Keat, & Wise, 2013). It is important to remark that this elevated HTC intrinsically compensates lacking cooling effects in the third dimension which is expected to have the highest contribution to the overall heat transfer since front and back surfaces have relatively large areas compared to the other sides.

The two-dimensional code can be calibrated with the use of measured temperatures via infrared camera. Then, the calibrated code can be used for the estimation of t_{weld}, total welding time above glass temperature, at different production parameters. A t_{weld}-σ correlation can be developed with tensile tests of the parts that are manufactured under corresponding production parameters. The authors continue to work tensile tests for the determination of a t_{weld}-σ correlation for PLA.

Recommendations

As a future work, modeling of the third dimension with actual printing path is recommended. Convection from back and front surfaces contributes to cooling which has an impact on time history of temperatures. Further improvement of the code to include discretization of the third dimension may result in more accurate estimation of t_{weld}.

Scientific Ethics Declaration

The authors declare that the scientific ethical and legal responsibility of this article published in EPSTEM journal belongs to the authors.

Acknowledgements and Notes

* This article was presented as an oral presentation at the International Conference on Basic Sciences, Engineering and Technology (www.icbaset.net) conference held in Istanbul/Turkey on August 25-28, 2022.

* This research was supported by Simularge A.Ş. and its cloud infrastructure to run developed algorithms. We thank Dr. Erhan TURAN, CTO of Simularge A.Ş., for his insights that greatly assisted the research.

References

Bartolai, J., Simpson, J., & Xie, R. (2018). Predicting strength of additively manufactured thermoplastic polymer parts produced using material extrusion. *Rapid Prototyping Journal*, *24*(2), 321-332.

Bergman, T. L., & Adrienne, L. S. (2017). *Fundamentals of Heat and Mass Transfer.* Wiley.

Bikas, H., Stavropoulos, P., & Chryssolouris, G. (2016). Additive manufacturing methods and modelling approaches: a critical review. *Int. J. Adv. Manuf. Technology,*, *83*, 389-405.

Coogan, T., & Kazmer, D. (2017). Bond and part strength in fused deposition modeling. *Rapid Prototyping Journal*, *23*(2), 414-422.

Coogan, T., & Kazmer, D. (2017). Healing simulation for bond strength prediction of FDM. *Rapid Prototyping Journal*, *23*(3), 551-561.

Faludi, J., Bayley, C., Boghal, S., & Iribarne, M. (2015). Comparing environmental impacts of additive manufacturing vs. traditional machining via life-cycle assessment. *Rapid Prototyping Journal, 21*(1), 14-33.

Jud, K., Kausch, H., & Williams, J. (1981). Fracture mechanics studies of crack healing and welding polymers. *Journal of Materials Science, 16*(1), 204-210.

Kosky, P., Balmer, R., Keat, W., & Wise, G. (2013). Mechanical engineering. In *Exploring Engineering - an Introduction to Engineering and Design* (p. 264). Academic Press.

Matyjaszewski, K., & Möller, M. (2012). *Polymer science: a comprehensive reference.* Elsevier Science.

Sin, L. T., Rahmat, A. R., & Rahman, W. W. (2012). *PLA handbook series: polylactic acid - pla biopolymer technology and applications.* Plastics Design Library.

Sun, Q., Rizvi, G., Bellehumeur, C., & Gu, P. (2008). Effect of processing conditions on the bonding quality of FDM polymer filaments. *Rapid Prototyping Journal, 14*(2), 72-80.

Turan, E., & Ecder, A. (2011). Analysis of a bimetallic slab in non-isothermal flow. *Proceedings of the Institution of Mechanical Engineers, Part C: Journal of Mechanical Engineering Science, 225*(3), 658-672.

Wool, R., & O'Connor, K. (1981). A theory of crack healing in polymers. *Journal of Applied Physics*, *52*, 5953-5963.

Yang, F., & Pitchumani, R. (2002). Healing of thermopastic polymers at an interface under nonisothermal conditions. *Macromolecules, 35*, 3213-3224.

Author Information

Buryan Apacoglu-Turan
Istanbul Technical University
Faculty of Mechanical Engineering, Türkiye
Contact e-mail: *apacoglu@itu.edu.tr*

Kadir Kirkkopru
Istanbul Technical University
Faculty of Mechanical Engineering, Türkiye

To cite this article:

Apacoglu-Turan, B. & Kirkkopru, K. (2022). Development of two-dimensional thermal analysis code for the analysis of 3D printed PLA parts. *The Eurasia Proceedings of Science, Technology, Engineering & Mathematics (EPSTEM), 18,* 28-36.

The Eurasia Proceedings of Science, Technology, Engineering & Mathematics (EPSTEM)
ISSN: 2602-3199

The Eurasia Proceedings of Science, Technology, Engineering & Mathematics (EPSTEM), 2022

Volume 18, Pages 37-45

ICBASET 2022: International Conference on Basic Sciences, Engineering and Technology

Finite Element Method for Analysis of Off-Center Connected Continuous Beams

Albena DOICHEVA
University of Architecture, Civil Engineering and Geodesy (UACEG)

Abstract: The study of the structural elements goes through the premise of their centric support and centric connection. In reality, it is common to see elements with different cross-sections connected by offset axes, for example to align some of their edges, or those that are supported with off-center supports. Such inter-element eccentricities and off-center supports leads to a change in the stress-strain state from the traditional ones known from the available literature and university textbooks. In previous publications with participation of the author, exact nonlinear and approximate analytic solutions of similar problems for beams under various loading, support and connection conditions have already been published. The finite element method provides an approximate approach for computer analysis. In this paper, results obtained through a computer program created in the MATLAB, based on a finite element accounting for eccentricity in connection and off-centering of support, are demonstrated. The results shows values in the diagrams of internal forces differing by up to 15-30% compared to the classical theory of centric connection and centric supporting.

Keywords: Continuous beam, Different cross-sections, Inter-element eccentricities, Off-center supports, Finite element method

Introduction

In construction practice, it is often assumed that beams and systems of bodies are connected under the premise of their axial support and axial connection. In real structure, however, there is often a divergence from this assumption. The presence of different operating conditions of the structural elements causes the emergence of a more special stressed and strained state. This is proven in a number of studies with the participation of the author (Mladenov & Doicheva, 2011; Doicheva & Mladenov, 2009). Inferences were made in both, linear and non-linear analysis. The latter case is based on the exact differential equation of the deformed beam axis

$\frac{d^2\varphi_i}{ds_i^2} + \frac{F_i}{EI}\left(1 - \frac{F_i}{EA}\cos\varphi_i\right)\sin\varphi_i = 0$ and the elastic analogy theorem (Mladenov, 1985-86).

The practical application of the obtained results requires an approach applicable to modern computing technology. Over the past few decades, the finite element method (Bankov & Pavlova 1989; Gallagher, 1984; Bhatti, 2005) has proven to be a reliable means of solving complex stress and strain states. In this paper FEM will be used to study continuous beams without and with joints. However, a corresponding finite element is required for this purpose. A stiffness matrix of such a beam-type finite element was obtained by the force method in (Mladenov et al., 2011-2012). Another so-called direct approach will be applied here (Gallagher, 1984; Gavin, 2011).

Method

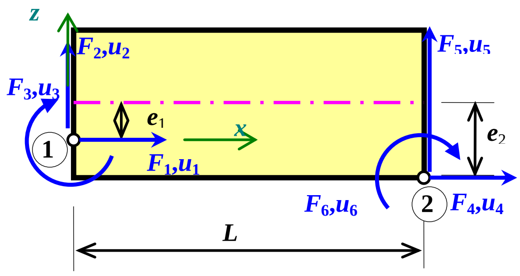

Figure 1. Finite element for unsymmetrical support with nodal forces and displacements

Figure 1 presents the type of finite element with length L, eccentricities e_1 and e_2, respectively, at nodes *1* and *2*, nodal forces, nodal moments as well as unknown displacements and unknown rotations. From now on, for brevity, we will only talk about nodal forces and displacements in a generalized sense. The element is subjected to special bending and normal force. The physico-mechanical characteristics of the cross-section are: E - modulus of elasticity, I - principal moment of inertia, A - area of the cross-section and $i = \sqrt{I/A}$ - radii of gyration.

Derivation of Stiffness Matrix by Direct Approach

The fields of displacements (Gallagher, 1984) $u(x) = a_1 x + a_2$; $w(x) = a_3 x^3 + a_4 x^2 + a_5 x + a_6$ with $w'(x) = 3a_3 x^2 + 2a_4 x + a_5$ have values for the endpoints respectively:

$$u(0) = a_2; u(L) = a_1 L + a_2;\ w'(0) = a_5; u_3 \approx -w'(0);\ w'(L) = 3a_3 L^2 + 2a_4 L + a_5; u_6 \approx -w'(L) \tag{1}$$

On the other hand (Figure 1),

$$u(0) = u_1 + e_1 u_3 = u_1 - e_1 w'(0) = u_1 - e_1 a_5, \qquad \text{and} \qquad u(L) = u_4 + e_2 u_6 = u_4 - e_2 w'(L) = u_4 - e_2\left(3a_3 L^2 + 2a_4 L + a_5\right).$$

From here follows the relation $\{\mathbf{u}\} = [\mathbf{B}]\{\mathbf{a}\}$; $\mathbf{det(B)} = -L^5$, from where for the coefficients of the displacement functions we can write $\{\mathbf{a}\} = \left[\mathbf{B}^{-1}\right]\{\mathbf{u}\}$, therefore:

$$\begin{Bmatrix} a_1 \\ a_2 \\ a_3 \\ a_4 \\ a_5 \\ a_6 \end{Bmatrix} = \begin{bmatrix} -1/L & 1/L & 0 & -e_1/L & 0 & e_2/L \\ 1 & 0 & 0 & e_1 & 0 & 0 \\ 0 & 0 & 2/L^3 & -1/L^2 & -2/L^3 & -1/L^2 \\ 0 & 0 & -3/L^2 & 2/L & 3/L^2 & 1/L \\ 0 & 0 & 0 & -1 & 0 & 0 \\ 0 & 0 & 1 & 0 & 0 & 0 \end{bmatrix} \begin{Bmatrix} u_1 \\ u_4 \\ u_2 = (w_1) \\ u_3 = (\alpha_1) \\ u_5 = (w_2) \\ u_6 = (\alpha_2) \end{Bmatrix} \tag{2}$$

Thus, the longitudinal displacement as a function of the nodal displacements is $u(x) = (u_4 - u_1 + e_2 u_6 - e_1 u_3)\, x / L + u_1 + e_1 u_3$, and for the axial linear strain is written $\varepsilon_x = u'(x) = (u_4 - u_1 + e_2 u_6 - e_1 u_3)/L$. Using Hooke's law, the normal stress and hence the normal force in the beam is determined:

$$\mathsf{N} = \sigma_x A = EA\varepsilon_x = \frac{EA}{L}\lfloor -1 \quad 1 \quad 0 \quad -e_1 \quad 0 \quad e_2 \rfloor \{\mathbf{u}\} \tag{3}$$

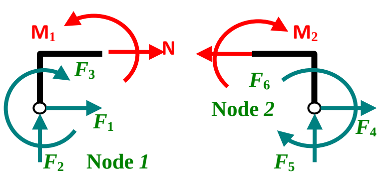

Figure 2. Internal forces at the finite element boundary

On the other hand, the relationship between the normal force and the nodal forces is (see figure 2) $F_{1/4} = \mp N$, so:

$$\begin{Bmatrix} F_1 \\ F_4 \end{Bmatrix} = \frac{EA}{L} \begin{bmatrix} 1 & -1 & 0 & e_1 & 0 & -e_2 \\ -1 & 1 & 0 & -e_1 & 0 & e_2 \end{bmatrix} \{\mathbf{u}\} \tag{4}$$

The following coefficients a_3, a_4, a_5, a_6 are expressed by (2)

$$a_3 = \frac{2u_2}{L^3} - \frac{u_3}{L^2} - \frac{2u_5}{L^3} - \frac{u_6}{L^2}; \quad a_4 = -\frac{3u_2}{L^2} + \frac{2u_3}{L^2} + \frac{3u_5}{L^2} + \frac{u_6}{L^2}; \quad a_5 = -u_3; \quad a_6 = u_2 . \tag{5}$$

Substituting (5) into the transverse displacement function yields:

$$w(x) = \left(2\frac{x^3}{L^3} - 3\frac{x^2}{L^2} + 1\right)u_2 + x\left(2\frac{x}{L} - \frac{x^2}{L^2} - 1\right)u_3 + \left(3\frac{x^2}{L^2} - 2\frac{x^3}{L^3}\right)u_5 + x\left(\frac{x}{L} - \frac{x^2}{L^2}\right)u_6 . \tag{6}$$

This result is recorded in matrix form $w(x) = \lfloor \mathbf{N} \rfloor \{\Delta\} = \lfloor N_1 \; N_2 \; N_3 \; N_4 \rfloor \{\Delta\}$, where $\{\Delta\} = \lfloor u_2 \; u_3 \; u_5 \; u_6 \rfloor^T$. N_i are called interpolation functions or shape functions (Gallagher, 1984).

The dependence between the bending moments defined in the end sections is used as follows: $M_1 = -F_1 e_1 + F_3$; $M_2 = F_4 e_2 - F_6$ and the derivatives $w''(0)$ and $w''(L)$, bearing in mind that $M(x) = EIw''(x)$, a system of two linear equations with four unknowns is obtained. Since F_1 and F_4 are already defined, from the above expressions we extract F_3 and F_6, i.e.

$$\begin{Bmatrix} F_3 \\ F_6 \end{Bmatrix} = \frac{EI}{L^3 i^2} \begin{bmatrix} L^2 e_1 & -L^2 e_1 & -6Li^2 & L^2\left(4i^2 + e_1^2\right) & 6Li^2 & L^2\left(2i^2 - e_1 e_2\right) \\ -L^2 e_2 & L^2 e_2 & -6Li^2 & L^2\left(2i^2 - e_1 e_2\right) & 6Li^2 & L^2\left(4i^2 + e_2^2\right) \end{bmatrix} \{\mathbf{u}\} . \tag{7}$$

Finally, through the expressions for F_1, F_3, F_4, F_6 and the conditions for equilibrium of the forces is found:

$$\begin{Bmatrix} F_2 \\ F_5 \end{Bmatrix} = \frac{EI}{L^3 i^2} \begin{bmatrix} 0 & 0 & 12i^2 & -6Li^2 & -12i^2 & -6Li^2 \\ 0 & 0 & -12i^2 & 6Li^2 & 12i^2 & 6Li^2 \end{bmatrix} \{\mathbf{u}\} . \tag{8}$$

Written together (4, 7, 8) give the stiffness matrix of the finite element considering the influence of only the bending moment and the normal force:

$$\begin{Bmatrix} F_1 \\ F_2 \\ F_3 \\ F_4 \\ F_5 \\ F_6 \end{Bmatrix} = \frac{1}{L^3 i^2} \begin{bmatrix} L^2 & 0 & L^2 e_1 & -L^2 & 0 & -L^2 e_2 \\ 0 & 12i^2 & -6Li^2 & 0 & -12i^2 & -6Li^2 \\ L^2 e_1 & -6Li^2 & L^2\left(4i^2 + e_1^2\right) & -L^2 e_1 & 6Li^2 & L^2\left(2i^2 - e_1 e_2\right) \\ -L^2 & 0 & -L^2 e_1 & L^2 & 0 & L^2 e_2 \\ 0 & -12i^2 & 6Li^2 & 0 & 12i^2 & 6Li^2 \\ -L^2 e_2 & -6Li^2 & L^2\left(2i^2 - e_1 e_2\right) & L^2 e_2 & 6Li^2 & L^2\left(4i^2 + e_2^2\right) \end{bmatrix} \begin{Bmatrix} EIu_1 \\ EIu_2 \\ EIu_3 \\ EIu_4 \\ EIu_5 \\ EIu_6 \end{Bmatrix} . \tag{9}$$

Geometric Stiffness Matrix

The element with pre-deformation length dx due to bending only is elongated to dl (Figure 3). Furthermore

$$dl = \sqrt{(dx)^2 + (dw)^2} \approx \left(1 + w'^2 / 2\right) dx . \tag{10}$$

Therefore, the absolute extension of the element with length dx is $dl - dx = \left(w'^2 / 2\right) dx$.

The differentially small work of the normal force from this extension will be $d\pi = \mathrm{N}(x)\left(w'^2 dx\right)/2$, and for the entire beam will be $\Pi_G = \int_0^L \left(\mathrm{N}(x) w'^2\right) dx/2$, which is exactly the potential energy of deformation.

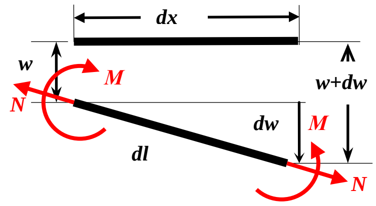

Figure 3. Infinitesimal length deformation

At a constant normal force $\mathrm{N} = N$ we will have $\left(N\int_0^L w'^2 dx\right)/2$.

$$\left(\overline{\Pi}_G = \frac{\Pi_G}{N}\right) = \frac{1}{2}\int_0^L w'^2 dx = \frac{\left(6u_2^2 - 12u_2u_5 + 6u_5^2\right)}{10L} - \frac{(u_2 - u_5)(u_3 + u_6)}{10} + L\frac{2u_3^2 - u_3u_6 + 2u_6^2}{30}. \tag{11}$$

From Castigliano's inverse theorem, we obtain the forces F_{iG}, and the geometric stiffness matrix, which is due only to the influence of a constant normal force and the bending deformation, takes the known form (Gallagher, 1984; Gavin, 2011):

$$\begin{Bmatrix} F_{1G} \\ F_{2G} \\ F_{3G} \\ F_{4G} \\ F_{5G} \\ F_{6G} \end{Bmatrix} = N\begin{bmatrix} 0 & 0 & 0 & 0 & 0 & 0 \\ 0 & 6/5L & -1/10 & 0 & -6/5L & -1/10 \\ 0 & -1/10 & 2L/15 & 0 & 1/10 & -L/30 \\ 0 & 0 & 0 & 0 & 0 & 0 \\ 0 & -6/5L & 1/10 & 0 & 6/5L & 1/10 \\ 0 & -1/10 & -L/30 & 0 & 1/10 & 2L/15 \end{bmatrix}\begin{Bmatrix} u_1 \\ u_2 \\ u_3 \\ u_4 \\ u_5 \\ u_6 \end{Bmatrix} = \frac{N}{EI}\begin{bmatrix} 0 & 0 & 0 & 0 & 0 & 0 \\ 0 & 6/5L & -1/10 & 0 & -6/5L & -1/10 \\ 0 & -1/10 & 2L/15 & 0 & 1/10 & -L/30 \\ 0 & 0 & 0 & 0 & 0 & 0 \\ 0 & -6/5L & 1/10 & 0 & 6/5L & 1/10 \\ 0 & -1/10 & -L/30 & 0 & 1/10 & 2L/15 \end{bmatrix}\begin{Bmatrix} EIu_1 \\ EIu_2 \\ EIu_3 \\ EIu_4 \\ EIu_5 \\ EIu_6 \end{Bmatrix}. \tag{12}$$

The use of the geometric stiffness matrix in addition to the basic one turns out to be very useful in the iterative determination of a critical load in frame systems in the Euler sense (Gallagher, 1984; Saouma, 2002))

Results and Discussion

The calculations were performed with a program running in the MATLAB (MATLAB R2017b) environment.

First Example

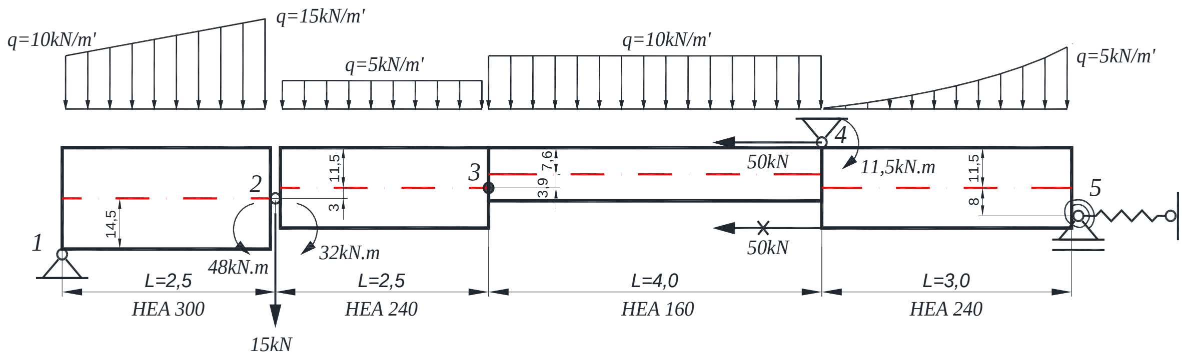

Figure 4. The joint is in the first element axis

Figure 4 shows a beam composed of 4 elements, two of which are with equal cross-section. All sections are aligned along the upper edge of the section, which leads to the divergence of their axes. The connection between the first and second section is with joint. Initially, the joint is in the first element axis. The concentrated forces and moments are introduced at the elements nodes. The stiffnesses of the linear and rotational springs are related to the stiffnesses of the beam. The linear springs is brought to the stiffness of tension (compressure) of the beam by coefficient ζ, as $k_i = \zeta_i \frac{EA_i}{L_i}$. The stiffness of the rotational springs is reduced to the bending stiffness of the beam by the coefficient γ and is $c_i = \gamma_i \frac{EI_i}{L_i}$. In the example considered are accepted $\zeta = 0,25$ and $\gamma = 0,5$.

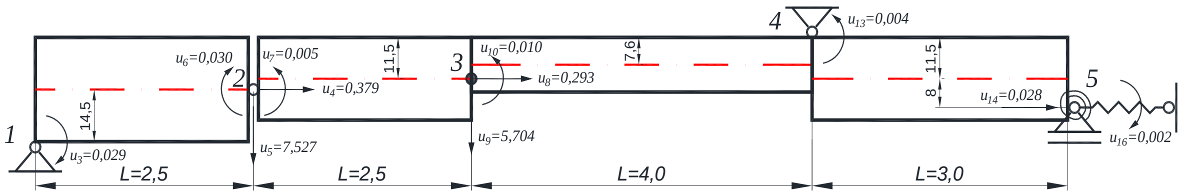

Figure 5. Displacements and rotations in the nodes

The results are shown graphically in Figure 5 and Figure 6.

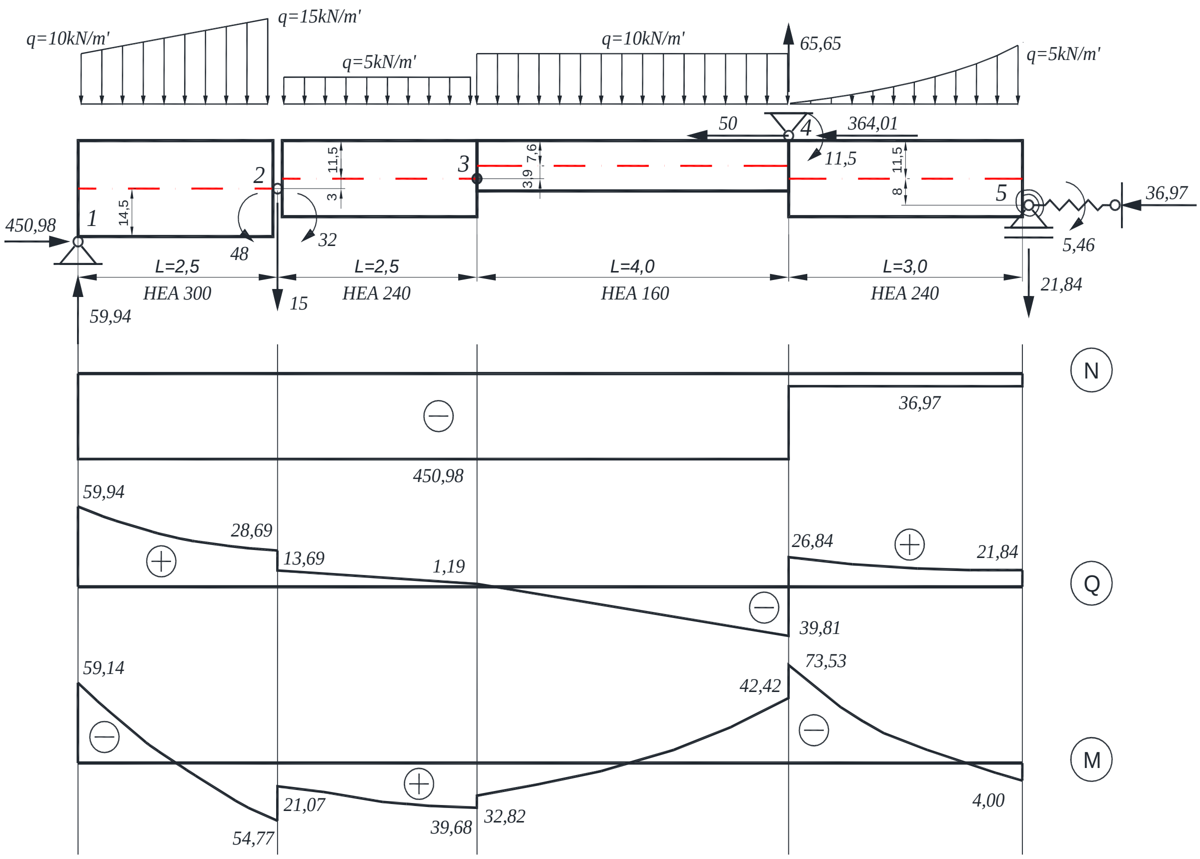

Figure 6. Initial force when the joint is in the first element axis

The second case is when the joint is located along the lower edge of the second element and all other conditions from the first case are preserved, Figure 7.

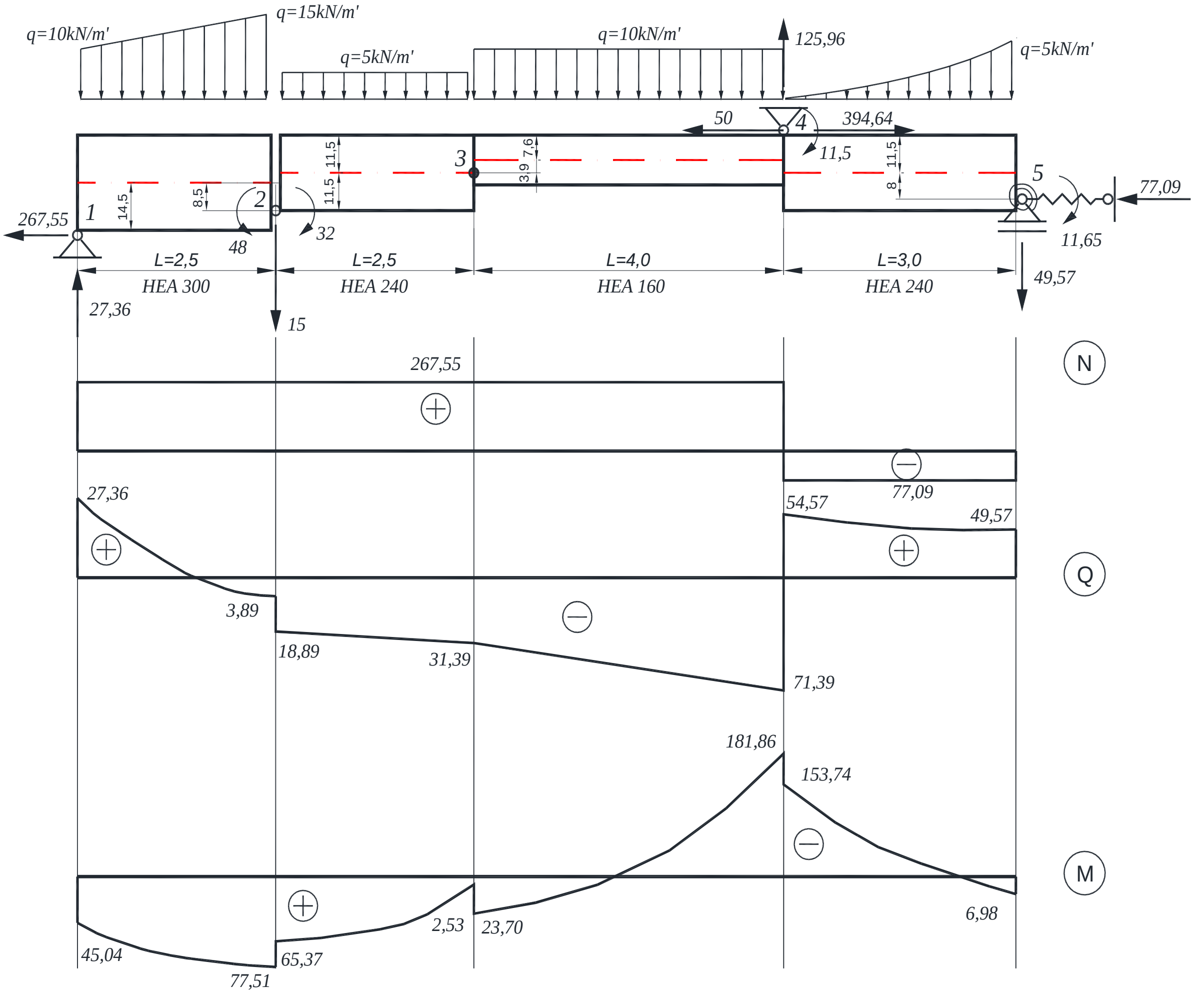

Figure 7. Beam with joint on the lower edge of the second element

In the two cases of joint position, the initial forces have different values. The large axial force is striking and the fact that if in the first case normal force is compressive, then in the second it is tensile.

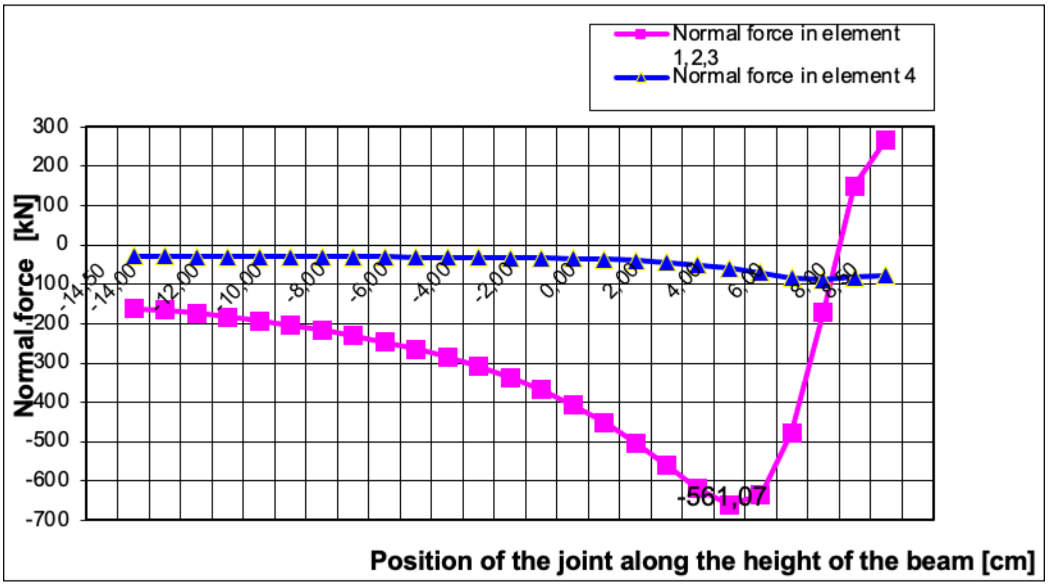

Figure 8. Change in normal force when moving the joint along the height of the beam

The limit of variation of the normal force during the displacement of the joint along the height of the beam is shown in Figure 8. When placing the joint around the upper edge on the beam, the horizontal force is compressive. This force numerically exceeds the vertical transverse loads by about two times and continues to increase as the joint moves towards the axis. The extreme value is slightly below the axis of the first element. Moving the joint to the bottom edge of a second element results in a rapid reset and reversal to the tension direction with a value commensurate with the maximum compressive force. The example is indicative for the importance of research on the different position of intermediate joints in non-axial connection and off-center support of continuous beams.

Second Example

A classic example about the occurrence of a complex stressed and strained state caused by the off-center support along the lower or upper edge is the crane beam (Figure 9).

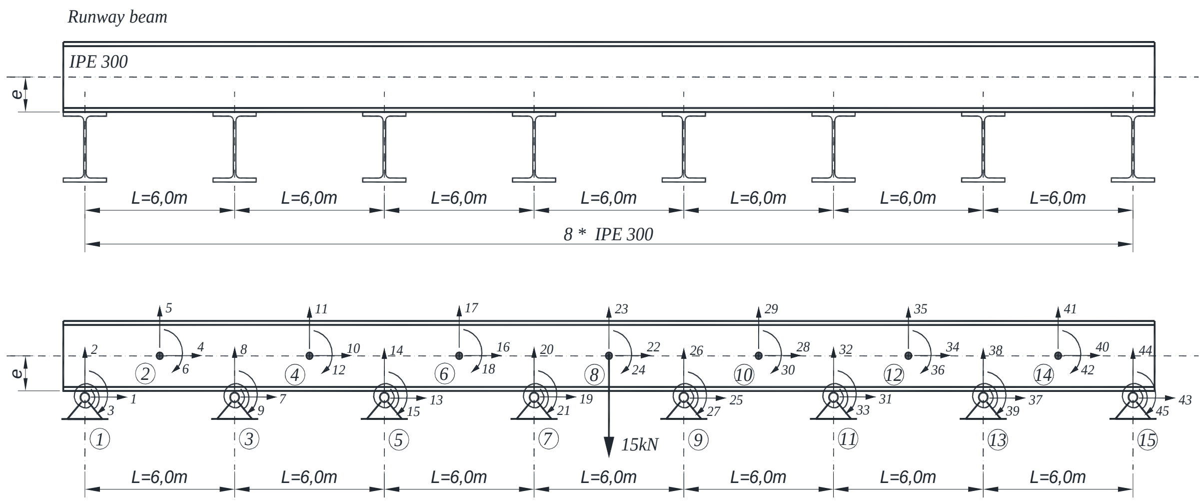

Figure 9. Crane beam

The crane beam is made of an IPE 300 profile. The crane beam is supported on an analogous profiles with a cross section of IPE 300. The bolted connections between the profiles are modeled as fixed supports. There will be a tendency to torsion on the support beams, which will lead to the occurrence of an additional moment accounted by the rotation springs in the supports. Their coefficient $c = \frac{GI_t}{L}$ has the value $c = \frac{8000.10^4.19,77.10^{-8}}{0,20} = 79,08\frac{\text{kN.m}}{\text{rad}}$. On the other hand, the coefficient of the rotation spring reduced to the bending stiffness of the beam is $c = \gamma\frac{EI}{L_i}$, where L_i is the length of the *i*-th finite element to which the stiffness of the spring is reduced. It follows that $\gamma = \frac{cL_i}{EI} = \frac{79,08.3}{2,1.10^8.8356.10^{-8}} = 0,0135$.

The results of the program are shown in Figure 10.

The large horizontal force in the loaded span of the beam, which exceeds the value of the transverse load as well as the jumps into the moment diagram in the area of the supports are striking. They are explained precisely by the displacement of the supports from the axis. If the supports were at the axis, as is commonly assumed, then the moment diagram values would be as shown by the dashed line. They differ from the real ones by 14.5% in the span of the beam and 27% in the area above the support. There is a case where, if the support is in the axis, like the classical cases, the beam will be dimensioned as a special bending. The presence of a horizontal force, however, requires that it be considered as a bending combined with tension or compression.

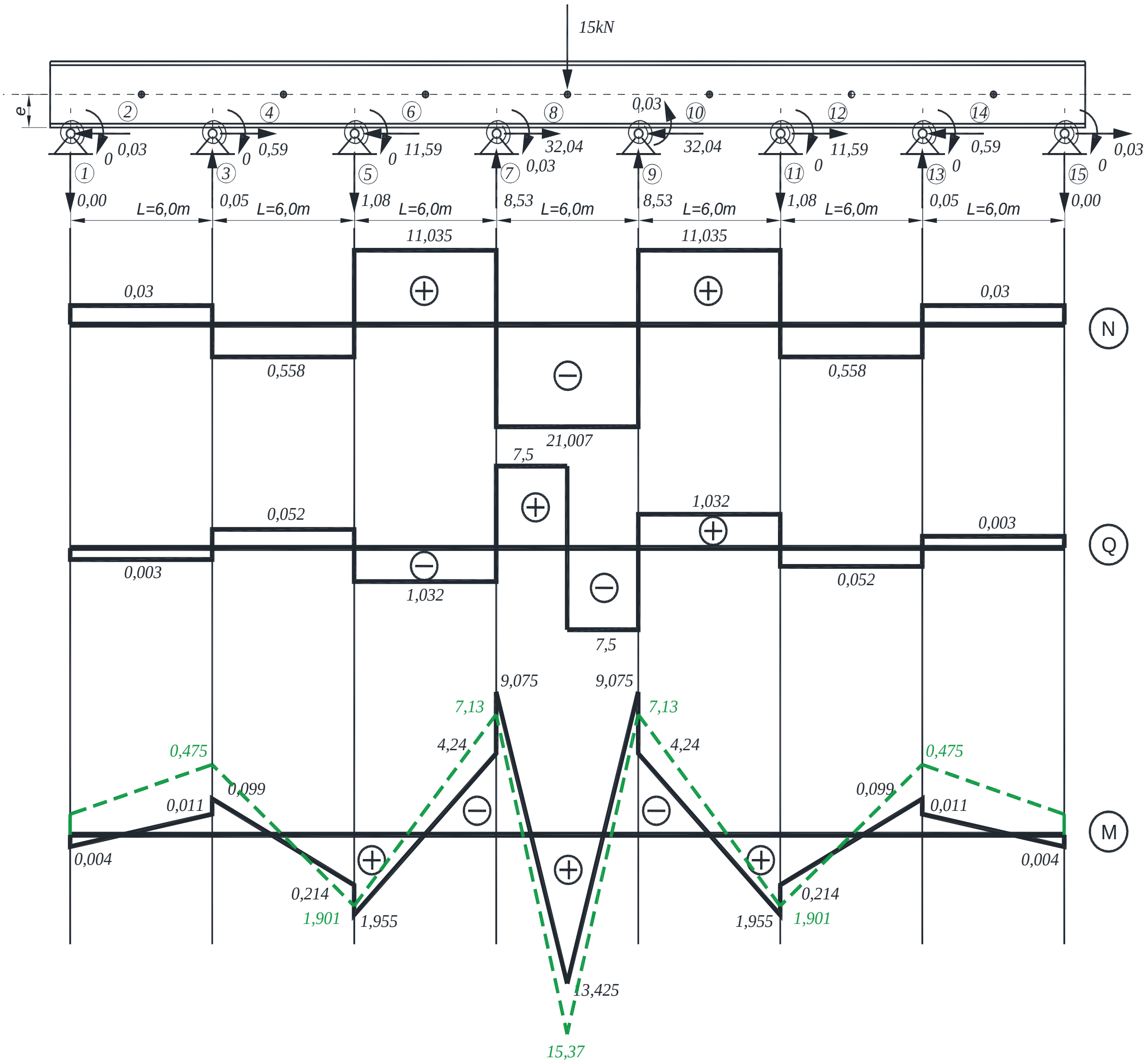

Figure 10. Numerical results for crane beam

Conclusion

The stiffness matrix for off-center connection of the finite elements is derived.

Examples of beams with off-center support and eccentrical connection are considered.

The influence on the internal forces at the different positions of the connecting joint between two elements of a continuous beam is shown.

The values of the normal forces, which many times exceed the vertical loads are demonstrated.

An example of a crane beam shows the effect of off-center supports on the stress and strain state. Large horizontal forces are observed. Bending moments over some supports and in the some span of the beam exceed those obtained when the beam is axially supported between 14,5-27%

Scientific Ethics Declaration

The author declares that the scientific ethical and legal responsibility of this article published in EPSTEM journal belongs to the author.

Notes

This article was presented as an oral presentation at the International Conference on Basic Sciences, Engineering and Technology (www.icbaset.net) conference held in Istanbul/Turkey on August 25-28, 2022.

References

Bankov, B., & Pavlova, J., (1989). Calculation of building structures using the finite element method. *Technika,* Sofia (In Bulgarian).

Bhatti, M. A., (2005). *Fundamental FE analysis and applications*, John Willey & Sons, New Jersey

Doicheva A., & Mladenov K., (2009). A problem of an off-centre supported beam with an elastic link. Third Symposium on bridges "Design and construction of bridges" UACEG - Sofia, *Civil Engineering - Bulgaria, 4*, 11-16. (In Bulgarian).

Gallagher, R. (1984). Finite element method. *Fundamentals,* Mir, Moscow (In Russian).

Gavin, H., (2011). *CE 131L. Matrix structural analysis*. Duke University, Department of Civil and Environmental Engineering.

MATLAB R2017b. The MathWorks Inc., Natick, USA.

Mladenov, K., (1985-86). Theorem of elastic analogy, annual of higher institute of architecture and civil engineering – Sofia, XXXII, 5, 76-84 (In Bulgarian).

Mladenov, K., & Doicheva, A. (2011). A study of off-center supported beams with large deflections. *"Civil Engineering" Bulgaria, No 1*, 10-22. (In Bulgarian).

Mladenov, K., Doicheva, A. & Kochev, P., (2011). Development of finite beam element for off-center transfer of forces. *Annual of the University of arhitecture, civil engineering and geodezy, XLV, VIII, Scientific Research,* 213-227. (In Bulgarian).

Saouma, V. E., (2002). *Lecture notes in finite element framed structures*. Department of Civil Environmental and Architectural Engineering, University of Colorado, Boulder.

Author Information

Albena Doicheva
University of Architecture, Civil Engineering and Geodesy (UACEG)
Bulgaria, Sofia 1164, 1 Hristo Smirnenski Blvd., Bulgaria
Contact e-mail: *doicheva_fhe@uacg.bg*

To cite this article:

Doicheva, A. (2022). Finite element method for analysis of off-center connected continuous beams. *The Eurasia Proceedings of Science, Technology, Engineering & Mathematics (EPSTEM), 18,* 37-45.

The Eurasia Proceedings of Science, Technology, Engineering & Mathematics (EPSTEM)
ISSN: 2602-3199

The Eurasia Proceedings of Science, Technology, Engineering & Mathematics (EPSTEM), 2022

Volume 18, Pages 46-54

ICBASET 2022: International Conference on Basic Sciences, Engineering and Technology

Dynamic Control of Non-Linearly Tapering FGM Beams

Khalid EL HARTI
Moulay Ismail University

Rachid SAADANI
Moulay Ismail University

Miloud RAHMOUNE
Moulay Ismail University

Abstract: This work presents the dynamics and active vibration control of a non-uniform functionally graded beam. Thanks to the strong use of beams and specifically with non-uniform section, in the different industrial applications, such as helicopter rotor blades, wind turbines, space and marine structures, we present in this article, a comparison of linearly and non-linearly tapering beams. The FGM beam is equipped with four layers of piezoelectric materials as sensors and actuators, bonded on the upper and lower surfaces of the main structure, on different finite elements to see the influence of its location on the dynamics and active control. In this study, the Timoshenko beam's theory combined with FEM is applied to a beam divided into a finite number of elements. Hamilton's principle is applied to generate the equation of motion. The structure is modeled analytically and numerically and the simulation results are presented at the end. The optimal LQG control with Kalman filtering is applied.

Keywords: Vibration, LQG-kalman control, FGM, Piezoelectric materials, Timoshenko's beam theory

Introduction

The mathematical finite element model of Euler Bernoulli has shown its limitations because it does not take into account shear effects, rotational inertia, axial displacements etc... In order to remedy this, we model our smart structure by the Timoshenko shear deformation theory. Timoshenko's beam model corrects the classical beam model by considering the effects of first order transverse shear deformation and axial displacements. Thus, the Timoshenko's beam theory overcomes the disadvantages of the EB's beam theory and the resulting mathematical model is closer to an exact model. For isotropic beams, Timoshenko's theory takes into account six fundamental global deformations (bending and transverse shearing in two directions, extension and torsion). In this model, a plane cross-section perpendicular to the beam axis before deformation no longer remains normal to the beam axis after deformation due to shear. The derivation of normality is produced by a transverse shear which is assumed to be constant over the cross section. Thus, the Timoshenko beam model performs better than the EB's model for the accurate prediction of the response of a beam and is of additional importance in the dynamics of the structure and the control of its vibrations.

In the mid-1980s, a new class of composites, called functionally graded materials (FGMs), emerged thanks to a group of Japanese scientists (Koizumi, 1997). That year, Japanese researchers faced a problem that required a specific type of composite material that could withstand a very large temperature difference in a space project. These materials exhibit a gradual change in their composition as a function of volume (Bharti et al., 2013). These composites are widely used in various engineering applications due to their high temperature resistance.

Mechanical structures are often subject to vibrations from various sources. These vibrations are generally sources of problems affecting the proper functioning of many systems and processes in different industrial sectors and many engineering fields such as automotive, aeronautics, naval... Thanks to the strong use of beams and specifically with non-uniform section, in the different industrial applications, such as helicopter rotor blades, wind turbines, space and marine structures. These systems increasingly integrate more composite materials in the manufacture of structures. The amplitude of vibrations can cause a significant number of problems such as damage or fatigue of structures. One solution to such a problem is active vibration control (AVC) (Beards 1996).

Examples of systems where AVC can be applied are numerous, such as fans, vehicle interiors, precision equipment, engines, electric and hydraulic drives, noise barriers and enclosures… (Bendine et al., 2016, El Harti et al., 2017, Panda et al., 2016). There have been extensive theoretical and experimental studies on FGM structures that have been published, especially beams and are still of interest to researchers because of their applications. (El Harti et al., 2017) studied the AVC of an FGM beam with a piezo-materials with a new geometry. They also addressed the active control of the porous Euler-Bernoulli FGM beam in a thermal environment with symmetrically bonded piezo materials (El Harti et al., 2020), as well as the dynamic analysis and AVC of the distributed piezo-thermo-elastic porous FGM beam modeled by the FEM (El Harti et al., 2021). (Sahabni & Cunedioglu, 2020) studied the free vibration analysis of cracked FG non-uniform beams. (Ebrahimi & Hashemi, 2017) investigated the vibration analysis of non-uniform FG porous beams under thermal loading. (Kumar et al., 2015) analyzed the geometrically nonlinear free vibration of axially FG taper beams. (Chen, 2021) studied the vibration analysis of axially FG Timoshenko beams with non-uniform section-cross. (Huang et al., 2013) examined the free vibration of axially functionally graded Timoshenko beam with non-uniform cross section. (Ozdemir et al., 2010) presented a study of the vibration analysis of a rotating tapered beam using DTM. (Eberle & Oberguggenberger, 2022) established a new method for estimating the bending stiffness curve of non-uniform Euler-Bernoulli beams using static deflection data.

Mathematical Formulation

A non-uniform FG beam with dimension $(L \times b(x) \times h)$, the width $b(x)$ is considered variable in this study. The general equations for the cross-sectional area, width and moment of inertia of the beam are given by (Ebrahimi & Hashemi, 2017):

$$\begin{aligned} b(x) &= b_0\left(1 - C_b \frac{x}{L}\right)^m \\ A(x) &= A_0\left(1 - C_b \frac{x}{L}\right)^m \\ I_y(x) &= b_{y0}\left(1 - C_b \frac{x}{L}\right)^m \end{aligned} \quad (1)$$

The width taper ratio (C_b) must satisfy $0 \leq C_b < 1$ for $A(x)$ and $I_y(x)$ to be positive. Knowing the width quantities at the embedding and free end of the structure, the width taper ratio can be calculated as follows:

$$C_b = 1 - \frac{b}{b_0} \quad (2)$$

In this study, the beam shrink linearly (m=1). The quantities of cross sectional area, moment of inertia at the beam embedment can be written as follows:

$$\begin{aligned} A_0 &= b_0 h \\ I_{y0} &= \frac{b_0 h^3}{12} \end{aligned} \quad (3)$$

The properties of the materials vary from pure metal on the bottom side to pure ceramic on the top side using power law, presented as follows: (El Harti et al., 2020).

$$V_c = \left(\frac{z}{h}\right)^k = 1 - V_m \quad (4)$$

According to the theory of Timoshenko, the longitudinal and transverse displacements are written, respectively (Friedman & Kosmataka, 1993):

$$u(x,y,z,t) = z\theta(x,t) \qquad w(x,y,z,t) = w(x,t) \qquad (5)$$

The nonzero components of strain can be written by (Eisenberger & Abramovich, 1997):

$$\varepsilon_{xx} = z\frac{\partial\theta}{\partial x} \qquad \gamma_{xz} = \frac{\partial w}{\partial x} + \theta \qquad (6)$$

The equations of motion are derived via the Hamilton's principle:

$$\delta\prod = \int_{t_1}^{t_2} (\delta U - \delta T - \delta W_e)\,dt = 0 \qquad (7)$$

with δU, δT , δW_e represent the variations of strain energy, kinetic energy and the work of external forces, respectively.

The strain energy U of the element can be written as:

$$U = \frac{1}{2}\int_0^l \begin{bmatrix} \frac{\partial\theta}{\partial x} \\ \frac{\partial w}{\partial x} + \theta \end{bmatrix}^T \begin{bmatrix} EI & 0 \\ 0 & KGA \end{bmatrix} \begin{bmatrix} \frac{\partial\theta}{\partial x} \\ \frac{\partial w}{\partial x} + \theta \end{bmatrix} dx \qquad (8)$$

where E, G, I and ρ are respectively, Young modulus, shear modulus, the area moment of inertia of the cross-section and the mass density, and $K = 10(1+\nu)/(12+11\nu)$ being the shear coefficient (Cowper, 1996).

The kinetic energy of the element is given as:

$$T = \frac{1}{2}\int_0^l \begin{bmatrix} \frac{\partial w}{\partial t} \\ \frac{\partial\theta}{\partial t} \end{bmatrix}^T \begin{bmatrix} \rho A & 0 \\ 0 & \rho I \end{bmatrix} \begin{bmatrix} \frac{\partial w}{\partial t} \\ \frac{\partial\theta}{\partial t} \end{bmatrix} dx \qquad (9)$$

The total work W_e due to the external forces in the beam is given by:

$$W_e = \int_0^l \begin{bmatrix} w \\ \theta \end{bmatrix}^T \begin{bmatrix} q_d \\ m \end{bmatrix} dx \qquad (10)$$

Finite Element Formulation

The equations governing the beam based on the Timoshenko theory could be satisfied if their polynomial order in w is far greater by one order of θ (Friedman & Kosmataka, 1993). Using the boundary conditions for the embedded-free beam, the transversal displacement $w(x,t)$ and its first, second spatial derivatives are given in matrix form as:

$$w(x,t)[N_w][q] \qquad \dot{w}(x,t)[N_\theta][q] \qquad \ddot{w}(x,t)[N_a][q] \qquad (11)$$

With

$$q = [w_1 \quad \theta_1 \quad w_2 \quad \theta_2]^T \qquad (12)$$

The equation of motion's element is developed by substituting the shape functions in the Hamilton principle, then integrating over the entire length of the element:

$$M\ddot{q} + Kq = \quad (13)$$

where the elementary mass matrices of the piezoelectric and FGM elements are expressed respectively as:

$$[M^{P}] = \frac{1}{2}\int_{0}^{l_p} \begin{bmatrix} N_w \\ N_\theta \end{bmatrix}^T \begin{bmatrix} \rho_p A_p & 0 \\ 0 & \rho_p I_p \end{bmatrix} \begin{bmatrix} N_w \\ N_\theta \end{bmatrix} dx \quad (14)$$

$$[M^{FGM}] = \frac{1}{2}\int_{0}^{l_b} \begin{bmatrix} N_w \\ N_\theta \end{bmatrix}^T \begin{bmatrix} C_1 & 0 \\ 0 & C_2 \end{bmatrix} \begin{bmatrix} N_w \\ N_\theta \end{bmatrix} dx \quad (15)$$

and the elementary stiffness matrices of the piezoelectric and FGM elements are also expressed respectively as:

$$[K^{P}] = \frac{1}{2}\int_{0}^{l_p} \begin{bmatrix} \frac{\partial N_\theta}{\partial x} \\ \frac{\partial N_w}{\partial x} + N_\theta \end{bmatrix}^T \begin{bmatrix} E_p I_p & 0 \\ 0 & KG_p A_p \end{bmatrix} \begin{bmatrix} \frac{\partial N_\theta}{\partial x} \\ \frac{\partial N_w}{\partial x} + N_\theta \end{bmatrix} dx \quad (16)$$

$$[K^{FGM}] = \frac{1}{2}\int_{0}^{l_b} \begin{bmatrix} \frac{\partial N_\theta}{\partial x} \\ \frac{\partial N_w}{\partial x} + N_\theta \end{bmatrix}^T \begin{bmatrix} C_3 & 0 \\ 0 & C_4 \end{bmatrix} \begin{bmatrix} \frac{\partial N_\theta}{\partial x} \\ \frac{\partial N_w}{\partial x} + N_\theta \end{bmatrix} dx \quad (17)$$

with C_1, C_2, C_3, and C_4 are constants which depend on the characteristics of the FGM material, given by (El Harti et al., 2019).

Piezoelectric Equations

The linear piezoelectric coupling between the elastic field and the electric field can be expressed by the direct and inverse piezoelectric constitutive equation (Aldraihem et al., 1997, Anjanappa & BI, 1994) as:

$$D_z = d_{31}\sigma + e^{\sigma}E \qquad D_z = d_{31}E_f + S^{c}c \quad (18)$$

The voltage will be applied as an input to the actuator with an accurate gain depending on the degree of damping desired.

$$V^{c}(t) = G_c e_{31} z b \int_{0}^{l_p} n_1^T \dot{q}\, dx \quad (19)$$

where $z = \left(\frac{h}{2} + t_s\right)$, and e_{31} being the piezoelectric stress/load constant.

$$V_1^{c}(t) = S_c[0 \quad -1 \quad 0 \quad 1] \quad (20)$$

$$V_2^{c}(t) = -S_c[0 \quad -1 \quad 0 \quad 1 \quad (21)$$

where $S_s = G_C e_{31} z_1 b$ is called the sensor constant.

Dynamic Equation

The dynamic equation of the structure and the control equation are finally given by:

$$M^*\ddot{g} + C^*\dot{g} + K^*g = f^*_{ext} + f^*_{ctr1} + f^*_{ctr2} \quad (22)$$

The state space model in MIMO mode is given by:

$$\dot{x} = Ax(t) + Bu(t) + Er(t) \quad (23)$$

$$y(t) = C^T x(t) + Du(t) \quad (24)$$

Results and Discussion

In the aim to validate the control's procedure, we consider an embedded-free FGM beam with a non-uniform section, partially covered by four layers of piezoelectric materials. A pulse of amplitude (1N) is applied as external force. The figures below show the response of the beam to the pulse. In all results, we presents the comparison of the responses, with and without control, varying the location of piezoelectric actuators as well as the taper ratio, and the power index. The geometrical and physical characteristics of the materials are shown in (Table 1).

Table 1. Geometric and physical characteristics of the structure

Physical properties	FG material	Material (PZT) Sensor/Actuator
Length (m)	$L = 5 \times l_b = 0.$	$l_p = 0.05$
Width (m)	$b = 0.03$ $b_0 = 0.02$	$b = 0.03$ $b_0 = 0.02$
Thickness (m)	$h = 0.002$	$t_s = t_a = 0.00001$
Density (Kg/m^3)	$\rho_m = 2780$ $\rho_c = 3800$	$\rho_p = 7700$
Young's Modulus (G Pa)	$E_m = 70$ $E_c = 380$	$E_p = 68.1$
Poisson's ratio	$\nu_m = 0.3$ $\nu_c = 0.3$	$\nu_p = 0.3$
PZT Strain constants (m/V)		$d_{31} = 125 \times 10^{-12}$
PZT Stress constant (Vm/N)		$g_{31} = 10.5 \times 10^{-3}$

Figure 1 shows the variation of the width from b=3 to b=2, keeping the power index k=1. Figure 2 presents the variation of the power index for k=(0.5; 1; 5) and b=2. in the first two figures, the actuator pair is in the FE2. Figure 3 shows the variation of the actuator pair between FE2 and FE3 for k=1 and b=2.

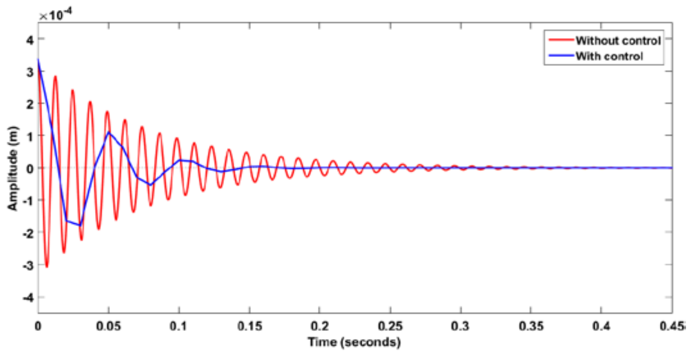

(a) b=3

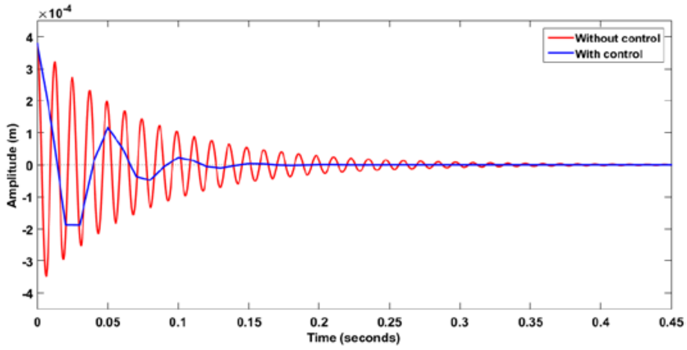

(b) b=2.5

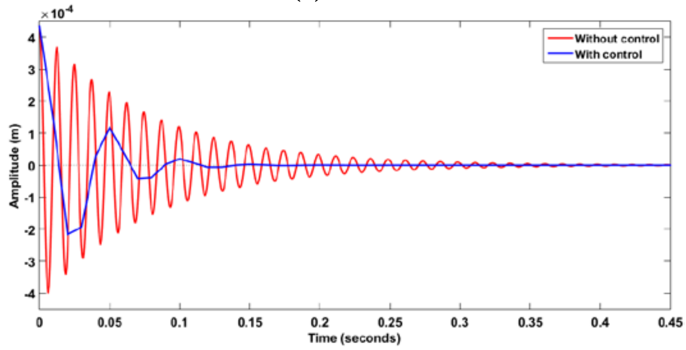

(c) b=2

Figure 1. Impulse response of the smart beam for k=1 (Actuators in FE2)

From (figure 1), we find that the increase in the width taper ratio (decrease in the width) between b=3 and b=2, implies increases in the amplitudes of the vibrations. The decrease in width implies a decrease in the mass matrix, it means that the structure becomes less resistive.

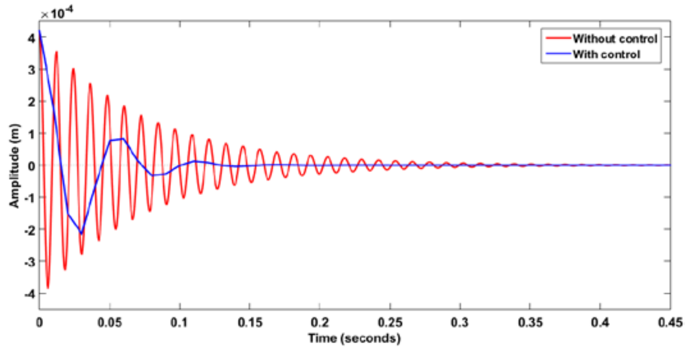

(a) k=0.5

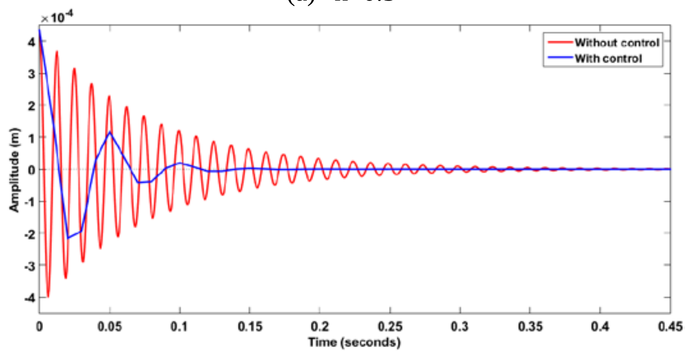

(b) k=1

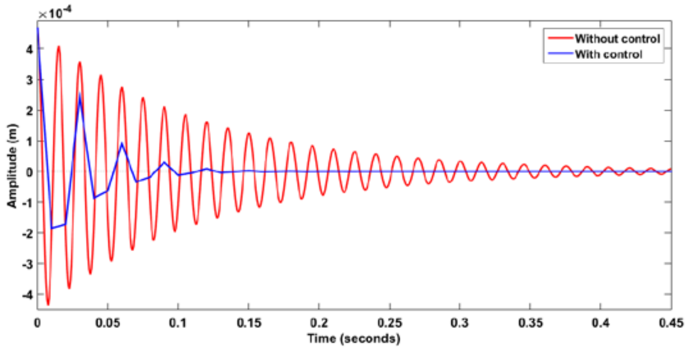

(c) k=5

Figure 2. Impulse response of the smart beam for b=2 (Actuators in FE2)

Figure 2 shows the variation of the power index. From the figure, we find that the increase in the power index between k=0.5 and k=5, implies an increase in the vibration amplitudes. This increase is due to the fact that the increase in the power index, the beam contains more metal than ceramic, the thing which explains the weakness of the matrix of matrix and rigidity.

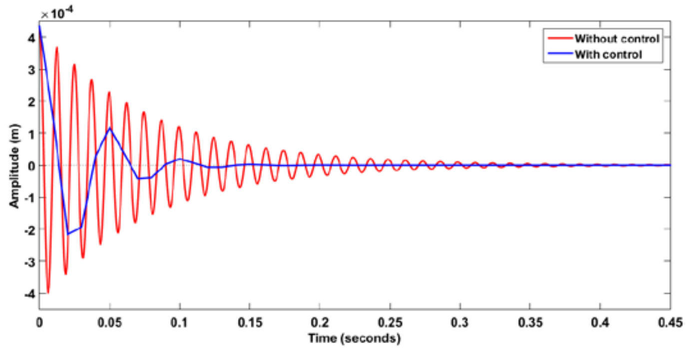

(a) FE2

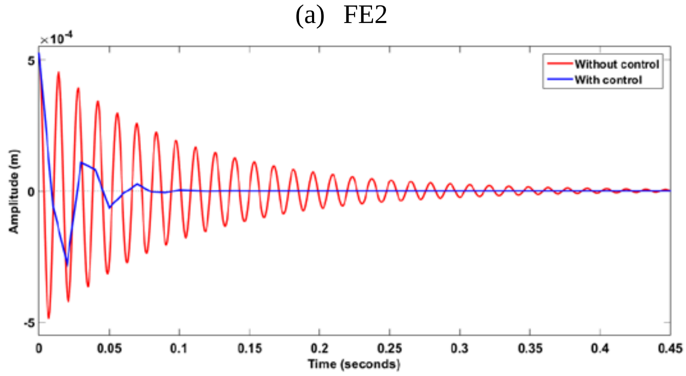

(b) FE3

Figure 3. Impulse response of the smart beam for k=1 and b=2

From Figure 3, the displacement of the actuator pair from the embedded end to the free end implies an increase in the vibration amplitudes. This increase is explained, that the displacement of a quantity of material towards the free end is equivalent to an increase in the excitation force.

Conclusion

In order to study the dynamics and active control of a non-uniform section FGM beam, based on Timoshenko theory and FEM, we consider a free-embedded FGM beam containing four layers of piezoelectric materials. The analysis of results shows that the increase in the power index, the increase in the width taper ratio as well as the displacement of the pair of actuators towards the free end, imply increases in the amplitudes of the vibrations. also the comparison of the responses in open and closed loop shows the success of the LQG-Kalman active control procedure.

Scientific Ethics Declaration

The authors declare that the scientific ethical and legal responsibility of this article published in EPSTEM journal belongs to the authors.

Acknowledgements or Notes

This article was presented as an oral presentation at the International Conference on Basic Sciences, Engineering and Technology (www.icbaset.net) conference held in Istanbul/Turkey on August 25-28, 2022.

References

Aldraihem, O. J., Wetherhold, R. C., & Singh, T. (1997). Distributed control of laminated beams: Timoshenko theory vs. Euler-Bernoulli theory. *Journal of Intelligent Material Systems and Structures, 8*(2), 149-157.

Anjanappa, M., & Bi, J. (1994). Magnetostrictive mini actuators for smart structure applications. *Smart Materials and Structures*, *3*(4), 383.

Beards, C. E. (1996). *Structural vibration: analysis and damping*, 1st ed. Arnold: London, UK.

Bendine, K., Boukhoulda, F. B., Nouari, M., & Satla, Z. (2016). Active vibration control of functionally graded beams with piezoelectric layers based on higher order shear deformation theory. *Earthquake Engineering and Engineering Vibration*, *15*(4), 611-620.

Bharti, I., Gupta, N., & Gupta, K. M. (2013). Novel applications of functionally graded nano, optoelectronic and thermoelectric materials. *International Journal of Materials, Mechanics and Manufacturing, 1*(3), 221-224.

Chen, W. R. (2021). Vibration analysis of axially functionally graded Timoshenko beams with non-uniform cross-section. *Latin American Journal of Solids and Structures*, 18.

Cowper, G. R. (1996). The shear coefficient in Timoshenko's beam theory. *ASME J. App. Mech.*, *33*, 335-340.

Eberle, R. & Oberguggenberger, M. (2022). A new method for estimating the bending stiffness curve of non-uniform Euler-Bernoulli beams using static deflection data. *Applied Mathematical Modelling*, *105*, 514-533.

Ebrahimi, F. & Hashemi, M. (2017). Vibration analysis of non-uniform imperfect functionally graded beams with porosities in thermal environment. *Journal of Mechanics*, *33*(6):739-757.

Eisenberger, M. & Abramovich, H. (1997). Shape control of non-symmetric piezolaminated composite beams. *Computers and Structures*, *38*, 565-571.

El Harti, K., Sanbi, M., Rahmoune, M., Saadani, R., Agounoun, R., Bentaleb, M., & Rahmoune, M. (2017). Active vibration control of sandwich FGM beam with piezoelectric sensor/actuator. *Int. J. Appl. Eng. Res*, *12*(20), 9338-9345.

El Harti, K., Rahmoune, M., Sanbi, M., Saadani, R., Bentaleb, M., & Rahmoune, M. (2019, February). Finite element model of vibration control for an exponential functionally graded Timoshenko beam with distributed piezoelectric sensor/actuator. *Actuators Vol. 8*, No. 1, p. 19.

El Harti, K., Rahmoune, M., Sanbi, M., Saadani, R., Bentaleb, M., & Rahmoune, M. (2020). Dynamic control of Euler Bernoulli FG porous beam under thermal loading with bonded piezoelectric materials. *Ferroelectrics*, *558*(1), 104-116.

El Harti, K., Sanbi, M., Saadani, R., Bentaleb, M., & Rahmoune, M. (2021). Dynamic analysis and active control of distributed piezothemoelastic FGM composite beam with porosities modeled by the finite element method. *Composites: Mechanics, Computations, Applications: An International Journal*, *12*.1.

Friedman, Z. & Kosmataka, J. B. (1993). An improved two-node Timoshenko beam finite element. *Computers and Structures*, *47* (3), 473-481.

Huang, Y., Yang, L. E., & Luo, Q. Z. (2013). Free vibration of axially functionally graded Timoshenko beams with non-uniform cross-section. *Composites Part B: Engineering*, *4*5(1), 1493-1498.

Koizumi, M. (1997). FGM activities in Japan. *Compos. Part B Eng*.,*28*,1–4.

Kumar, S., Mitra, A. & Roy, H. (2015). Geometrically nonlinear free vibration analysis of axially functionally graded taper beams. *Engineering Science and Technology. An International Journal*, *18*(4), 579-593.

Ozdemir Ozgumus, O. & Kaya, M. O. (2010). Vibration analysis of a rotating tapered Timoshenko beam using DTM. *Meccanica*, *45*(1), 33-42.

Panda, R. K., Nayak, B., & Sarangi, S. K. (2016). Active vibration control of smart functionally graded beams. *Procedia Engineering*, *144*, 551-559.

Shabani, S. & Cunedioglu, Y. (2020). Free vibration analysis of cracked functionally graded non-uniform beams. *Materials Research Express, 7*(1):015707.

Author Information

Khalid El Harti
Laboratory of Advanced Materials Studies and Applications,
Fs-Est, Moulay Ismail University,
Meknes, Morocco.
Contact e-mail:*elhartikhalid@gmail.com*

Rachid Saadani
Laboratory of Advanced Materials Studies and Applications,
Fs-Est, Moulay Ismail University,
Meknes, Morocco

Miloud Rahmoune
Laboratory of Advanced Materials Studies and Applications,
Fs-Est, Moulay Ismail University,
Meknes, Morocco

To cite this article:

El Harti, K., Saadani, R. & Rahmoune, M. (2022). Dynamic control of non-linearly tapering fgm beams. *The Eurasia Proceedings of Science, Technology, Engineering & Mathematics (EPSTEM), 18,* 46-54.

The Eurasia Proceedings of Science, Technology, Engineering & Mathematics (EPSTEM), 2022

Volume 18, Pages 55-63

ICBASET 2022: International Conference on Basic Sciences, Engineering and Technology

Moisture Absorption Behavior of CP5 Composite Materials Used in Industry

Băilă DIANA-IRINEL
University Politehnica of Bucharest

Păcurar RĂZVAN
Technical University of Cluj-Napoca

Păcurar ANCUȚA
Technical University of Cluj-Napoca

Abstract: In engineering practice, perhaps the most interesting aspect of woodworking deals with the relationship between wood and moisture. The plywood composite presents hygroscopicity characteristic, as the wood and reaction almost like a sponge, will gain or lose moisture from the air based upon the conditions of the surrounding environment. When the tree is in the green state, is first felled, it contains a very large amount of moisture existing in two different forms: as free water that is contained as liquid in the pores or vessels of the wood itself and as bound water, trapped within the cell walls. After that the wood is exposed to the air and immediately loose free water and the wood does not contract or otherwise change in dimension, it is in the state of drying and it is called the fiber saturation point. The moisture content in each piece of CP5 composite material is expressed as a percentage of the weight of the water and oven-dry weight of CP5 composite material. The moisture absorption depends on the wood type, density of wood and it is influenced by the environmental temperature, this is an aspect very important in the furniture industry. The moisture absorption test is generally used for quality control purposes and to measure the degradation of the quality for the wood and composite materials.

Keywords: Isotherm absorption, Composite materials, Rate of moisture, SEM analysis, Thermostat enclosure

Introduction

Variation of the moisture content can cause wood to shrink and swell and alter its dimensions, affecting all wood properties. In the same time, the manufacturing, gluing, and finishing of wood and its mechanical, thermal, and acoustic properties are influenced by moisture content, this can increase weight 100 percent or more, with great effects on transportation costs. For realizing traction tests for the CP5 composite samples on the temperature and hydroscopic control, it was used an enclosure thermostat controlled in temperature and humidity.

The humidity can influence too, the processing operations, especially drying, preservative treatment, and pulping. The moisture content of CP5 composite material can be calculated based on its current and oven-dry weight. In the case of wood, the hygroscopic value varies between 30 to 100 percent, in function of species, position of the wood in the tree or year seasons. In this article we used a climate room with control system and an electric moisture meter portable that can measure the change of electrical properties of CP5 composite material, in function of changing moisture content. In the case of carbon-fiber-reinforced polymer matrix composites, the high specific strength, stiffness, and good chemical resistance, make them attractive for applications in aerospace components, sporting goods, civil structures, and marine vehicles, but humidity absorption can reduce their mechanical properties (Costa, 2006). For the basalt fibre reinforced polymer matrix composites, the moisture absorption influences considerable the mechanical properties (Pandian, 2014). By example for carica papaya fiber reinforced polymeric composites, the moisture absorption affects the thickness swelling behaviors on mechanical performances (Saravanakumaar, 2022).

Fiber-reinforced polymer composites may offer numerous attractive features such as low cost, high specific performance, and ease of production. But their durability and sustained performance depend of severe and changing environmental conditions. Property drop was observed to be much more significant for the samples that were exposed to lower freezing temperatures before moisture absorption (Hamidi, 2017). For the natural fiber composites was investigated the value of Fickian diffusivity constant, moisture equilibrium content and correction factor. Tests were carried out on composite plates, which was a combination of sugar palm fiber and epoxy resins and two different fiber compositions have been chosen which were 10% and 20% by weight and it is shown that, for composite plates that contain higher fiber composition, the moisture absorption rate is even higher (Leman, 2008).

Method

For establish the moisture value for the CP5 composite samples in function of the temperature and hydroscopic control, it was used an enclosure thermostat controlled in temperature and humidity. The thermostat enclosure is composed of the following elements:

- the inner tube of welded stainless steel sealed and exhaust bung;
- mineral wool insulation;

Two joints in silicon;

Door opener with wedge-thermal bridges: The principle of heating enclosure it is realized using the caloric resistances in stainless steel, arranged behind a table screen. The cooling is accomplished by a fluid evaporation condenser in a shifter in the form of copper tube. Concerning the adjusting the temperature, the cooling it is regulated using a tuning electro valve, been equipped with a cold circuit. The heating it is made using under voltage heating resistances with a static relay. For controlled humidity it is used a solenoid feed, a cold drying racket, electro valves that inject compressed and dried air.

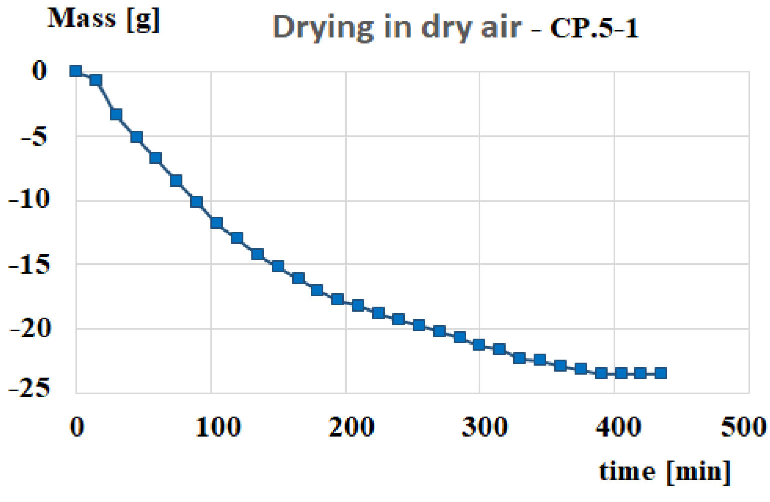

Figure1.Drying in dry air for C.P.5-1 composite material

Results and Discussion

In this research, it was studied the moisture behavior for traction tests for the CP5 composite material. For CP5 composite material is shown the experimental values of absorption coefficients for moisture 1%H, at the temperature of 100^{o}C in the Table 1.

Table 1. Moisture coefficients for CP5 composite material at 1%H and the temperature of 100^{o}C

Temperature [oC]	Time [min]	Humidity [H]	Mass [g]
25.4	0	1	0
79.8	15	1	-0.7
102.3	30	1	-3.3
102.3	45	1	-5.1
102.4	60	1	-6.8
102.4	75	1	-8.5
102.4	90	1	-10.1
102.5	105	1	-11.8
102.6	120	1	-13
102.4	135	1	-14.2
102.6	150	1	-15.2
102.7	165	1	-16.1
102.6	180	1	-17
102.4	195	1	-17.8
102.6	210	1	-18.2
102.6	225	1	-18.8
102.6	240	1	-19.3
102.4	255	1	-19.7
102.4	270	1	-20.2
102.5	285	1	-20.7
102.6	300	1	-21.3
102.6	315	1	-21.6
102.6	330	1	-22.3
102.6	345	1	-22.5
102.4	360	1	-22.9
102.4	375	1	-23.2
102.6	390	1	-23.5
102.6	405	1	-23.5
102.4	420	1	-23.5
102.6	435	1	-23.5

In the Table 2 is presented the variation of the experimental mass values in function of time for the CP5 composite material for temperature of 20^{o}C and different moisture values and in the table 3 are presented the mass value in function of time at the temperature of 40^{o}C and different moisture values (20%H, 40%H, 60%H, 80%H). In the figure 2 is shown the curve of variation between the mass values and time for the temperature of 20^{o}C and different wettability coefficients (20%H, 40%H, 60%H, 80% H) and in the figure 3 it is represented the variation curve in the same conditions, but for the temperature of 40^{o}C.

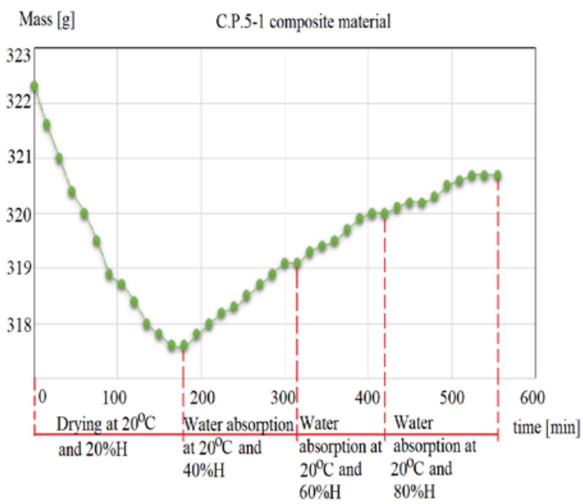

Figure 2. Curve of variation between the mass values and time for the temperature of 20°C and different moisture levels (20%H, 40%H, 60%H, 80% H).

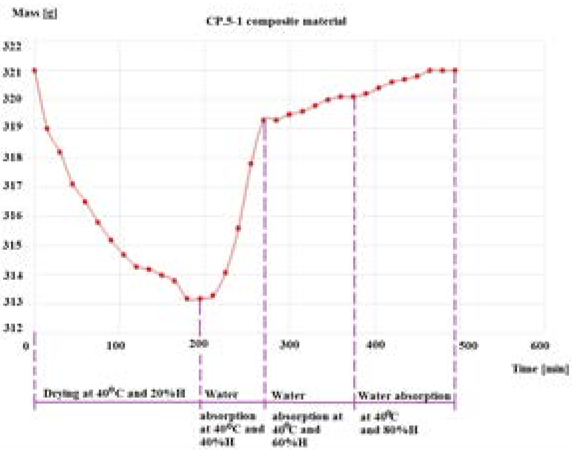

Figure 3. Curve of variation between the mass values and time for the temperature of 40°C and different moisture levels (20%H, 40%H, 60%H, 80%H)

Table 2. Mass variation in time for CP5 composite material at different moisture coefficients (20%H,40%H, 60%H, 80%H) and the temperature of 20°C

Temperature [oC]	Time [min]	Humidity [H]	Mass [g]
19.8	0	20	323.3
19.8	15	20	322.6
19.9	30	20	322
19.9	45	20	321.4
19.9	60	20	321
19.8	75	20	320.5
20	90	20	319.9
19.9	105	20	319.7
19.9	120	20	319.4
20.1	135	20	319
20.1	150	20	318.8
20	165	20	318.6
20	180	20	318.6
20	195	40	318.8
19.9	210	40	319
19.9	225	40	319.2
19.8	240	40	319.3
19.8	255	40	319.5
20	270	40	319.7
20	285	40	319.9
20	300	40	320.1
20	315	40	320.1
19.9	330	40	320.3
20.1	345	60	320.4
20.1	360	60	320.5
20	375	60	320.7
20	390	60	320.9
20	405	60	321
20.1	420	60	321
20.1	435	80	321.1
20.1	450	80	321.2
19.9	465	80	321.2
19.9	480	80	321.3
19.9	495	80	321.5
20	510	80	321.5
20	525	80	321.7
20	540	80	321.7
20	555	80	321.7

Table 3. Mass variation in time for CP5 composite material at different moisture coefficients (20%H, 40%H, 60%H, 80%H) and the temperature of 40°C

Temperature [°C]	Time [min]	Humidity [H]	Mass [g]
39.8	0	20	301.8
39.7	15	20	302.6
39.9	30	20	304.2
39.8	45	20	306.2
39.9	60	20	309.8
40	75	20	311.8
39.8	90	20	312.3
39.7	105	20	314
40	120	20	315.7
39.9	135	20	316.8
39.8	150	20	317.2
40	165	20	317.6
39.9	180	20	318.2
40	195	20	318.2
40	210	40	318.3
40.1	225	40	318.8
39.8	240	40	319.2
39.9	255	40	319.4
39.9	270	40	319.3
40	285	60	319.3
40.1	300	60	319.5
40.1	315	60	319.6
39.9	330	60	319.8
39.9	345	60	320
40	360	60	320.1
40.1	375	60	320.1
40	390	80	320.2
40	405	80	320.4
40	420	80	320.6
40.1	435	80	320.7
40.1	450	80	320.8
40	465	80	321
40	480	80	321
40.1	495	80	321

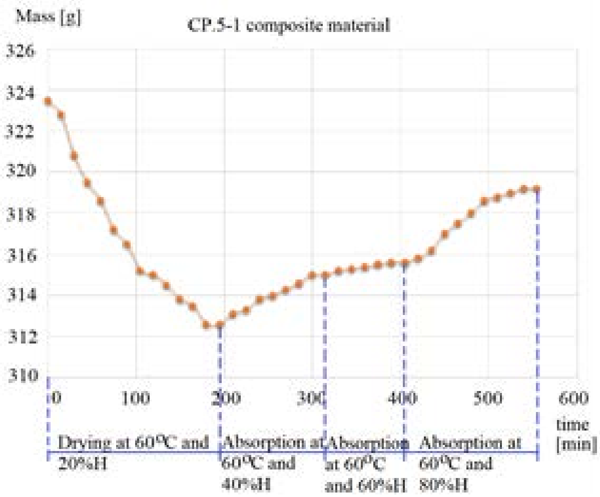

Figure.4. Curve of variation between the mass values and time for the temperature of 60°C and different moisture levels (20%H, 40%H, 60%H, 80% H).

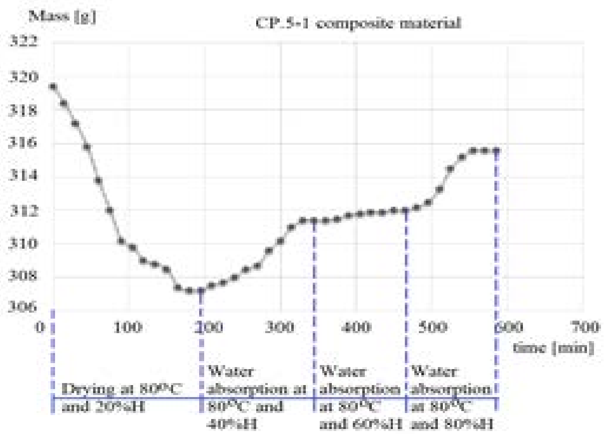

Figure 5. Curve of variation between the mass values and time for the temperature of 80°C and different moisture levels (20%H, 40%H, 60%H, 80%H)

Table 4. Mass variation in time for CP5 composite material at different moisture coefficients (20%H,40%H, 60%H, 80%H) and the temperature of 60oC

Temperature [°C]	Time [min]	Humidity [H]	Mass [g]
59.8	0	20	323.5
60	15	20	322.8
59.9	30	20	320.8
59.9	45	20	319.5
59.8	60	20	318.6
59.8	75	20	317.2
59.9	90	20	316.5
59.9	105	20	315.2
59.9	120	20	315
60.1	135	20	314.5
60	150	20	313.8
60.1	165	20	313.5
59.9	180	20	312.6
59.8	195	20	312.6
59.9	210	40	313.1
60	225	40	313.3
60	240	40	313.8
59.8	255	40	314
60	270	40	314.3
59.9	285	40	314.6
60	300	40	315
60.1	315	40	315
59.9	330	60	315.2
60	345	60	315.3
60	360	60	315.4
59.8	375	60	315.5
59.8	390	60	315.6
59.9	405	60	315.6
60.1	420	60	315.8
60.1	435	80	316.2
60.1	450	80	317
59.9	465	80	317.5
59.9	480	80	318
60	495	80	318.6
59.8	510	80	318.8
60	525	80	319
60	540	80	319.2
60	555	80	319.2

Table 5. Mass variation in time for CP5 composite material at different moisture coefficients (20%H, 40%H, 60%H, 80%H) and the temperature of 80°C

Temperature [°C]	Time [min]	Humidity [H]	Mass [g]
79.7	0	20	319.4
79.7	15	20	318.4
79.6	30	20	317.2
79.6	45	20	315.8
79.6	60	20	313.8
79.7	75	20	312
79.7	90	20	310.2
79.6	105	20	309.8
79.8	120	20	309
79.8	135	20	308.8
79.7	150	20	308.5
79.7	165	20	307.4
79.8	180	20	307.2
79.8	195	20	307.2
79.7	210	40	307.5
79.8	225	40	307.7
79.8	240	40	308
79.8	255	40	308.5
79.6	270	40	308.7
79.7	285	40	309.6
79.7	300	40	310.2
79.8	315	40	311
79.8	330	40	311.4
79.8	345	40	311.4
79.9	360	60	311.4
79.9	375	60	311.5
79.9	390	60	311.7
79.8	405	60	311.8
79.8	420	60	311.9
79.7	435	80	311.9
79.7	450	80	312
79.9	465	80	312
79.8	480	80	312.2
79.9	495	80	312.5
79.7	510	80	313.3
79.8	525	80	314.5
79.8	540	80	315.2
79.8	555	80	315.6
79.8	570	80	315.6
79.7	585	80	315.6

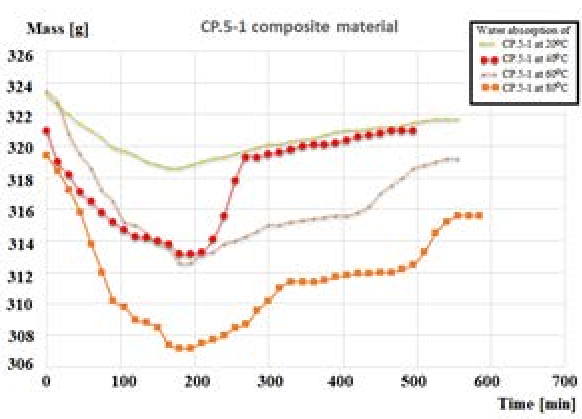

Figure 6. Curves of the variation of the mass during the time in function of different temperatures

Figure 7. SEM analyses plywood CP5 composite

In the Table 4 is establish the variation of the mass values during on time for the CP5 composite material for temperature of 60^{o}C and different moisture values and in the table 5 is shown the mass value variation in function of time at the temperature of 80^{o}C using different moisture values (20%H, 40%H, 60%H, 80%H). In the figure 4 is presented the curve of variation between the mass values and time for the temperature of 60^{o}C and different wettability coefficients (20%H, 40%H, 60%H, 80% H) and in the figure 5 it is shown the variation curve in the same conditions, for the temperature of 80^{o}C. In the figure 6 can remarck the different curves that show the variation of the mass during the time for the CP5 composite material. In figure 7 is presented the microscopic structure of CP5 composite material.

Conclusion

Due to the urge of developing environmentally friendly materials, researches in new dimensions evolved .This new dimension focuses on developing eco friendly material with good mechanical strength. The CP5 composite materials presents a higher moisture resistance in comparisons with different other composites. At the humidity value of 20%H, can remarck a drying process for the composite materials, if it increases the humidity values, can remarck an increase of mass values proportional with the humidity percents, because of the water absorption in the composite materials, although the temperature rises. Its superior properties will certainly help Composite engineers, researchers, manufacturers in developing environment friendly materials for a better tomorrow in future and could substitue the synthetic plastic and non degradable plastic.

Scientific Ethics Declaration

The authors declare that the scientific ethical and legal responsibility of this article published in EPSTEM journal belongs to the authors.

Acknowledgement

This article was presented as an oral presentation at the International Conference on Basic Sciences, Engineering and Technology (www.icbaset.net) conference held in Istanbul/Turkey on August 25-28, 2022.

This work has been funded by the EEA & Norway Grant, with project title “European network for 3D printing of biomimetic mechatronic systems”, Acronym EMERALD - Nr. Contract 21-COP-0019/ F-SEE-026/06.2021.

References

Amuthakkannan, P., Vairavan, M., Thangaiah, W. & Uthayakumar, M. (2014). Effect of moisture absorption behavior on mechanical properties of basalt fibre reinforced polymer matrix composites, *Journal of Composites*, Article ID 587980.

Costa, M., Rezende, M.C. & Almeida, S. (2006). Effect of void content on the moisture absorption in polymeric composites, *Polymer-Plastics Technology and Engineering 45*(6),691-698.

Hamidi, Y., Aktas, L. & Altan, M. (2017). Thermal history effects on moisture absorption of fiber-reinforced polymer composites, *AIP Conference Proceedings 1914*, 030012.

Leman, Z., Sapuan, S.M., Saifol, A.M., Maleque, M.A. & Ahmad, M. (2008), Moisture absorption behavior of sugar palm fiber reinforced epoxy composites, *Materials&Design 29*(8), 1666-1670.

Saravanakumaar, A., Senthilkumar, A., Rajan, B., Rajini, N., Ismail, S., Mohammad, F. & Al-Lohedan, H. (2022). Effects of moisture absorption and thickness swelling behaviors on mechanical performances of carica papaya fiber reinforced polymeric composites, *Journal of Natural Fibers*, https://doi.org/10.1080/15440478.2022.2051668.

Author Information

Băilă Diana-Irinel
University Politehnica of Bucharest, Romania
Blv.Splaiul Independenței, no.313, sector 6, cod 060042, Bucharest, Romania
Contact e-mail: *baila_d@yahoo.com*

Păcurar Răzvan
Technical University of Cluj-Napoca, Romania
Faculty of Machine Building, Department of Manufacturing Engineering, Blv. Muncii, no. 103-105, 400641, Cluj-Napoca, Romania

Păcurar Ancuța
Technical University of Cluj-Napoca, Romania
Faculty of Machine Building, Department of Manufacturing Engineering, Blv. Muncii, no. 103-105, 400641, Cluj-Napoca, Romania

To cite this article:

Diana-Irinel, B., Răzvan, P. & Ancuța, P. (2022). Moisture absorption of CP5 composite materials used in industry. *The Eurasia Proceedings of Science, Technology, Engineering & Mathematics (EPSTEM), 18*, 55-63.

The Eurasia Proceedings of Science, Technology, Engineering & Mathematics (EPSTEM)
ISSN: 2602-3199

The Eurasia Proceedings of Science, Technology, Engineering & Mathematics (EPSTEM), 2022

Volume 18, Pages 64-71

ICBASET 2022: International Conference on Basic Sciences, Engineering and Technology

Smart Cities: Using GIS Technology in Urban Infrastructure Development at Migration Areas

Bushra ZALLOOM
Zarqa University

Abstract: Technology played a vital role in urban planning and urban infrastructure development. The Geographic Information System (GIS) can help in creating smart cities by analyzing the required issues and present them for local communities. It can improve utilization of existing infrastructure capacity thus improving quality of life, it can also provide a guidance about mobility and the best use for available services. Smart cities promise that with increasing connectedness, services and quality of life can be improved. The intent of smart cities is to make urbanization more inclusive, bringing together public and private sectors, connecting urban centers with periphery, delivering services for all users alike, and integrating the migrants and poor into their community. This research aim at highlighting the advantages of using GIS technology in urban infrastructure development at Migration Areas in Amman the capital of Jordan that welcomes waves of immigration during the last decades which affect its infrastructure, basic services, and socio-economic situation. It focuses on one of the neighborhood and discover the challenges and opportunities based on the infrastructure development analyses using the GIS. The findings of this research confirm the essential need for smart cities with more inclusive plan to help in decreasing the vulnerability of both refugees and host communities thus enhance the social sustainability.

Keywords: Smart Cities, Urban Infrastructure, GIS, Migration Areas, Amman

Introduction

Smart city is the city of tomorrow. It tries to identify a smarter option to maximize the individuals satisfaction and accelerate urban socio-cultural and economic development (Cathelat, 2019). The smart city information system is built on four principles: Planning and engineering, data-driven performance, operational efficiency, and civic inclusion. However, According to Cathelat (2019:41) “the current reality of smart cities is that there aren’t any. At the end of the day, most so-called smart cities are just cities with a few or several standout smart projects”. Still, there are many initiatives in Jordan for a Smart city that are initiated to achieve one or more of the following objectives:

1. Efficiency of Services: Make the best effective use of public resources, and provide a high level of citizen service.
2. Sustainability: Develop the city with considering the environmental, economic and social impacts.
3. Mobility: Make it easy for all users to move in the city, whether by foot, bike, car, public transport.
4. Safety and Security: Improve public safety and security in every-day life, as well as being best possibly prepared for emergencies and disasters.
5. Economic Growth: Attract businesses, investors, citizens and visitors.
6. City Reputation: Constantly improve the city’s image and reputation.

These objectives can be achieved by using various types of technology such as GIS, online forums, online survey, and digital media throughout the decision-making process, these tools connect cities at the national and international levels and foster knowledge exchange among various parties, it also increases the public awareness among stakeholders for the importance of good data management and urban observatory platforms for future.

Since its development in the 1970s, the GIS is used in planning and developing the urban infrastructure, it becomes easier to analyze the collected data and bring many proposals to the ground (Banerjee, 2020). Today, a growing number of cities rely on GIS to model the real world at every stage of planning and development of a Smart City as it can incorporate a huge number of variables. There are various applications of GIS that help in developing the urban infrastructure in a smart way by analyzing the required issues and present them for individuals (Consortium, 2019). It can improve utilization of existing infrastructure thus improving quality of life, it can also provide the best practices for various types of mobility. In urban infrastructure projects the GIS is used based on a number of steps (Consortium, 2019):

1. Creation of the Urban Digital Model that illustrates the components of the urban built and natural environments.
2. Creation of the Sensing Layer that comprises sensors used for monitoring urban networks and infrastructures.
3. Analysis of Data by converting real-time and historical data into operational data that improves the security, efficiency and quality of urban systems.
4. Interactive Visualization of urban components and sensors maps. Users can utilize these maps to access static and dynamic data concerning urban systems.
5. The Control Layer that allows real-time visualization of these devices as well as their status. It could also visualize errors in device command.

Accordingly, this paper provide context on the national refugee situation in Jordan. Then, it highlights how Jordan can transform the migration challenges into spatial and urban infrastructure investment and create smart communities by using the GIS technology throughout planning stages. the GIS technology is used in studying the current condition of urban infrastructure at one of the migrants' areas in Amman, called the Al Hashmi Al Janoubi neighborhood, to help in developing this area in a smart way. Finally, this paper summarizes the urban challenges and opportunities that can be addressed through future development strategies.

Method

The research methodology consists of data collection, literature revision, and field observation. Stakeholders were asked to identify existing challenges in current infrastructure. These were categorized under the four main topics: Natural Environment, Urban Environment, Infrastructure Projects, and Refugee Integration. Moreover, Geographic Information System (GIS) is used to undertake the spatial analysis throughout the proposed plans, and assess the accessibility to public facilities.

National Context: Refugees in Jordan

Since its independence in 1946, Jordan has been a safe paradise to approximately 4 million refugees including Circassian, Palestinians, Iraqis, Syrians, and Yemeni, and others. Today, Jordan is hosting 89 refugees per 1,000 inhabitants (UNHCR, 2018). These refugees have become an important part of the country’s population and social fabric. The extraordinary numbers of refugees from surrounding countries have significantly affected Jordan throughout its history, and played a vital role in shaping the country’s politics, economy, community, and urban characteristics (Zalloom, 2020).

Figure (1) illustrates the refugee population density based on the nationality, indicating the highest refugee presence for Palestinians, Syrians, and Iraqis at the Amman city (UN-Habitat, 2022). This analysis supported the selection of the neighborhood that has been affected by the refugee influx.

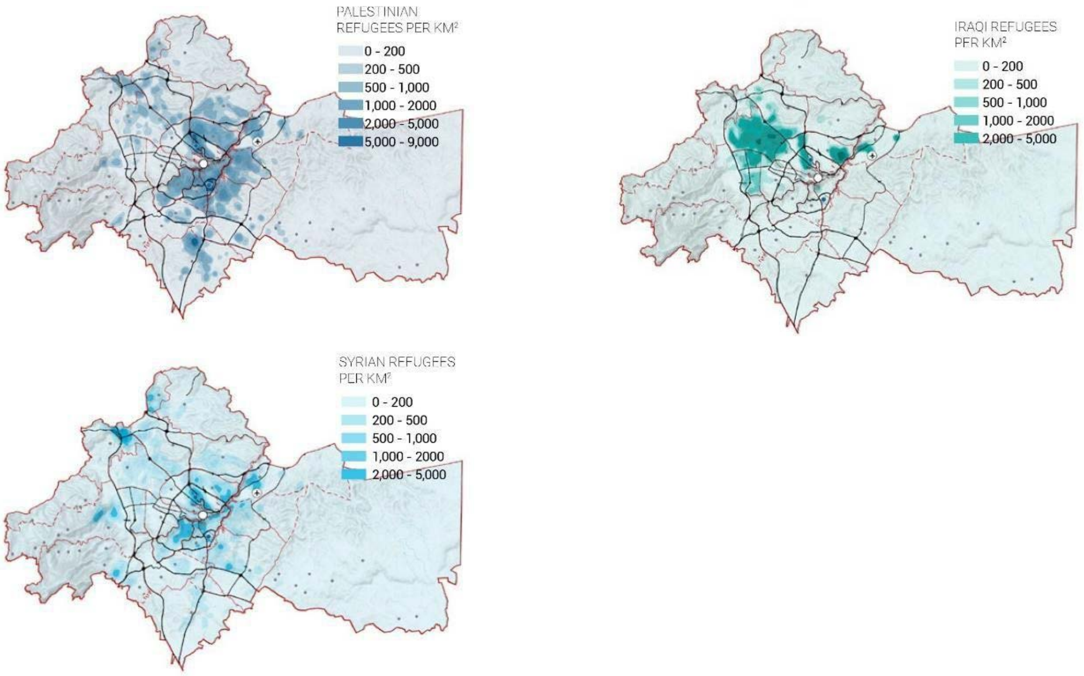

Figure 1. Refugee population density in Amman city (Source: UN-Habitat 2022)

After ten years of the Syrian Crisis and their immigration to Jordan, it becomes clear that the infrastructure, basic services, and economies of Jordanian cities are affected. The need for a more inclusive plan that help in decreasing the vulnerability of both refugees and host communities and provide longer-term sustainable solutions is appeared (Government of Jordan, 2020). Accordingly, national and international efforts are made to cope with this urban transformation, and to improve access to services and socioeconomic opportunities for displaced and host communities.

Applying GIS Technology in a Migrants' Area in Amman

Since 2011, municipal services in Amman, the capital of Jordan, have been significantly affected by the Syrian refugee crises. The waves of refugees from camps to urban areas has a major impact on the capacity of infrastructure and public facilities, such as education, health, public space, transportation, and natural resources (United Nations Jordan, 2021). The rapid displacement of populations to urban settings had major spatial, economic, environmental, and social impacts, which maximize the challenges that facing Amman Municipality such as, the lack of access to acceptable basic service infrastructure, the lack of affordable housing. These challenges affecting the refugees as well as the host communities. The urban sprawl and inefficient urban planning have led to the insufficient distribution and access to services and infrastructure which may cause critical issues. This negatively impacts their economic and social sustainability, thus, has resulted in the inefficient use of valuable resource and has left communities facing increased long-term problems, a lack of self-reliance, and insufficient access to urban services. Therefore, studying and analyzing the areas where migrants come and live is very essential.

The collection of accurate data helps in planning and decision-making process, thus, allows for achieving sustainable urban development. Developing and implementing efficient and reliable plans requires accurate, comprehensive, and up-to-date data to understand the urban needs of the population. However, inaccurate data lead to spatial inequalities in service supplying, housing, education, and public space development. Unfortunately, the available data at municipalities only considers local citizens, rather than all inhabitants, including the refugees, this may result in inadequate resource provisioning and inequitable services' distribution.

Using the modern technology such as GIS helps in filling these gaps when collecting and analyzing data, and help in creating guidance for the current and future planning of the city, which should be aligned to the Sustainable Development Strategy. It is an analytic tool that spatially integrates and analyzes urban indicators and attributes at the city levels by creating multi layers (Banerjee 2020, Zalloom 2020). Furthermore, applying the Sustainable Development Goals (SDGs) is essential as it helps in supporting the selected neighborhood to become more inclusive, safe, resilient, and sustainable. Urban planning strategies that built on infrastructure investments aim to benefit migrant communities, enhance the quality of their life, and create better opportunities for economic investment (UN-Habitat, 2022). In this manner, public can participate in decision making process and they involve in all planning stages from the beginning.

Accordingly, a spatial plan is developed for Al Hashmi Al Janoubi neighborhood in Amman. The area of study is one of the most affected areas with influx of refugees, it has an area of 0.43 km2, a total population of 14,100 inhabitants, therefore, a population density is 32,118.4 person/ km2 (UN-Habitat, 2022). Figure (2) shows the land use of the compacted neighborhood, the satellite image was combined with the available data by using the GIS technology. The created figure shows the residential land use within the neighborhood that mainly comprises of types C, type D, and the unplanned zones while the area has no assigned commercial land uses within its boundaries, instead, small commercial shops that are usually on the ground floor of mixed-use buildings are used to serve residents.

The residential types “C” and “D” according to the “Law of Planning of Cities, Villages, and Buildings, No.79” can have up to four floors, with minimum setbacks of 2.5 meters at “D” type and 3 meters at “C”type. This distance allow people to contact daily, thus, have a strong relationship that enhance the social sustainability of the area. Furthermore, the project is underpinned site visits to visually assess the current situation and to interact with the residents in the neighborhood, the field observation for the neighborhood found housing in good condition and structure, but still the existing public infrastructure, the walkways, and street furniture are not acceptable and need maintenance.

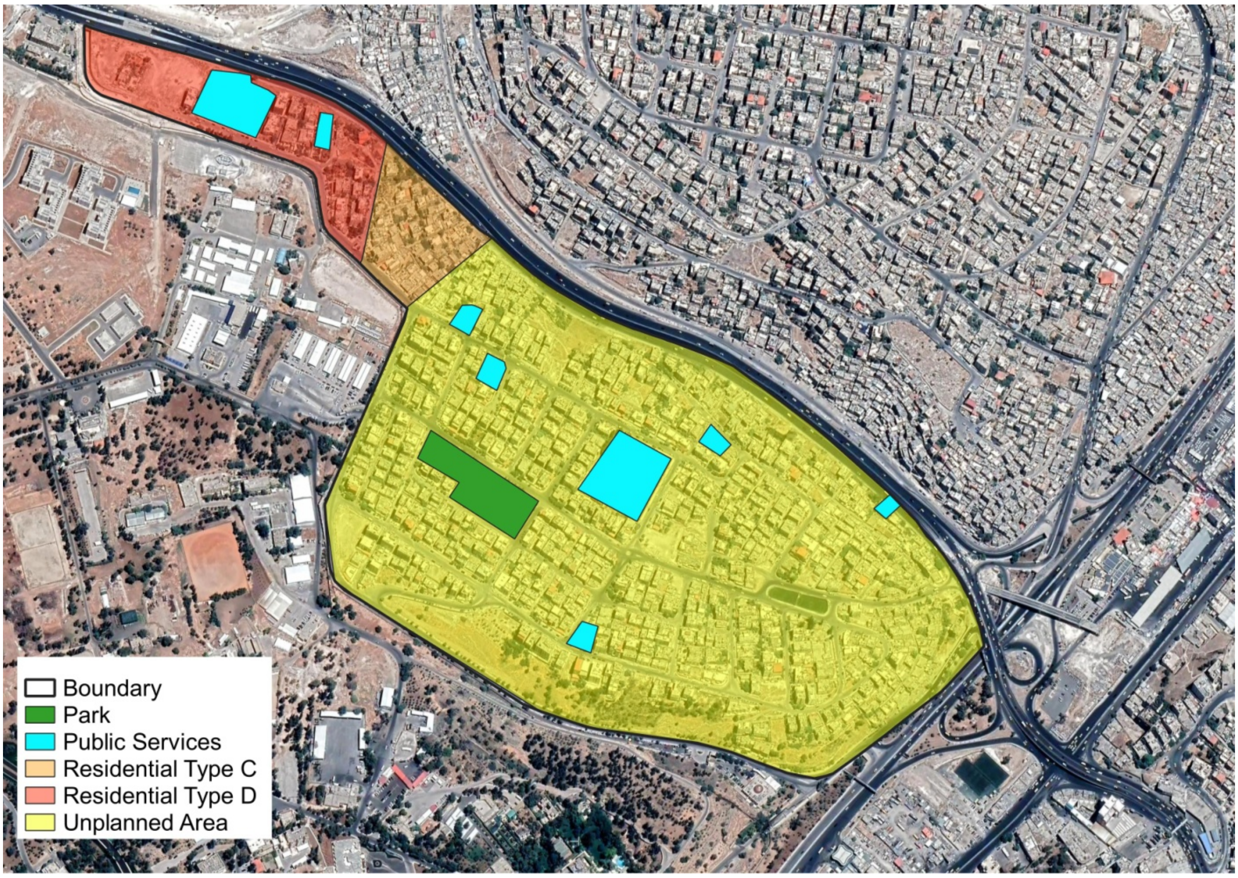

Figure 2. Satellite image shows the compacted neighborhood

Al Hashmi Al Janoubi neighborhood is further analyzed by the GIS program based on its context, refugee presence, access to transportation, access to basic services, and access to public facilities. It was used to undertake the spatial analysis throughout the proposed plans, and assess the accessibility to public facilities within a walkable distance of 15 to 30-minute. The site analysis shows that there are three schools for male and females, four mosques, one public park, and one public health center (Figure 3). The accessibility to these services is very high. Moreover, the street network analysis shows that all services located within a walkable distance, 40.9% of the population have access to these services within a 5-minute walking distance and 100% within a 15-minute (Figure 4). The preparation of urban planning analyses for the selected area will help in proposing various planning scenarios and arranging priorities that improve living conditions thus enhancing the quality of life; these priorities can be identified, discussed, and converted to actions. It gives a comprehensive spatial understanding of the existing situation as a basis for decision-making. This provides a unique opportunity for stakeholders with different mandates to work together to connect short-term plans with long-term strategies and investments, enabling the development of more inclusive communities.

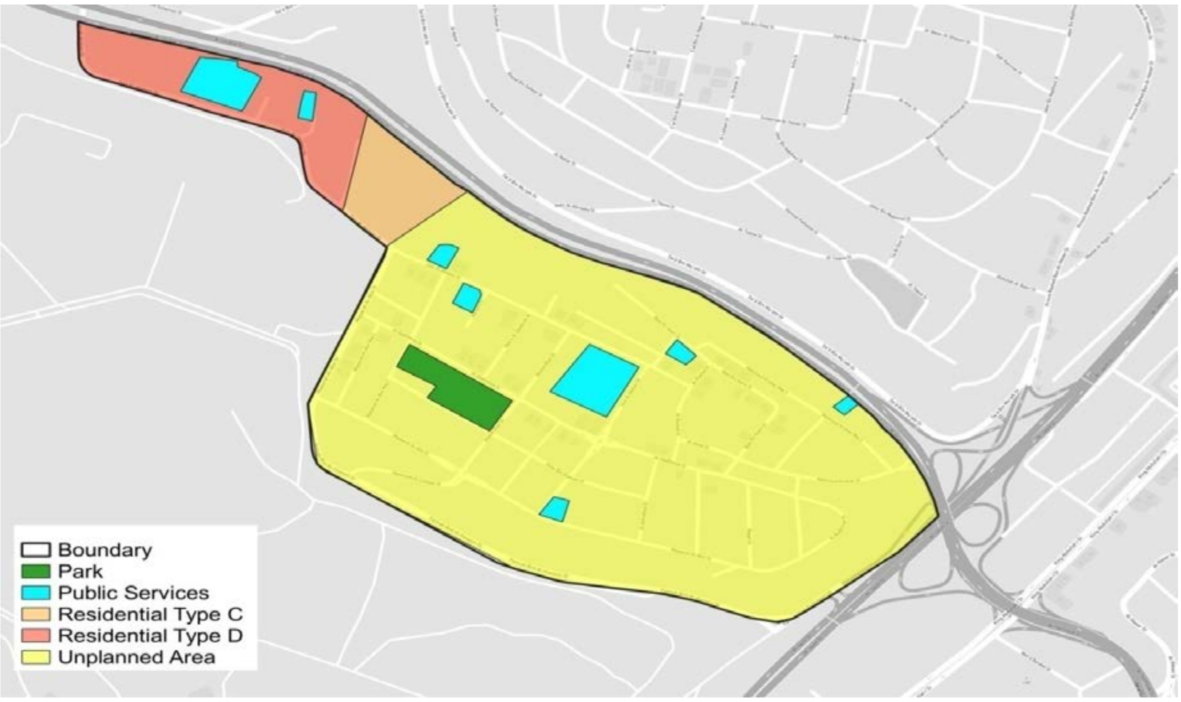

Figure 3. Land use map

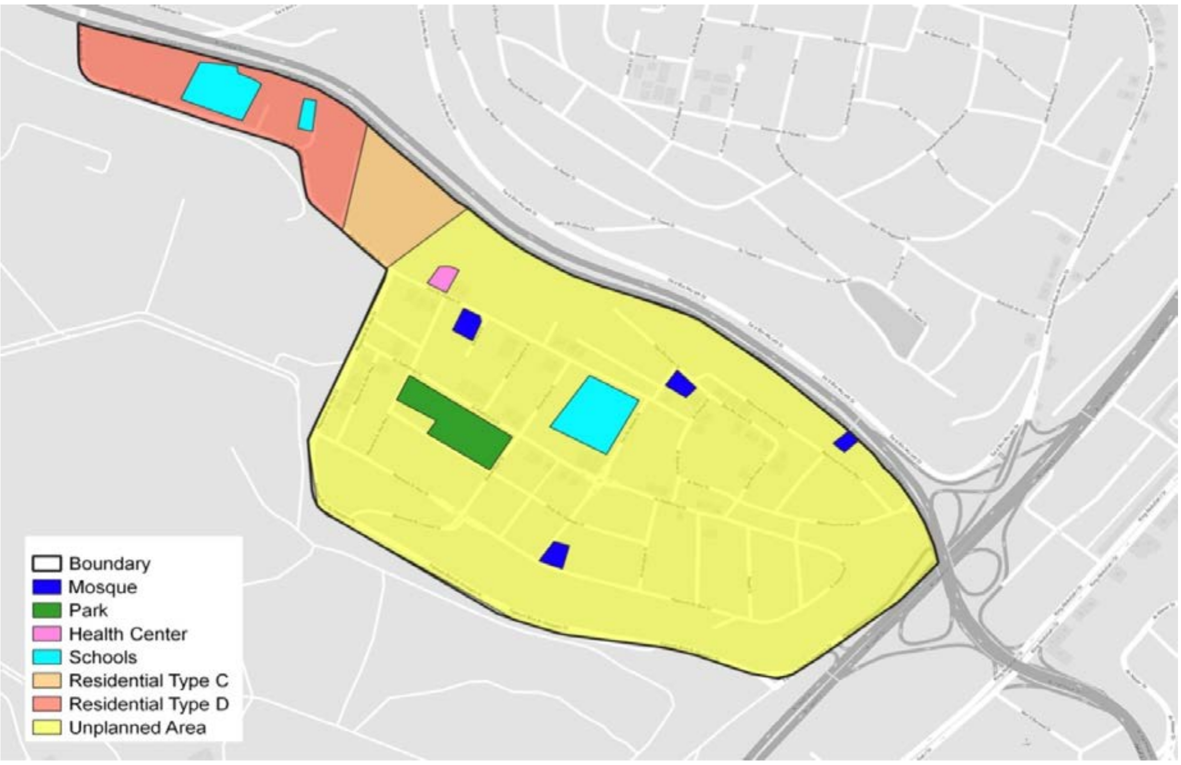

Figure 4. Access to public services

Findings: Challenges and Opportunities

The spatial planning of Amman has revealed various strategic challenges accompanied with the waves of migrations at various levels. At the national level, the major challenge identified is unequal urbanization, whereby weak urban planning practices and influxes of refugees have led to inadequate distribution and access to basic services and public facilities. Accordingly, this rapid urban growth has resulted in urban sprawl that increased the demand on services, thus maximize the pressure on Greater Amman Municipality, who have limited resources to fulfill this gap. This has impacted the quality-of-service, as well as the quality of life for locals and immigrants. Moreover, the lack of affordable adequate housing has become a critical issue due to the inflated prices of land, construction, and energy. Furthermore, inadequate transportation has resulted in major environmental, economic, and social challenges, as public transportation is slow, costly, and time consuming, thus, mainly used by the refugees and locals with low incomes. Refugees and host communities are currently facing outstanding challenges caused by the COVID-19 pandemic, which has resulted in increasing unemployment rates. The Municipality has limited capacity to support local economic development, while also facing constraints to finance service delivery.

At the neighborhood level, it was discovered that Al Hashmi Al Janoubi neighborhood in Amman lack access to health care facilities as it has only one public health center, although it is located within a walkable distance but still not enough to fulfill the residents' and migrants' needs. The neighborhood also has some challenges concerning road maintenance, whereby there is a need for speed bumps, pedestrian crossings, pedestrian bridges on the main roads, safe walkways, street-lighting and furniture.

The neighborhood has no assigned commercial land uses within its boundaries, instead, small commercial shops that are usually on the ground floor of mixed-use buildings are used to serve residents. It is clear that the outdated "Law of Planning of Cities, Villages, and Buildings, No.79", which was established in 1966 affected the land use, the facility distribution, as well as the urban fabric. Furthermore, the area lack of children facilities and it is not designed for people with disabilities, besides the lack of maintenance and rehabilitation of the existing public recreational facilities, and a lack of green elements and spaces. There are also some concerns about the safety of the park at nights as it becomes a men domain and cannot be used by women and children.

Although these challenges specifically affect the achievement of the SDGs goals, but still, there is a significant opportunity to address the challenges associated with migration. At the national level, the Syrian refugee crisis can be transformed into a development opportunity that attracts new investments and boosts the local economy. Amman has a high proportion of youth where more than half of the population are under 25 years old (The Department of Statistics, 2020). This means that there is a growing labor force, less demand on health facilities, and reduced dependency rates. Moreover, the COVID-19 pandemic and restrictions raised awareness on the importance of spatial planning, the availability of green open space, of investing the vacant lands for green open spaces, urban agriculture to reduce unemployment, mitigate climate change impact, enhance the residents' socio-economic conditions, and achieve food security. Likewise, developing adequate mobility options will give the opportunity of minimizing the environmental impact and increasing the residents' socioeconomic conditions and access to job opportunities. The strategic location of Amman, and the enhancement of affordable and accessible public transport is an important opportunity that can enhance the socioeconomic opportunities. As there are several planned infrastructure projects and investments that will help in promoting sustainability and improving the delivery of services.

At the neighborhood level, the study confirms that there is an opportunity to improve access to healthcare through constructing a comprehensive health centre and upgrading the existing primary health centre within the neighborhood. The mobility of residents could be enhanced through restoring the road infrastructure, adding various means of street furniture such as lighting poles, waste containers and benches, extending a public transport route into the neighborhoods, as well as adding pedestrian bridges. There are also opportunities to encourage diversity in commercial facilities by establishing community centre training centre, and by improving the public spaces, which can host various social activities, bazaars, cafes and restaurants, thus boost the livability of the public areas.

Conclusion

Technology played a fundamental role in urban infrastructure development. The Geographic Information System (GIS) is used to provide a better understanding of the urban context at different levels, it helps in creating smart cities by analyzing the collected data and transform them into maps. The analyses outcomes are then presented for local communities and stakeholders. This research aim at highlighting the advantages of Using GIS Technology in urban infrastructure development at Migration Areas in Amman the capital of Jordan.

The waves of emigration have played a vital role in shaping the country's politics, economy, and urban characteristics. A specific neighborhood in Amman is selected as an example to understand the impacts of these migrations based on the infrastructure development analyses using the GIS. The findings of this research confirm the essential need for smart cities with more inclusive plan to help in decreasing the vulnerability of both refugees and host communities thus enhance the social sustainability.

Recommendations

It is recomended that the findings of this research considered as a foundation for decision- making when developing the urban infrastructure at the migration areas. The challenges and opportunities identified in this spatial planning for the selected neighborhood can be entry points for future national and international strategies.

Scientific Ethics Declaration

The author declares that the scientific ethical and legal responsibility of this article published in EPSTEM journal belongs to the author.

Acknowledgements

This article was presented as an oral presentation at the International Conference on Basic Sciences, Engineering and Technology (www.icbaset.net) conference held in Istanbul/Turkey on August 25-28, 2022.

The author acknowledge the Dean of Scientific Research at Zarqa University in Jordan for funding this research. Special thanks to Eng. Mais Malik Atiyat for preparing the GIS maps.

References

Banerjee, S., Chakraborty, C., & Das, D. (2020). An approach towards GIS application in smart city urban planning. In *Internet of Things and Secure Smart Environments* (pp. 71-110). Chapman and Hall/CRC.

Cathelat, B. (2019). *Smartcities shaping the society of 2030.* Paris: UNESCO and NETEXPLO. Aralık, 21, 2021.

Consortium (2019). *What is the use of application of GIS services in smart cities?* July 7, 2022. https://giscindia.com/use-application-gis-services-smart-cities/

Government of Jordan. (2020*). Jordan response plan for the Syria crisis 2020-2022*. Retrieved April 21, 2022, from Ministry of Planning and International Cooperation

The Department of Statistics. (2020). *Estimated population of 2020 and some of selected data*. Retrieved April 21, 2022, The Department of Statistics: http://dosweb.dos.gov.jo/DataBank/ Population_Estimares/PopulationEstimates

UNHCR. (2018, February). *UNHCR Jordan factsheet* - February 2018. Retrieved April 21, 2022, from ReliefWeb: https://reliefweb.int/report/jordan/unhcr-jordan-factsheet-february-2018

UN-Habitat (2022, March). *AMMAN SPATIAL PROFILE*. Retrieved from United Nations Jordan: https://jordan.un.org/sites/default/files/2022-04/220411-final_amman_profile_0.pdf

United Nations Jordan (2021, July 04). *Together we learn: supporting inclusive education for refugees in Jordan*. Retrieved from United Nations Jordan: https://jordan.un.org/en/134455-together-we-learn-supporting-inclusive-education- refugees-jord

Zalloom, B. (2020). Enhancing tourism by reconnecting the fragmented landscape of wadi araba in Jordan. *Journal of Urban Planning and Development. 146*(3): 05020010. https://doi.org/10.1061/(ASCE)UP.1943-5444.0000592

Author Information

Bushra Zalloom
Zarqa University
Zarqa, Jordan
Contact e-mail: *bzalloom@zu.edu.jo*

To cite this article:

Zalloom, B. (2022). Smart cities: Using GIS technology in urban ınfrastructure development at migration areas. *The Eurasia Proceedings of Science, Technology, Engineering & Mathematics (EPSTEM), 18,* 64-71.

The Eurasia Proceedings of Science, Technology, Engineering & Mathematics (EPSTEM)
ISSN: 2602-3199

The Eurasia Proceedings of Science, Technology, Engineering & Mathematics (EPSTEM), 2022

Volume 18, Pages 72-80

ICBASET 2022: International Conference on Basic Sciences, Engineering and Technology

The Preparation of Montmorillonite/Carrageenan-Composite Hydrogel for Chromium (VI) Removal from Aqueous Solution

Gulen Oytun AKALIN
Aksaray University

Abstract: In this study, Montmorillonite/Carrageenan (MMT/CG)-composite hydrogel was synthesized for removal of Chromium (VI) from aqueous solution. The chemical structure, morphological property and thermal decomposition of (MMT/CG)-composite hydrogel has been evaluated by Fourier Transform Infrared Spectroscopy (FTIR), Scanning Electron Microscope Spectroscopy (SEM) and thermogravimetric analysis (TGA), respectively. The X-ray data of (MMT/CG)-composite hydrogel was researched crystallite properties. The results of (MMT/CG)-composite hydrogel CG, and MMT powders had compared each other to research the efficiency of MMT. The efficiency of adsorption parameters (contact time, initial feed concentration, and pH) on Chromium (VI) ion adsorbing capacity of (MMT/CG)-composite hydrogel was also investigated by UV–vis diffusive reflectance spectra. The adsorption capacity enhanced with the adding of MMT in hydrogel. The adsorption process was determined by the Langmuir isotherm model. According to the findings, the MMT/CG-composite hydrogel can be utilized as a suitable adsorbent to removal of Chromium (VI) from aqueous solution.

Keywords: Montmorillonite, Carrageenan, Hydrogel, Adsorption, chromium (VI)

Introduction

Water pollution is increasing day by day following the rapid industrial improvement. Industrial wastes, pesticides, detergents, agricultural fertilizers, dyestuffs, and heavy metals are major pollutions. Heavy metals must be effectively removed from water sources due to their toxic and carcinogenic properties.

Ion exchange, chemical precipitation, chemical oxidation/reduction, reverse osmosis, and ultrafiltration methods are frequently used to remove heavy metal ions. However, these methods have low efficiency and high cost, and they cause significant waste problem. Adsorption is another alternative method (Islam, Angove, & Morton, 2019). It is the accumulation of a substance on the surface of the second phase by passing from one phase to the other, or the retention of adsorbent molecules dissolved in the liquid phase on a solid adsorbent surface or the adhesion phenomenon that occurs at the phase interface because of the concentration change at the boundary surface. It occurs between solid-liquid or solid-gas phases. It has advantages such as low cost, simplicity of design, low energy requirement, high efficiency, ease of use, and reuse of adsorbents. The adsorption method becomes more prominent when environmentally friendly, non-toxic, cheap, and safe adsorbents are used. (Dakiky et al., 2002). In recent years, there has been a lot of research for alternative low-cost materials that are effective and biodegradable, such as hydrogels, agricultural wastes, and clays.

Hydrogels are inexpensive polymeric materials which include hydrophilic groups (such as -COOH, $-SO_3H$, -OH, $-NH_2$, -CONH, $-CONH_2$, etc.). They can easily swell in water due to their hydrophilic groups. They are extremely used in heavy metal removal systems because of their high-water holding capacity, biocompatibility, and biodegradability (Ahmed, 2015). Several natural polymers such as gelatin, carboxymethyl cellulose, pectin, chitosan, alginate, carrageenan etc. are utilized for formation of hydrogels.

Carrageenan is obtained from *Rhodophyceae class* seaweed by some extraction methods from red algae species. It is a linear polysaccharide produced from the most common red algae *Chondrus Crispus* and *Gigartina Mamillosa*. It consists of large and highly elastic molecules in a coiled helical structure. Its flexible structures enable to generate gel forms at room temperature. (Sharma et al., 2022). Thanks to these properties, it is used as a thickener and stabilizer in the food industry and other industrial fields.

Clays are good adsorbent for heavy metal ions, polymer nanocomposites, catalyst, photochemical reactions, and biosensors. They have high chemical and mechanical stabilities and several surface and structure properties. Montmorillonite (MMT) is the commonly preferred clay for industrial utilization. MMT is an alteration forming of volcanic tuff and ash, product of bentonite beds, and of wall rock and pegmatite dikes bordering hydrothermal mineral deposits. It is non-toxic and low-cost, but its adsorption capability is limited by its poor water permeability. To overcome this limitation, MMT can be blended with other materials such as CMC, PVA, PMMA etc. to generate composite hydrogels (Ianchis et al., 2020; Kaşgöz, & Durmus, 2008). These composites have high water permeability, and they are used as adsorbents for heavy metal removal. However, the use of MMT/Carrageenan-composite hydrogels as adsorbent for heavy metal removal has not been studied. In this research, MMT/Carrageenan-composite hydrogels were prepared for *Cr(VI)* ions removal. The adsorption capacity of *Cr(VI)* ions by changing the MMT/CG mass ratio, pH of *Cr(VI)* solution, initial *Cr(VI)* concentration and contact time were investigated. To describe the adsorption character, adsorption isotherm model was examined.

Materials and Methods

Sodium-MMT with a zeta potential of -39.3 mV and a cationic exchange capacity of 71 mequiv/100 g was purchased from Southern Clay (USA) was supplied by Ciba Specialty Chemicals (Thailand). CG and Glutaraldehyde were supplied by Sigma Aldrich.

Preparation of MMT/Carrageenan-Composite Hydrogels

The MMT/CG suspensions were prepared by adding MMT (0.1, 0.2 and 0.3 w/v) to the 1% (w/v) CG solution under vigorous dispersion for 1 hr. 100 ml of MMT/CG suspension was added dropwise to 0.2% (w/v) glutaraldehyde solution using a peristaltic pump for the MMT/CG ratios of 0.1:1, 0.2:1 and 0.3:1 respectively. After the stirring for 1 h, the solidified MMT/CG-composite hydrogels were obtained, they washed with distilled water several times and then dried at 60°C for 24 h.

Characterization of MMT/CG Hydrogels

The MMT, Carrageenan and MMT/Carrageenan composite hydrogels were performed by Fourier transform infrared (FTIR) spectrophotometry (FT-IR Shimadzu IR-Prestige 2) using KBr. The measurement was scanned between 400 and 4000 cm^{-1}. The crystallinity of the samples was performed by wide-angle X-ray diffraction (XRD; Diffractometer Bruker D8 Advance). The X-ray diffractometer was done at 40 kV and 50 mA, with Cu-Kα radiation source (λ=1.54060 Å). The morphology of the composite hydrogels was visualized by scanning electron microscopy (SEM; model Quanta 250, FEI). Thermal analysis of the composite hydrogels were determined by thermogravimetric analysis (TGA; TG/DTA 7300 Hitachi) under nitrogen gas flow from 30°C to 800°C at a heating rate of 10°C/min.

Adsorption Studies

The influence of contact time, pH, and initial concentration of *Cr(VI)* solution on adsorption was investigated. The adsorption was performed on a shaker (120 rpm) at 25^{o}C using 0.2 g MMT/CG composite hydrogels (MMT/CG mass ratio 0.1:1.0 and 0.3:1.0), and 50 mL of Cr (VI) solution (80 mg/L) in a 125-mL conical flask. The *Cr(VI)* solution was collected at certain time intervals and the residual *Cr(V*I) concentration was measured using a UV-vis spectrophotometer (Shimadzu-18A UV-Visible spectrophotometer) at 540 nm (Alemayehu, Singh, & Tessema, 2012).

The amount of adsorbed *Cr(VI)* concentration at time *t* was determined from Equation 1:

$$Qt = \frac{(Co - Ct)\,V}{W} \tag{1}$$

Qt is amount of adsorbed *Cr(VI)* per amount of hydrogel at time t (mg/g), C_0 is initial *Cr(VI)* concentration (mg/L), C_t is *Cr(VI)* concentration at time t (*mg/L*), *W* is weight of dried composite hydrogels (*g*) and *V* is volume of *Cr(VI)* solution (L).

The equilibrium adsorption capacity (Q_e) of the composite hydrogels was determined from Equation 2:

$$Qe = \frac{(Co - Ce)\,V}{W} \tag{2}$$

where C_0 and C_e are initial concentration and equilibrium concentration of *Cr(VI)* in solution (*mg/L*) respectively, *V* is volume of *Cr(VI)* solution (*L*) and *W* is weight of dried composite hydrogels (*g*).

Results and Discussion

FTIR

The FTIR spectra of the MMT powder, CG powder and MMT/CG hydrogel (with MMT/CG mass ratio of 0.3:1 as representative sample) are given in Figure 1. The characteristic peaks of CG at 1291 cm^{-1} (the O = S = O stretching vibration of C-4 position of galactose), 929 cm^{-1} (C-O-C vibration mode of the 3,6-anhydro-D-galactose residue) and 844 cm^{-1} (the $–O\text{-}SO_3$ stretching vibration of C-4 position of galactose) are occurred in the MMT/CG composite hydrogel (Pereira et.al, 2003). The hydrogel and CG powder both had a broad absorption peak at 3500-3000 cm^{-1}, representing the -OH stretching mode. The absorption at 2920 cm^{-1} was observed due to C–O groups and the interlayer C–H stretching. The absorption at 1500 cm^{-1} was represented for the $–CH_2$ stretching. The absorption at 1080 cm^{-1} for glycosidic linkage, the absorption at 933 cm^{-1} for C–O of 3,6-anhydro-D-galactose and the absorption at 850 cm^{-1} for $C–O–SO_3$ of D-galactose-4-sulfate were obtained. The functional groups of Al-O and Si-O of MMT in the MMT/CG-composite hydrogel were occurred between 400 and 600 cm^{-1}, which was absent in the CG powder. (Hayati-Ashtiani, 2011). This can be proved by the formation of MMT/CG hydrogel.

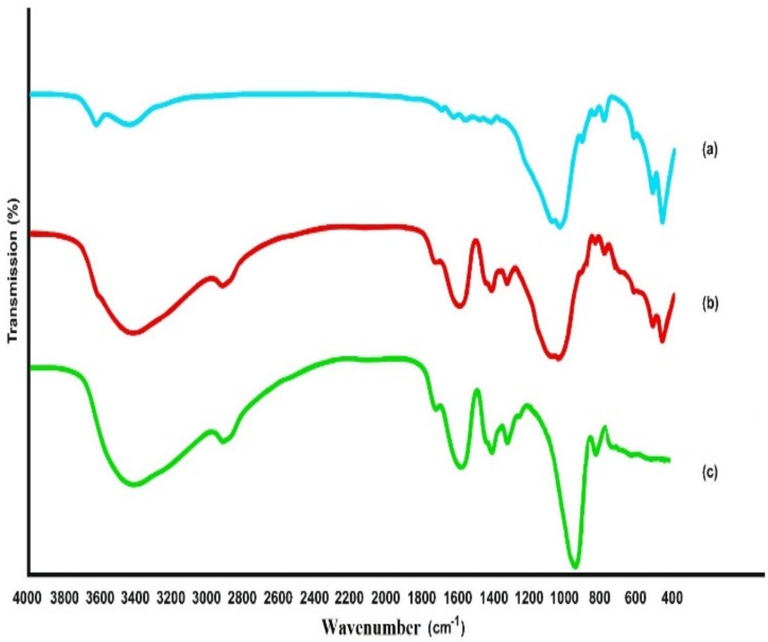

Figure 1. FTIR spectra of a) MMT powder, b) MMT/CG hydrogel, c) CG powder

XRD

The XRD diffractograms of the MMT powder, CG powder, MMT/CG-composite hydrogel (with MMT/CG mass ratio of 0.3:1 as representative sample) are shown in Figure 2. The sharp characteristic peak of MMT at nearly 6.00°2Ɵ was observed, whereas this peak was not occurred in the diffractogram of CG powder and MMT/CG hydrogel. This can be explained by the connection of CG molecules into the MMT layer. Additionally, two peak were observed at 20-25°2Ɵ for MMT powder, whereas CG powder, MMT/CG-composite hydrogel have a wider peak.

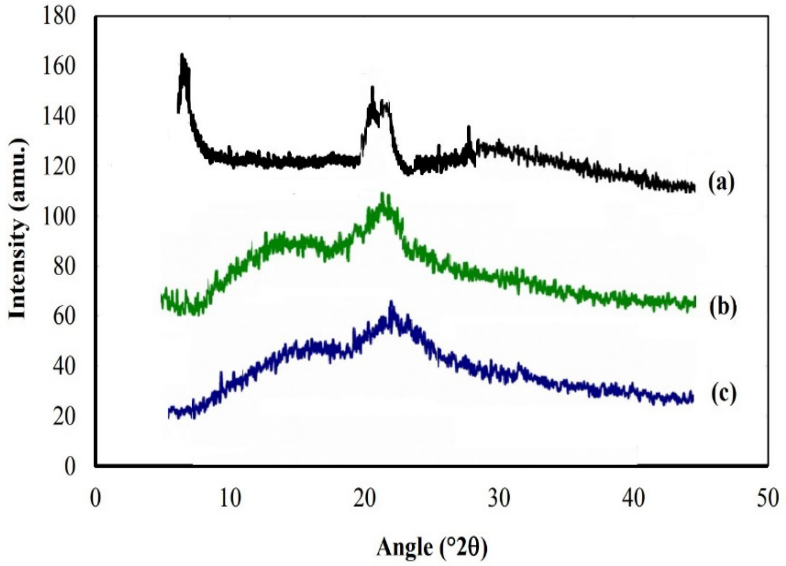

Figure. 2. XRD diffractograms of a) MMT powder, b) MMT/CG, c) CG powder

SEM

SEM images of MMT/CMC-composite hydrogels with different mass ratios are given in Figure 3. It was clearly seen that the surfaces of all hydrogels were rough. The most roughness was observed for MMT/CG (0.3:1) hydrogel. Surface roughness increased with increasing amount of MMT. This can be explained by the fact that the movement of the CG polymer chains may be interrupted by increasing the content of MMT, this causing the roughness to increase.

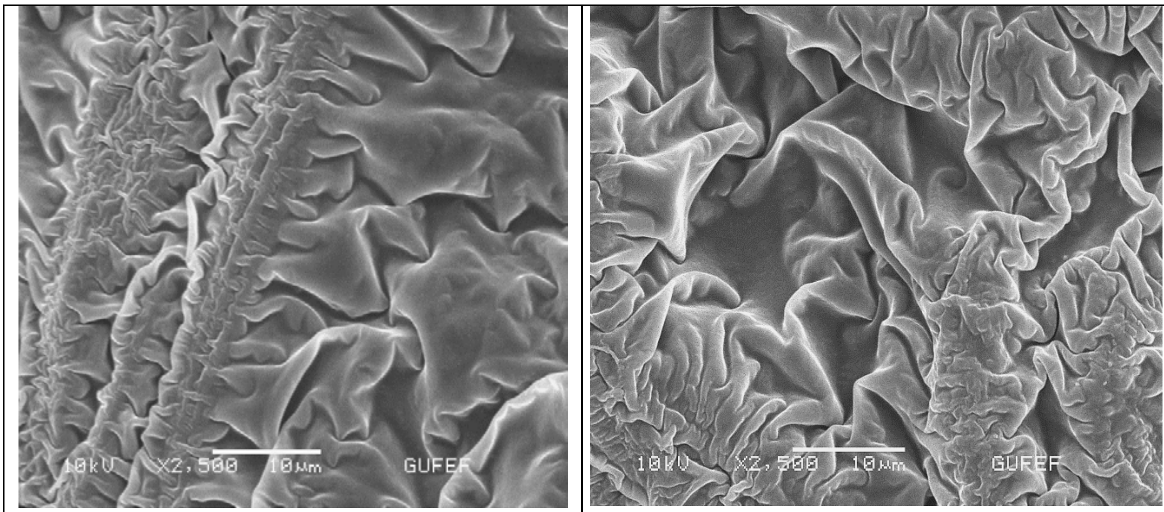

(a)	(b)

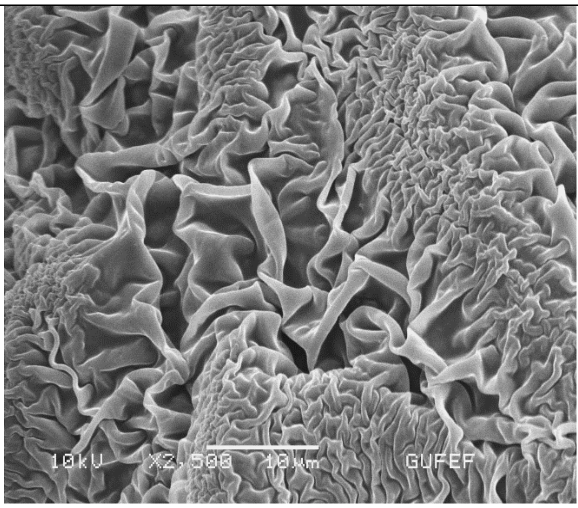

(c)

Figure 3. SEM images of the MMT/CG-composite hydrogel at MMT/CG mass ratios of (a) 0.1:1, (b) 0.2:1 and (c) 0.3:1

Thermal Analysis

The thermal properties of hydrogels were researched by TGA analysis. The TGA thermogram of the MMT/CG hydrogel, compared with those of the CG and MMT powders and, is given in Figure 4. At 25°C to 800°C, the weight loss (%) of the MMT/CG hydrogel was lower than that of CG powder, which demonstrated a good thermal stability of the MMT/CG-composite hydrogel than that of the CG powder The results are compatible with the literature (Rojsitthisak et.al, 2019).

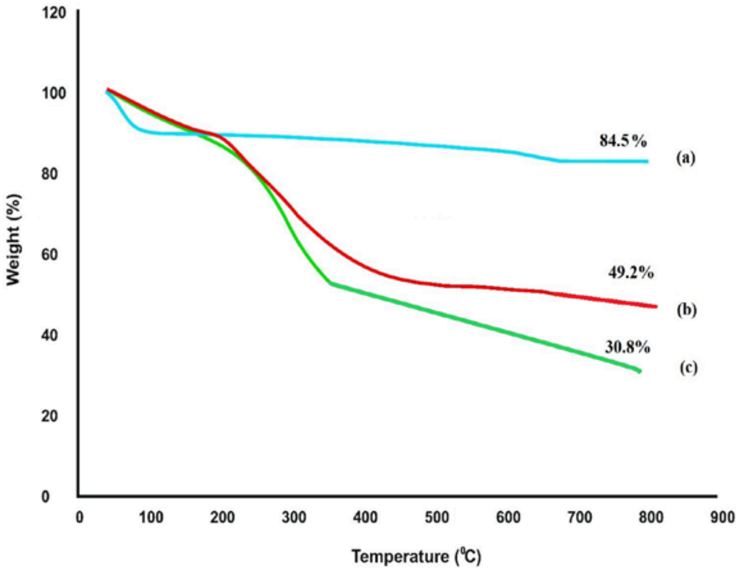

Figure 4. TGA thermogram of a) MMT powder, b) MMT/CG, c) CG powder

Adsorption Studies

The effects of contact time on the adsorption capacity (Q_t) of MMT/CG-composite hydrogels (mass ratio of MMT/CG 0.1:1 and 0.3:1) (initial concentration = 80 mg/L, without adjusted pH) were researched. While the contact time increased, the uptake rate of Cr (VI) ions accelerated and then, it reached a constant value. Firstly, the functional groups of the structure interact with metal ion easily. Thus, the adsorption became to increase. Over time, the adsorption rate slowed down and reached equilibrium. The adsorption capacity values increased gradually till 300 min and then the rate slowed down. The equilibrium adsorption value was found to be 71.4± 0.4 mg/g for MMT/CG hydrogel (0.1:1), while the equilibrium adsorption value was found to be 77.2 ± 0.3

mg/g for MMT/CG hydrogel (0.3:1). This difference can be explained by the increment of MMT made easier the penetration of water containing metal ion into the structure and so, the adsorption rate increased (Yang et. al, 2018).

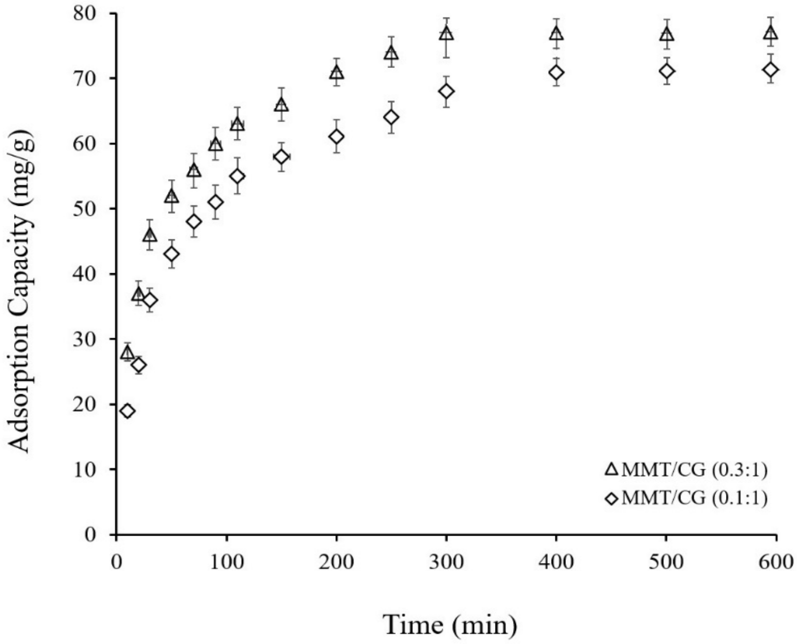

Figure 5. Effect of contact time on *Cr(VI)* metal ions adsorption capacity of MMT/CG hydrogel (initial metal ion concentration = 80 *mg/L*, without adjusted pH). Data are shown as mean ± SD of 3 independent trials.

Table 1. Equilibrium swelling degree of MMT/CG hydrogel beads

Samples	Swelling Degree (%)	Time
MMT/CG (0.1:1.0)	65.4± 0.2	600 min
MMT/CG (0.1:1.0)	72.4± 0.6	600 min

Note: Data are shown as mean ± SD of 3 independent trials

The effect of pH on the adsorption efficiency of MMT/CG hydrogel (0.1:1.0 and 0.3:1.0) is given in Figure 6. Samples were put into 50 mL of *Cr(VI)* solutions (80 mg/l) of different pH values. Initially, the adsorption increased speedily until pH 6. The maximum adsorption was obtained at pH 6 and then, it steadily decreased. Similar findings were reported in literature.

According to literature, *Cr(VI)* have various oxoanionic forms in aqueous solution at different pH. At pH 1.0, it is in the form of H_2CrO_4. Between pH 1–6, it is in the form of $HCrO_4^-$, which dimerizes to $Cr_2O_7^{2-}$ within the release of water molecules into the medium. Above pH 6, $Cr_2O_7^{2-}$ are reduced to form CrO_4^{2-}. formed, the electrostatic attraction increases thanks to this ionic form and the adsorption capacity also increases. Above pH 6, Cr (VI) is in the form of $Cr_2O_4^{2-}$. The positively charged adsorbent adsorbed Cr (VI) metal ions. After pH 6, two diavelent negative ions ($Cr_2O_4^{2-}$ and CrO_4^{2-}) exist in the medium. These ions alter the charge of the composite hydrogel from positive to negative, thus the electrostatic interaction between adsorbent to metal ions is decreased (Bhattacharyya & Sen Gupta, 2006; Khan et.al, 2017; Lei, Su, & Tian, 2018).

$2H_2CrO_4 \leftrightarrow 2H^+ + 2HCrO_4^-$ pH= 1

$2HCrO_4^- \leftrightarrow Cr_2O_7^{2-} + H_2O$ pH 1-6

$Cr_2O_7^{2-} + H_2O \leftrightarrow 2CrO_4^{2-} + 2H^+$ pH> 6

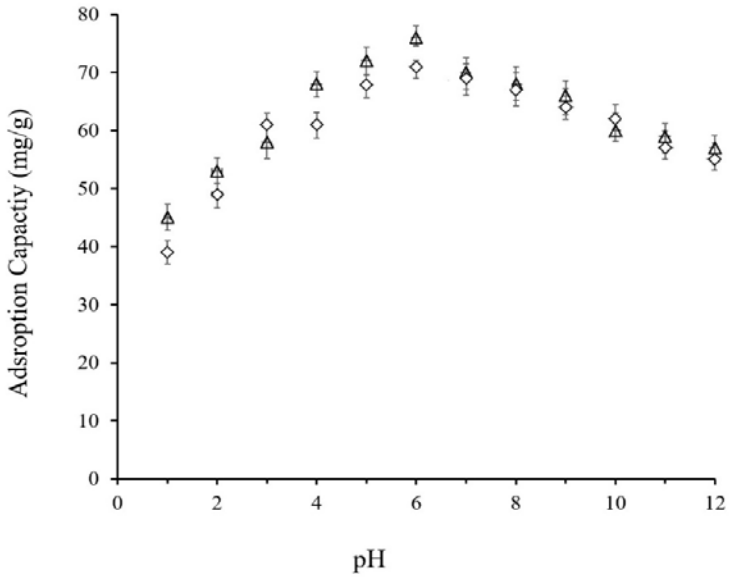

Figure 6. The effect of pH on the adsorption of *Cr(VI)* ions (under the conditions initial *Cr(VI)* concentration of 80 mg/L, temperature 25^{o}C in period of 600 min). Results shown are mean ± standard deviation, n = 3.

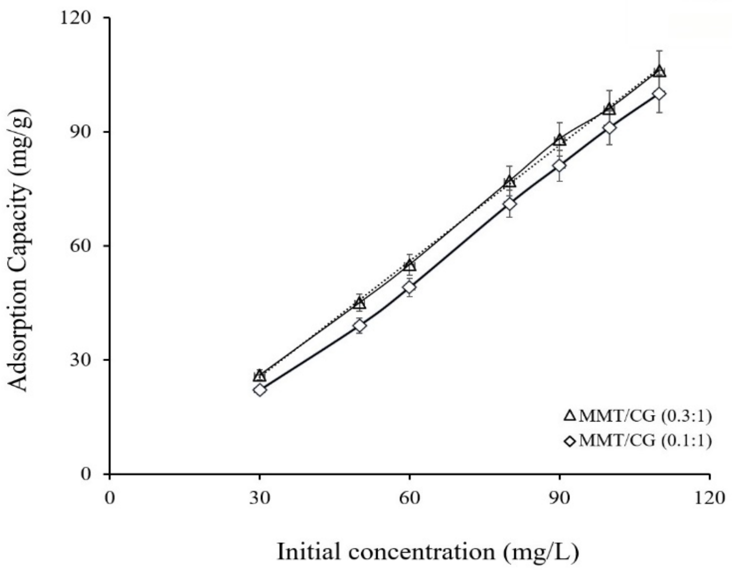

Figure 7. Effect of initial concentration on *Cr (VI)* metal ions adsorption capacity of MMT/CG hydrogel (pH = 7, contact time=600 min). Data are shown as mean ± SD of 3 independent trials.

The adsorption capacity (Q_t) of MMT/CG-composite hydrogels (mass ratio of MMT/CG 0.1:1 and 0.3:1) were investigated, the results are given in Figure 4. The adsorption capacity depends on initial concentration (*Ci*), in other words, *Qt* changed directly with *Ci* (Maity, & Ray 2016). The amount of adsorbed metal ions enhanced with increasing *Ci* value, so Q_t was increased. Q_t value of MMT/CG (0.3:1) changed from 26 to 106 mg/g, while Q_t value of MMT/CG (0.1:1) ranged from 22 to 100 mg/g. The highest Q_t value was obtained for MMT/CG (0.3:1).

An adsorption isotherm uses for the determination between the content of a metal ions adsorbed on adsorbent and the amount of the dissolved metal ions in solution at equilibrium. Additionally, it can describe the interaction between adsorbent and metal ions. Langmuir isotherm is commonly utilized to model the adsorption of metal ions on polymeric absorbent (Yu et.al, 2017; Yan et. al, 2018; Vilela et.al, 2019). According to this isotherm, adsorption takes place in certain homogeneous regions on the adsorbent, and no further adsorption takes place in the place occupied by the adsorbate.

Langmuir isotherm model was utilized for detecting the adsorption isotherm. The isotherm equation is given in below:

$$1/Qe = \frac{1}{Q_{max} x\, b\, x\, Ce} + \frac{1}{Q_{max}} \quad (1)$$

where *Qe* is the adsorption capacity of the adsorbent at equilibrium, *Ce* is the metal ion concentration at equilibrium time, *b* is the Langmuir constant and Q_{max} is the maximum monolayer adsorption capacity. The correlation coefficient (R^2) was calculated for two samples from the graph. R^2 was found to be 0.9980 and 0.9984 for MMT/CG (0.1:1.0) and MMT/CG (0.3:1.0), respectively. The correlation coefficient close to 1 represents monolayer adsorption of metal ions on the adsorbent.

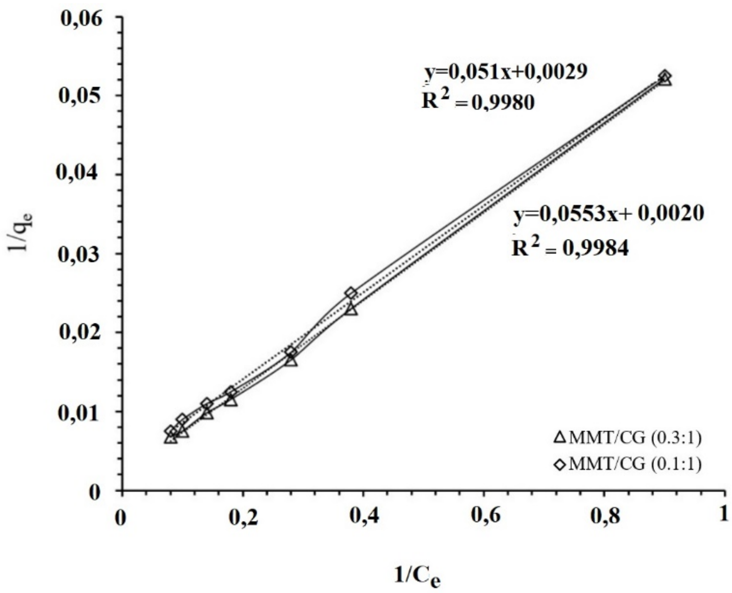

Figure 8. Langmuir isotherm for adsorption of Cr (VI) ions (under the conditions pH=6, temperature 25°C in period of 600 min).

Conclusions

Composite MMT/CG-hydrogels have the potential for being used as a polymeric adsorbent for the removal of *Cr(VI)* metal ions from aqueous solution. The maximum adsorption capacity of MMT/CG at a mass ratio of 0.3:1. The adsorption process can be described by the Langmuir isotherm model.

Scientific Ethics Declaration

The author declares that the scientific ethical and legal responsibility of this article published in EPSTEM journal belongs to the author.

Acknowledgements or Notes

* This article was presented as an oral presentation at the International Conference on Basic Sciences, Engineering and Technology (www.icbaset.net) conference held in Istanbul/Turkey on August 25-28, 2022.

References

Ahmed, E. M. (2015). Hydrogel: preparation, characterization, and applications: A review. *Journal of advanced research*, *6*(2), 105-121.

Alemayehu, D. D., Singh, S. K. & Tessema, D. A. (2012). Assessment of the adsorption capacities of fired clay soils from Jimma (Ethiopia) for the removal of Cr (VI) from aqueous solution. *Universal Journal of Environmental. Research & Technology, 2*(5).

Bhattacharyya, K. G. & Sen Gupta, S. (2006). Adsorption of chromium (VI) from water by clays. *Industrial & Engineering Chemistry Research, 45*(21), 7232-7240.

Dakiky, M., Khamis, M., Manassra, A. & Mer'Eb, M. (2002). Selective adsorption of chromium (VI) in industrial wastewater using low-cost abundantly available adsorbents. *Advances in Environmental Research, 6*(4), 533-540.

Hayati-Ashtiani, M. (2011). Characterization of nano-porous bentonite (montmorillonite) particles using FTIR and BET-BJH analyses. *Particle & Particle Systems Characterization, 28*(3-4), 71-76.

Ianchis, R., Ninciuleanu, C. M., Gifu, I. C., Alexandrescu, E., Nistor, C. L., Nitu, S. & Petcu, C. (2020). Hydrogel-clay nanocomposites as carriers for controlled release. *Current Medicinal Chemistry, 27*(6), 919-954.

Islam, M. A., Angove, M. J. & Morton, D. W. (2019). Recent innovative research on chromium (VI) adsorption mechanism. *Environmental Nanotechnology, Monitoring & Management, 12,* 100267.

Kaşgöz, H. & Durmus, A. (2008). Dye removal by a novel hydrogel-clay nanocomposite with enhanced swelling properties. *Polymers for Advanced Technologies, 19*(7), 838-845.

Khan, T. A., Nazir, M., Ali, I. & Kumar, A. (2017). Removal of chromium (VI) from aqueous solution using guar gum–nano zinc oxide biocomposite adsorbent. *Arabian Journal of Chemistry, 10,* S2388-S2398.

Lei, Y., Su, H. & Tian, F. (2018). A novel nitrogen enriched hydrochar adsorbents derived from salix biomass for Cr (VI) adsorption. *Scientific reports, 8*(1), 1-9.

Maity, J. & Ray, S. K. (2016). Enhanced adsorption of Cr (VI) from water by guar gum based composite hydrogels. *International Journal of Biological Macromolecules, 89,* 246-255.

Pereira, L., Sousa, A., Coelho, H., Amado, A. M. & Ribeiro-Claro, P. J. (2003). Use of FTIR, FT-raman and 13C-NMR spectroscopy for identification of some seaweed phycocolloids. *Biomolecular Engineering, 20*(4-6), 223-228.

Rojsitthisak, P., Hansapaiboon, S., Sorasitthiyanukarn, F. N. & Limpanart, S. (2019). Montmorillonite/carboxymethylcellulose-composite hydrogel beads as biodegradable adsorbent for dye removal. *Maejo International Journal of Science and Technology, 13*(3), 170-184.

Sharma, G., Khosla, A., Kumar, A., Kaushal, N., Sharma, S., Naushad, M., ... & Stadler, F. J. (2022). A comprehensive review on the removal of noxious pollutants using carrageenan based advanced adsorbents. *Chemosphere, 289*, 133100.

Vilela, P. B., Dalalibera, A., Duminelli, E. C., Becegato, V. A. & Paulino, A. T. (2019). Adsorption and removal of chromium (VI) contained in aqueous solutions using a chitosan-based hydrogel. *Environmental Science and Pollution Research, 26*(28), 28481-28489.

Yan, E., Cao, M., Ren, X., Jiang, J., An, Q., Zhang, Z., ... & Zhang, D. (2018). Synthesis of Fe_3O_4 nanoparticles functionalized polyvinyl alcohol/chitosan magnetic composite hydrogel as an efficient adsorbent for chromium (VI) removal. *Journal of Physics and Chemistry of Solids, 121*, 102-109.

Yang, X., Li, F., Xia, M., Luo, F. & Jiang, Y. (2018). Investigation on the micro-structure and adsorption capacity of cellulosic biomass carbon based montmorillonite composite. *Microporous and Mesoporous Materials, 256,* 18-24.

Yu, P., Wang, H. Q., Bao, R. Y., Liu, Z., Yang, W., Xie, B. H. & Yang, M. B. (2017). Self-assembled sponge-like chitosan/reduced graphene oxide/montmorillonite composite hydrogels without cross-linking of chitosan for effective Cr (VI) sorption. *ACS Sustainable Chemistry & Engineering, 5*(2), 1557-1566.

Author Information

Gülen Oytun Akalin
Aksaray University
Medical Laboratory Program, Department of Medical Services and Techniques,
Vocational School of Health Service,
Contact e-mail: *gulenoytunakalin@hotmail.com*

To cite this article:

Akalın, G. O. (2022). The preparation of montmorillonite/carrageenan-composite hydrogel for chromium (VI) removal from aqueous solution. *The Eurasia Proceedings of Science, Technology, Engineering & Mathematics (EPSTEM), 18,* 72-80.

The Eurasia Proceedings of Science, Technology, Engineering & Mathematics (EPSTEM)
ISSN: 2602-3199

The Eurasia Proceedings of Science, Technology, Engineering & Mathematics (EPSTEM), 2022

Volume 18, Pages 81-85

ICBASET 2022: International Conference on Basic Sciences, Engineering and Technology

Duty Cycle Detection Method for High Speed Input-Output Systems

Karen MELIKYAN
National Polytechnic University of Armenia (NPUA)

Abstract: A clock coupled duty cycle detection method for high speed input-output is presented in this paper. In High speed systems duty cycle (DC) of output signal needs to be calibrated at 50% for having acceptable performance in the system. The proposed method introduces a synchronous signal in the output of system with 50% duty cycle with maximum 1 % error over process, voltage, and temperature (PVT). Proposed method also compensate input referred offset of DC detector which helps to improve overall system performance. The duty cycle detection method was implemented in 16nm technology with a power supply of 1.2V. With this type of designed architecture, the circuit can provide up to 5Gbps frequency data signal. Experimental results show that proposed architecture is reliable, and it can work operative in high frequency intervals. The presented circuit can be implemented in special serial links of several standards such as Peripheral Component Interconnect (PCI), Universal Serial Bus (USB) and Double Data Rate (DDR).

Keywords: Duty Cycle, detector, high speed, calibration, process-voltage-temperature (PVT)

Introduction

The speed of many systems increases year by year. One of them are DDR systems (Wang, 2015) (Figure 1). Providing a good performance in them become more difficult. So, there arise problems with parameters, such us DC distortion, offset, jitter etc.

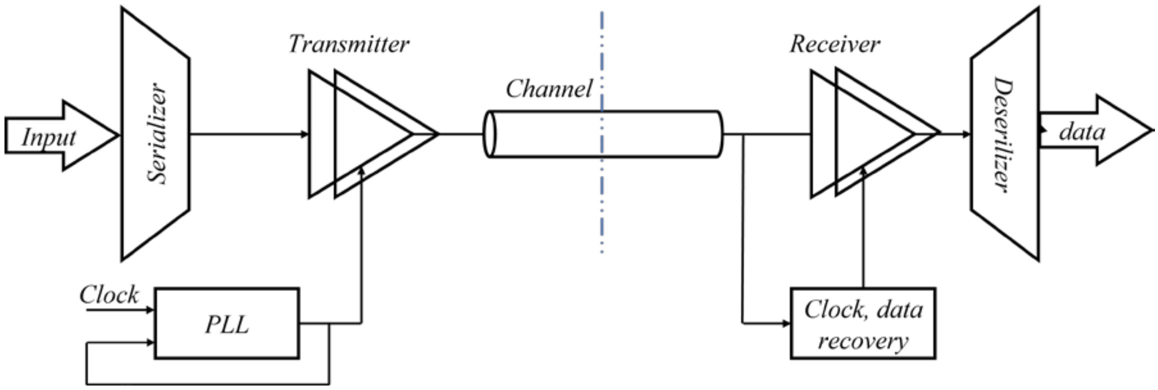

Figure 1. High speed system

Duty Cycle

DC is one of the most important parameters in high speed I/O circuit analyzes. If DC of circuit is not meet 50% specification, then we can have functional error, which can impact on data loss (Sindhu, 2015). DC signal basically measured (1) by pulse width (PW) and the period of signal components (Figure 2).

- Selection and peer-review under responsibility of the Organizing Committee of the Conference

$$DC=(PW/Per)*100\% \quad (1)$$

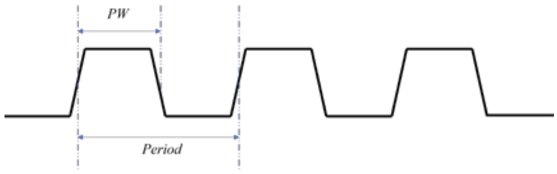

Figure 2. DC main components

Duty Cycle Detection Importance

The DC correction circuit (Melikyan, 2015) main blocks are adjuster and detector (Figure 3). The adjuster regulates a code for getting desired DC and send it to DC detector. The main function of detector is a correct measure of the DC error (%), make a right decision to send it to output and end operation, or continue corrective operation with sending signal to DC adjuster for requesting a new code.

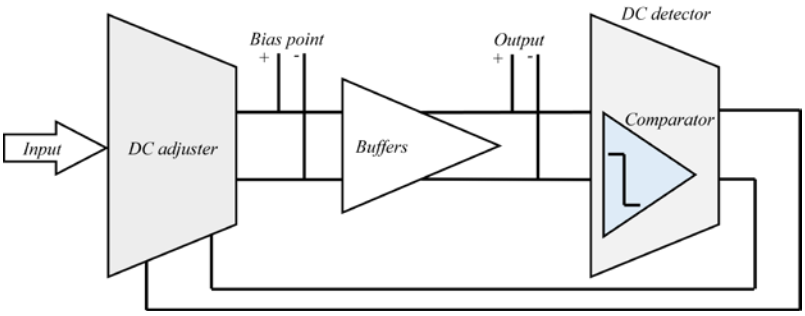

Figure 3. Block diagram of DC correction circuit

As nowadays circuits are working in the high frequency regions (Chien, 2019). The transistors and junctions in them get stressed while operating. So, for having acceptable performance in the system reliable architecture must be designed for DC detector, which can satisfy DC correcting circuit requirements.

Proposed Method of Duty Cycle Detection

Architecture of Duty Cycle Detector

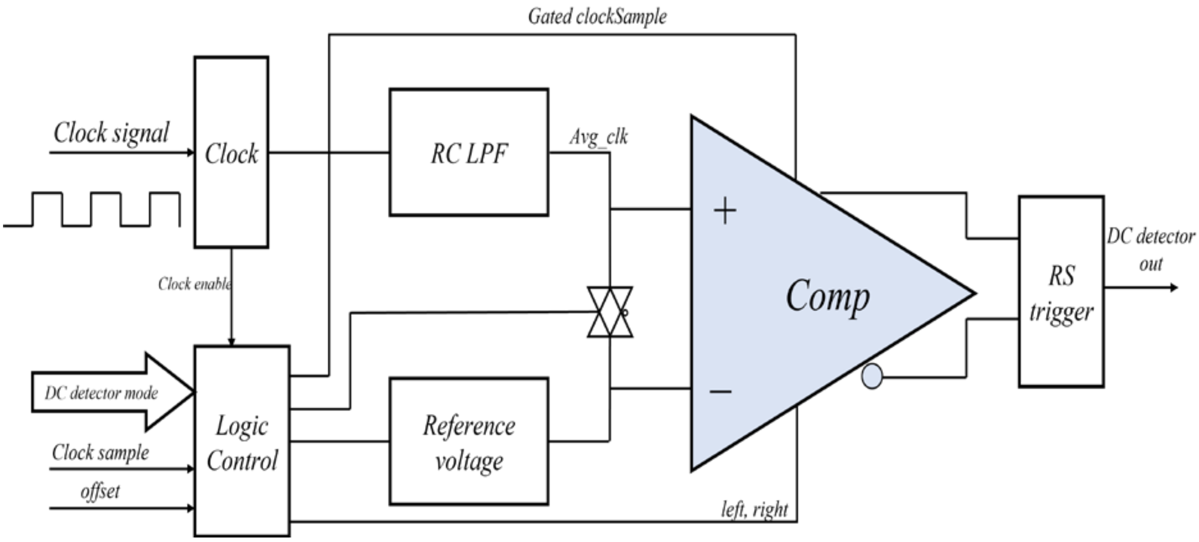

Figure 4. DC detector block diagram

The macro contains (Figure 4),

- digital control logic.
- analog DC detector core, including a mux for two input clocks, two RC tanks, and a comparator

The DC detector has two different functional modes: offset calibration mode and mission mode. The comparator offset is first calibrated in the offset calibration mode. Once it is done, the offset code is stored and used for the mission mode. In power down mode the analog DC detector is not measuring the incoming clock signals. The compactor is in the precharge mode with disabled offset legs. The two inverters are off and the two RC tank outputs are weakly driven to VSS.

Offset calibration mode: The offset code is incremented one by one to check when the comparator output toggles. The offset code is then stored and applied for the mission mode. It should be programmable between min and max code. The offset code either generated by the state-machine or can be overwritten by users. Also sweeping can't be wrapped around. It will be stopped at min or max value. Control and status register (CSR) default for the offset should be equivalent to no offset in the comparator.

The offset receive 5-bit binary code, MSB is the signed bit (1 is negative). Default and reset value is: 5'b00000 (this is the state of no offset). Min value is -15(5b'11111) and the max value +15(5b'01111). Mission mode: clk_sel chooses between the two input clocks. The average of the input clock signal is compared against the voltage divider output that is ideally at VDD/2. The comparator is either 1 or 0 depending on the relative relationship between the average clock and the reference voltage.

Operation Principle

The DC detecing algorithm is shown in block diagram (Figure 5). The Phase Locked Loop (PLL) provides the clock signal. Which pass trough RC filter, where clock signal become fixed in almost half of VDD level (~VDD/2). Logic cantrol block also is in level choosing mode, which will be fixed in the appropriate RC filter and value of signal becomes ~VDD/2. After both signals have been fixed in ~VDD/2 level they pass into key, which corrects offset code when ciruict works in offset mode.

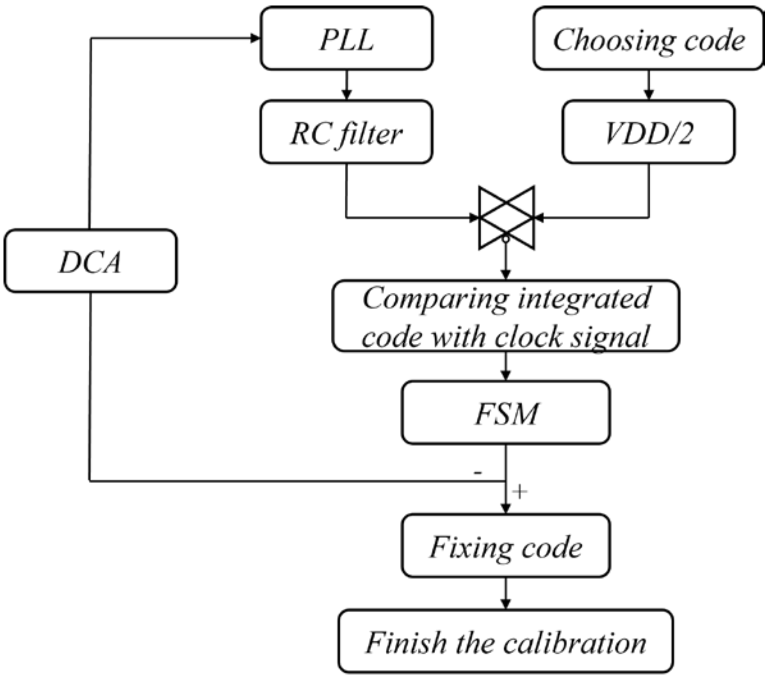

Figure 5. DC detector block diagram

In case of the mission mode the signal from PLL and choosed code get compared with each other to get information about signals level difference (error of DC detector), which must meet DC min/max error value specification. In the case when DC error is out of advisable specification of DC detector, finite state machine (FSM) enters the signal to DC adjuster block where the code will be changed and sent back to PLL block. FSM passes the code and calibrates it until finding the best output signal. After getting acceptable performance FSM fixes code and finishes calibration.

Results and Discussion

Simulations have been performed using circuit level simulator Hspice for 20 PVT corners (Hspice, 2010), including SS (slow-slow), TT (typical-typical), FF (fast-fast), SF (slow-fast), FS (fast-slow) with supply voltage and temperature variations to evaluate DC detection and offset correction of system, for 5Gbps frequency.

After starting operation circuit enters phase of settling. In the moment when settling time was ended, clock signal and chosen code get the appropriate voltage levels, the DC detection phase starts. In the end of operation comparator detects the DC (%) with the error percentage. In Figure 6 are shown DC detection results for FF corner, which is the worst corner in this case (Cosmosscope, 2018).

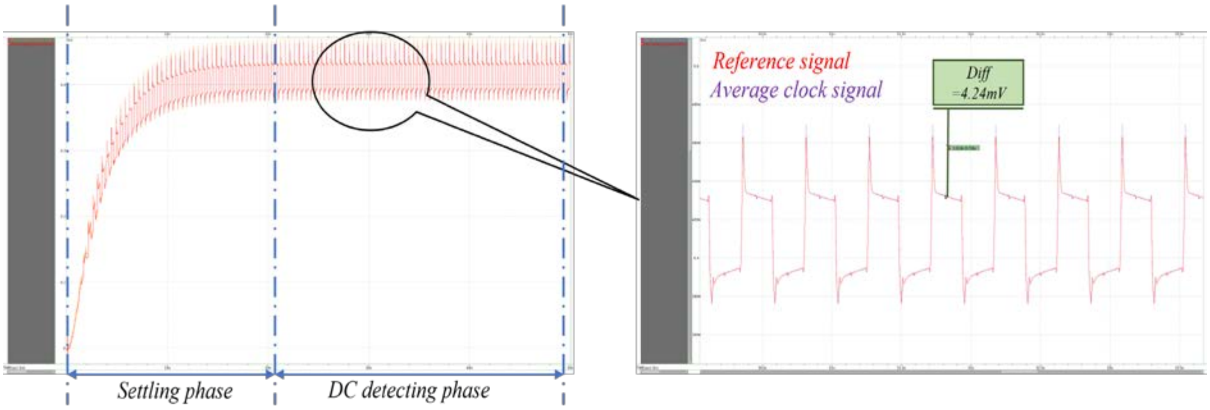

Figure 6. DC detected error in ff corner

In table 1 shown results of TT, FF and SS corners for DC and DC error min/max value.

Table 1. Simulation results for TT, FF, SS corners

Variables	Max difference on gate (mV)	DC detection max error (%)	DC (%)
TT	0.73	0.09	50.01
FF	4.24	0.54	50.61
SS	1	0.12	49.24

Conclusion

DC detection method designed for detecting error of DC in special high speed input-output systems. DC detection circuit used in method assist to maximum error and provide signals only with minimum DC error. The error maximum variation is 50%±1%. The architecture also corrects the offset of circuit with special offset mode implementing.

In high speed systems for 28nm and below processes it is hard to provide good performance without DC detection. So, this type of detection method is very important in special input-output circuits, due to huge PVT variations, which can have impact on the performance of the system. The approached method can be implemented for special input-output protocols of several standards such as DDR, USB, PCI.

Scientific Ethics Declaration

The author declares that the scientific ethical and legal responsibility of this article published in EPSTEM journal belongs to the author.

Acknowledgements or Notes

* This article was presented as an oral presentation at the International Conference on Basic Sciences, Engineering and Technology (www.icbaset.net) conference held in Istanbul/Turkey on August 25-28, 2022.

* This paper was supported by National Armenian Polytechnic University (NPUA). I thank my colleagues from Microelectronics and biomedical equipment departament, who provided insight and expertise that greatly assisted the research.

References

Chien, Y., L. & Heng, S., H. (2019). Design of a 0.8GHz-3GHz duty-cycle corrector with a 20%-80% input duty cycle. *IEEE International Conference on Consumer Electronics - Taiwan (ICCE-TW), 9,* 59-62.

Cosmosscope Reference Manual (2018), *Synopsys Inc,* 130.

Hspice Application Manual (2010), *Synopsys Inc.,*196.

Melikyan, V., Sahakyan, A., Hekimyan, A., Trdatyan, D., Shishmanyan, A. & Kazakhyan, T. (2015). Low power duty cycle adjustment simple method in high speed serial links. *IEEE East-West Design & Test Symposium (EWDTS),* 1-4.

Sindhu, M. & Jamuna, V. (2015). Highly reconfigurable pulse width control circuit with programmable duty cycle. *2nd International Conference on Electronics and Communication Systems (ICECS),* 2, 303-309.

Wang, X., & Hu, Q., (2015). Analysis and optimization of combined equalizer for high speed serial links. *IEEE 9th International Conference on Anti-counterfeiting, Security, and Identification (ASID), 9,* 43-46.

Author Information

Karen Melikyan
National Polytechnic University of Armenia
105 Teryan St, Yerevan, Armenia
Contact e-mail: *melikyan@synopsys.com*

To cite this article:

Melikyan, K. (2022). Duty cycle detection method for high speed input-output systems. *The Eurasia Proceedings of Science, Technology, Engineering & Mathematics (EPSTEM), 18,* 81-85.

The Eurasia Proceedings of Science, Technology, Engineering & Mathematics (EPSTEM)
ISSN: 2602-3199

The Eurasia Proceedings of Science, Technology, Engineering & Mathematics (EPSTEM), 2022

Volume 18, Pages 86-101

ICBASET 2022: International Conference on Basic Sciences, Engineering and Technology

Exploring the Risky Areas Due to Landslide Using Decision Tree Analysis: Case Study Tasmania, Australia

Mahyat SHAFAPOURTEHRANY
Bogazici University

Abstract: Landslide is one of the natural hazards that considers a serious threat to both humans' lives and properties. Tasmania, Australia is one of those regions where landslides caused considerable damage to people and the State. Landslide damages can be reduced, even stopped, if proper land condition and planning assessment has been done. The main influencing parameters in landslide occurrences are topography, precipitation, and geological formation. Those parameters along with other influencing parameters have been used in landslide susceptibility mapping. In order to have a reliable analysis, a robust method of Decision Tree (DT) has been used to perform susceptibility mapping. According to the hierarchy structure of DT, geology and slope have been selected as the most influential parameters in landslide susceptibility. In order to evaluate the reliability of the outcomes, Area Under the Curve (AUC) has been utilized. Success and prediction rates were 87.64% and 84% respectively. Subsequently, risky features such as buildings, schools, hotels, etc. have been used in overlay analysis in a GIS environment with "very high" and "high" susceptibility classes. The outcome of this research can assist planning parties to secure vulnerable regions and consider those areas in their future decision-making strategies.

Keywords: Landslide, Decision Tree (DT), Vulnerability, GIS, Tasmania

Introduction

Natural hazards are a great threat to both lives and properties worldwide (Jia et al., 2021). These include flooding, wildfire, earthquake, landslides, etc. Among natural disasters, landslides can cause serious losses directly or indirectly to the society and economy (Del Soldato et al., 2017). They are related to the characteristics of the slope of the terrain (Sim et al., 2022). One way to minimize the damage of landslides is to recognize the susceptible regions that are most likely to occur (Park et al., 2018). In the natural hazard scope, a susceptibility map recognizes regions that are more or less disposed to a potential landslide occurrence using low to high possibility values/classes (Ballabio & Sterlacchini, 2012). Susceptibility assessment has been implemented by several researchers to prevent or reduce actual damage from natural hazards. Until now, various methodological approaches including qualitative and quantitative methods have been applied for landslide susceptibility mapping (Reichenbach et al., 2018).

There is a variety of methods available in the literature to identify landslide susceptible areas such as frequency ratio (FR) (Lee & Sambath, 2006), logistic regression (LR) (Lee, 2005), index of entropy (IoE) (Pourghasemi, Mohammady, et al., 2012), the weight of evidence (WoE) (Lee & Choi, 2004), evidential belief function (EBF) (Althuwaynee et al., 2012), statistical index (Regmi et al., 2014), analytical hierarchy process (AHP) (Kumar & Anbalagan, 2016), fuzzy logic (Pourghasemi, Pradhan, et al., 2012), fuzzy rule-based classifiers (Pham, Tien Bui, et al., 2016), neuro-fuzzy models multivariate adaptive regression splines (MARS) (Chu et al., 2019), random forest (RF) (Hong et al., 2019), (DT) (Park et al., 2018), Artificial neural network (ANN) (Lee et al., 2004), and support vector machines (SVM) (H. R. Pourghasemi et al., 2013), and etc. Each of the aforementioned methods has advantages and disadvantages (Reichenbach et al., 2018). Though, machine learning is a category of methods that are repeatedly used in natural hazard studies (Korup & Stolle, 2014).

- Selection and peer-review under responsibility of the Organizing Committee of the Conference

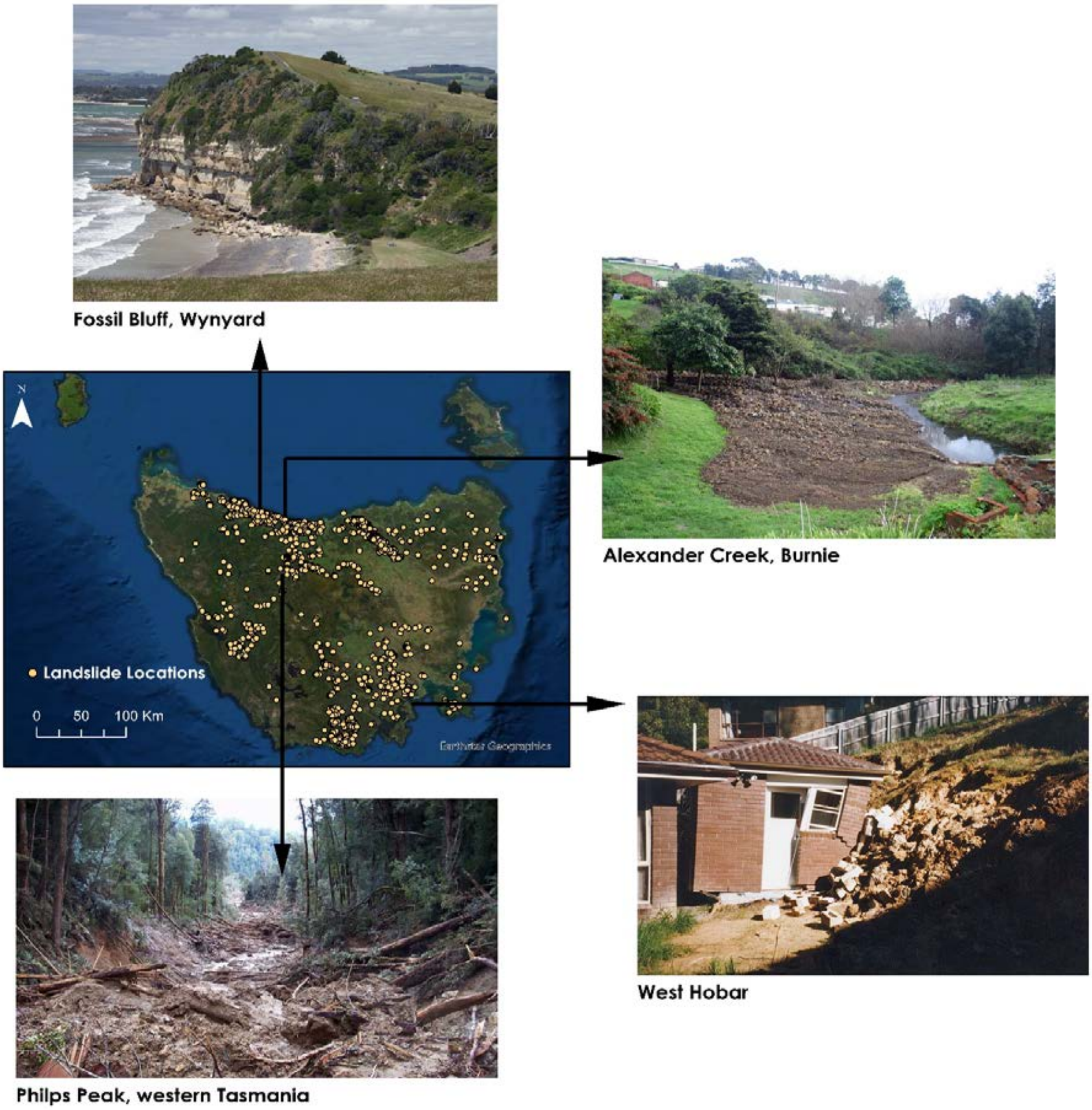

Figure 1. Distribution of landslides in Tasmania along with a few examples of the affected areas (BAY)

Machine learning is related to a set of methods that distinguish patterns in the dataset and use them to predict future scenarios (Jain et al., 2020). One of the differences between machine learning methods and other approaches is that without any pre-defined rules from experts, they can learn their own mappings between parametric rules directly from the data. This characteristic is advantageous in the case that the number of factors is considerably large and their physical properties are quite complex, as in the case of landslide (Merghadi et al., 2020). Hence, the machine learning approach to landslide response may assist to avoid many of the limitations of physics-based algorithms. In this study, we applied the machine learning method of DT using landslide data collected in the 1950s.

Australia has been affected by several landslides in the past (Roodposhti et al., 2019). Some lands in Tasmania are susceptible to slope instability (Slee & McIntosh, 2022). In some cases, the financial damage to people and the State reaches millions of dollars. However, there is no information source that people can use to get informed about landslide risk (Mazengarb, 2005). In addition, neither the insurance company nor the Tasmanian government provides coverage for those damages (Roodposhti et al., 2019). Without any doubt, such disasters and their destructive impacts can be avoided if the ground conditions are evaluated and assessed prior to the planning and construction (Dai et al., 2002).

In order to create safer and sustainable communities land use planning strategies are required (Chakraborty & Anbalagan, 2013; Sultana & Tan, 2021). Some of the planning actions are: to avoid development in areas that will increase the likelihood of landslide risk; to remove or modify structures in risky zones; to recognize high-risk areas through zoning and overlay controls, and to avoid developments that are more likely to contribute to increased landslide risk.

According to the above information, since landslide conditions in Tasmania received less attention in the literature, this study contributes to a better understanding of the landslide risky areas in Tasmania, Australia by overlaying the landslide susceptible areas with risky locations. Using this analysis to identify the risky areas can be a great tool for several end-users (private and public sectors), intended for landslide mitigation purposes at both local and international levels.

Study Area and Data Used

Landslides are common in Tasmania due to the natural geological processes over long-time scales (Figure 1). Due to its varied topographical, geological, and geomorphic processes, including the effects of past and present climates, landslides occur in a variety of sizes and types (Mazengarb & Stevenson, 2010). Mineral Resources Tasmania (MRT) stated that due to the nature and magnitude of the known past landslides, similar events occurring today would have the potential for significant damage in the future (https://www.mrt.tas.gov.au/home). The five major landslide types (slide, flow, fall, topple and spread) all can happen in Tasmania, with slides (both shallow and deepseated) and flows being the most common types. A number of landslides are a combination of movement types. The material that moves is classed as rock, earth, or debris.

In order to have efficient mitigation strategies, defining the landslide conditioning factors must be also highlighted throughout the spatial domain (Roodposhti et al., 2019). A relevant and reliable landslide conditioning factors dataset with accurate landslide inventories is essential for landslide susceptibility analysis. Both datasets' precision has a direct impact on the final outcomes (Meena et al., 2022). For the current research, the conditioning factors are altitude, slope, aspect, forest, geology, landuse/cover (LULC), Normalized Difference Vegetation Index (NDVI), rain, distance to the river, distance to road, and soil (Figure 2). Each factor was resized to a 30 × 30 m grid. Each one of these factors has an impact on landslide occurrence in a region.

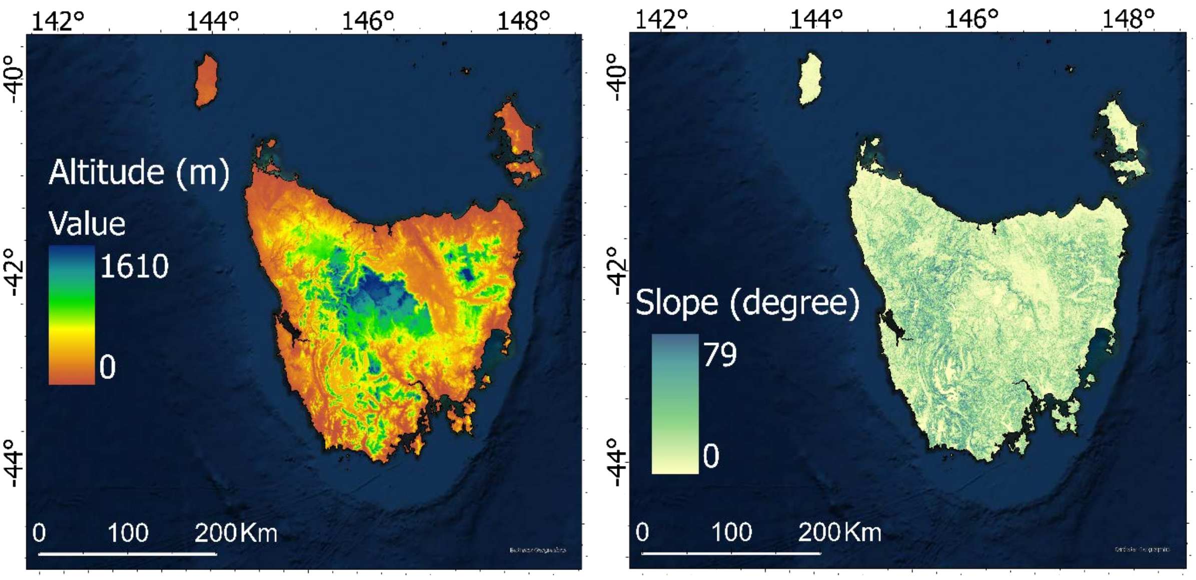

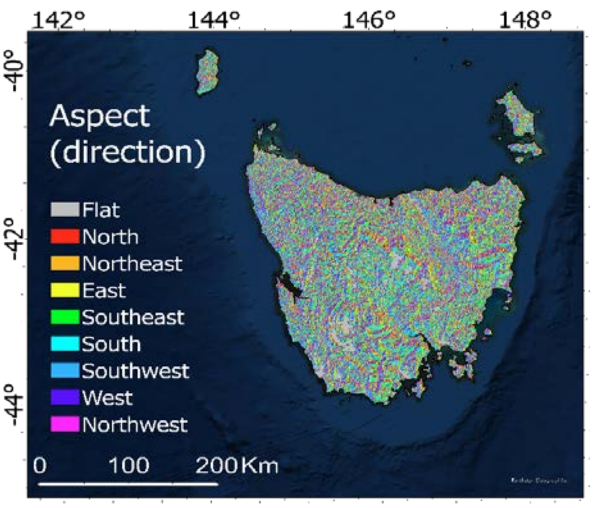
142° 144° 146° 148°
-40° -42° -44°
Aspect (direction)
Flat
North
Northeast
East
Southeast
South
Southwest
West
Northwest
0 100 200Km

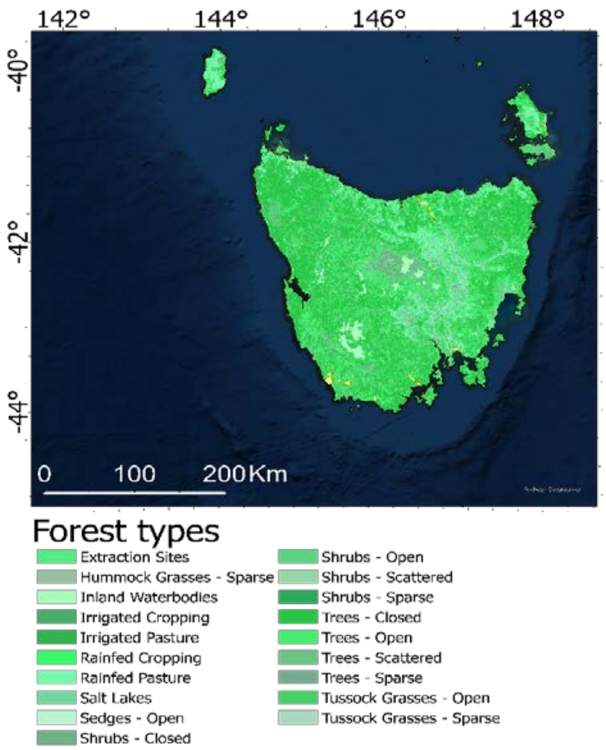
142° 144° 146° 148°
-40° -42° -44°
0 100 200Km
Forest types
Extraction Sites
Hummock Grasses - Sparse
Inland Waterbodies
Irrigated Cropping
Irrigated Pasture
Rainfed Cropping
Rainfed Pasture
Salt Lakes
Sedges - Open
Shrubs - Closed
Shrubs - Open
Shrubs - Scattered
Shrubs - Sparse
Trees - Closed
Trees - Open
Trees - Scattered
Trees - Sparse
Tussock Grasses - Open
Tussock Grasses - Sparse

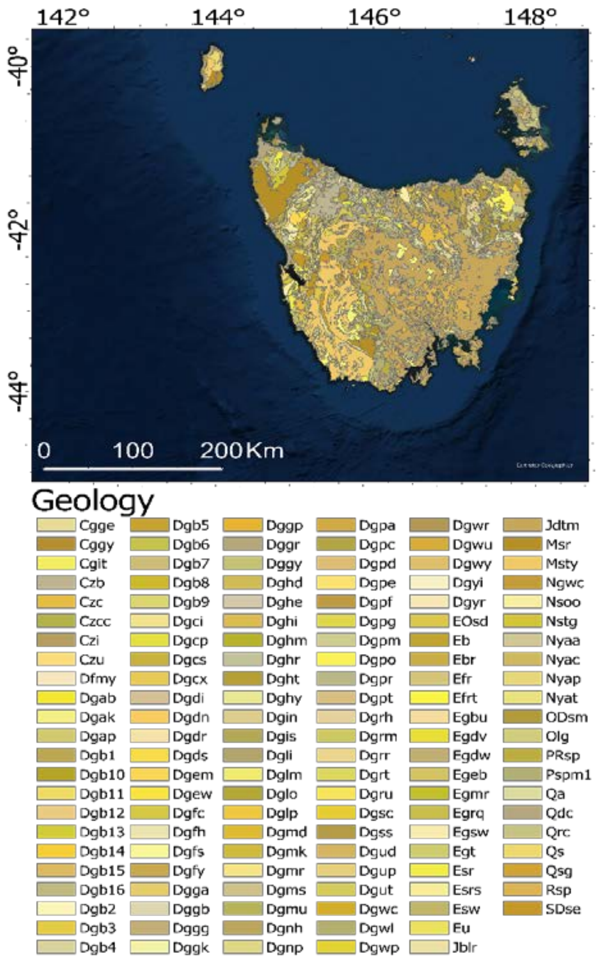
142° 144° 146° 148°
-40° -42° -44°
0 100 200Km
Geology
Cgge
Cggy
Cglt
Czb
Czc
Czcc
Czi
Czu
Dfmy
Dgab
Dgak
Dgap
Dgb1
Dgb10
Dgb11
Dgb12
Dgb13
Dgb14
Dgb15
Dgb16
Dgb2
Dgb3
Dgb4
Dgb5
Dgb6
Dgb7
Dgb8
Dgb9
Dgci
Dgcp
Dgcs
Dgcx
Dgdi
Dgdn
Dgdr
Dgds
Dgem
Dgew
Dgfc
Dgfh
Dgfs
Dgfy
Dgga
Dggb
Dggg
Dggk
Dggp
Dggr
Dggy
Dghd
Dghe
Dghi
Dghm
Dghr
Dght
Dghy
Dgin
Dgis
Dgli
Dglm
Dglo
Dglp
Dgmd
Dgmk
Dgmr
Dgms
Dgmu
Dgnh
Dgnp
Dgpa
Dgpc
Dgpd
Dgpe
Dgpf
Dgpg
Dgpm
Dgpo
Dgpr
Dgpt
Dgrh
Dgrm
Dgrr
Dgrt
Dgru
Dgsc
Dgss
Dgud
Dgup
Dgut
Dgwc
Dgwl
Dgwp
Dgwr
Dgwu
Dgwy
Dgyi
Dgyr
EOsd
Eb
Ebr
Efr
Efrt
Egbu
Egdv
Egdw
Egeb
Egmr
Egrq
Egsw
Egt
Esr
Esrs
Esw
Eu
Jblr
Jdtm
Msr
Msty
Ngwc
Nsoo
Nstg
Nyaa
Nyac
Nyap
Nyat
ODsm
Olg
PRsp
Pspm1
Qa
Qdc
Qrc
Qs
Qsg
Rsp
SDse

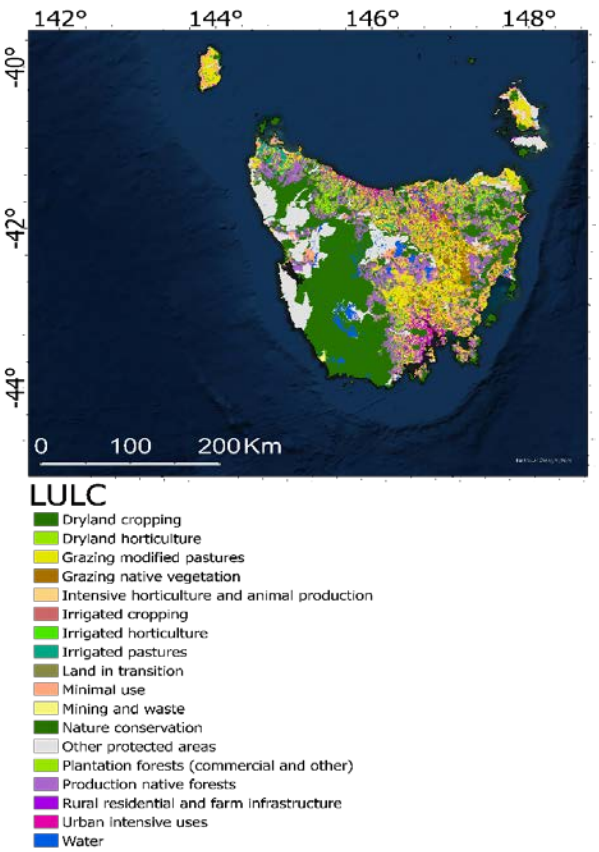
142° 144° 146° 148°
-40° -42° -44°
0 100 200Km
LULC
Dryland cropping
Dryland horticulture
Grazing modified pastures
Grazing native vegetation
Intensive horticulture and animal production
Irrigated cropping
Irrigated horticulture
Irrigated pastures
Land in transition
Minimal use
Mining and waste
Nature conservation
Other protected areas
Plantation forests (commercial and other)
Production native forests
Rural residential and farm infrastructure
Urban intensive uses
Water

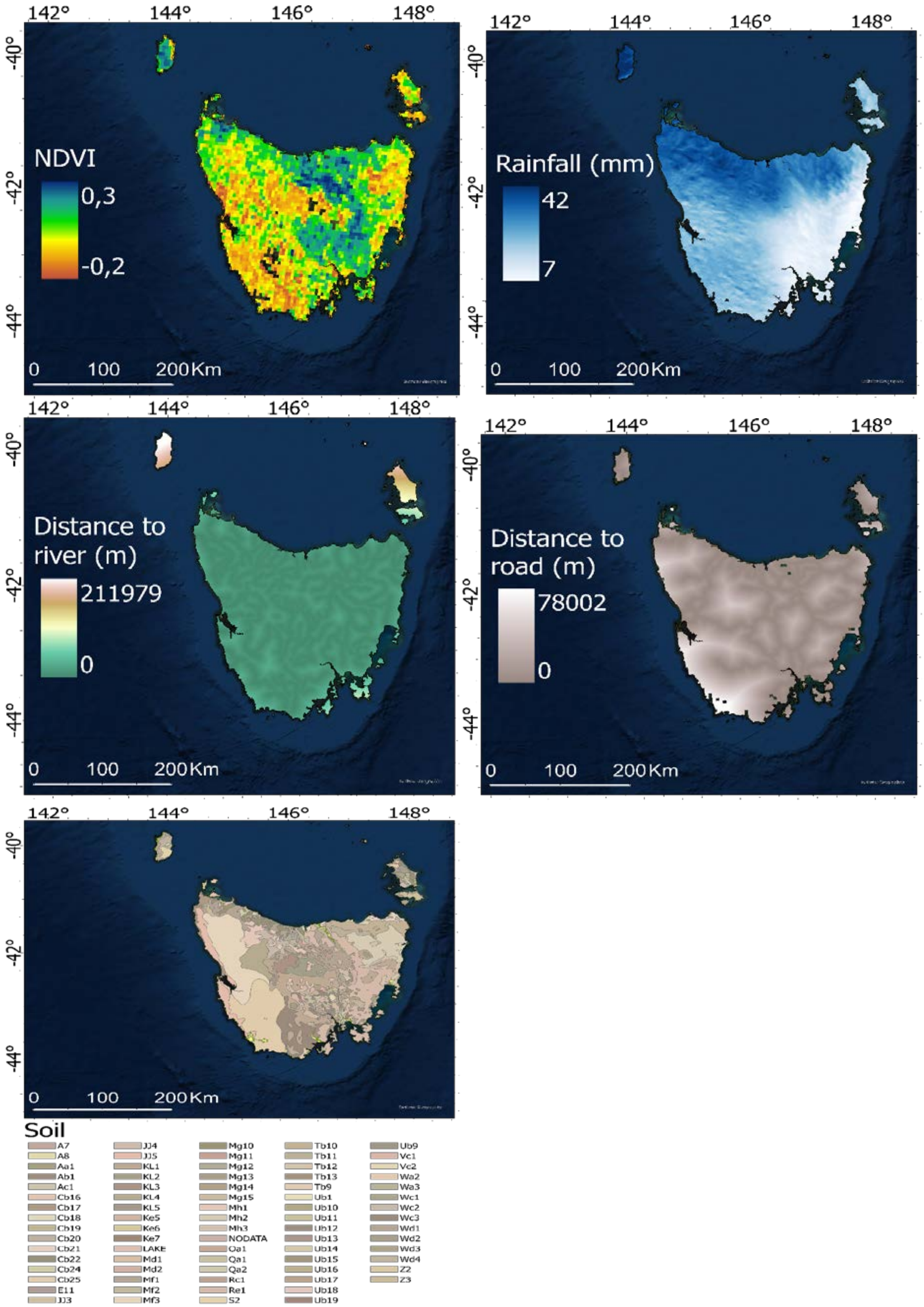

Figure 2. Landslide conditioning factors

Regarding the risky features, the Tasmania government website provided a set of factors such as ambulance, buildings, children and elderly population density, cultural places, educational places, entertainment places, governmental places, heritage Tasmania features, hotels, kindergarten, medical services, police stations, primary infant schools, private reserves, and tourist features. The aforementioned dataset has been used in risk analysis which will be described in the following sections.

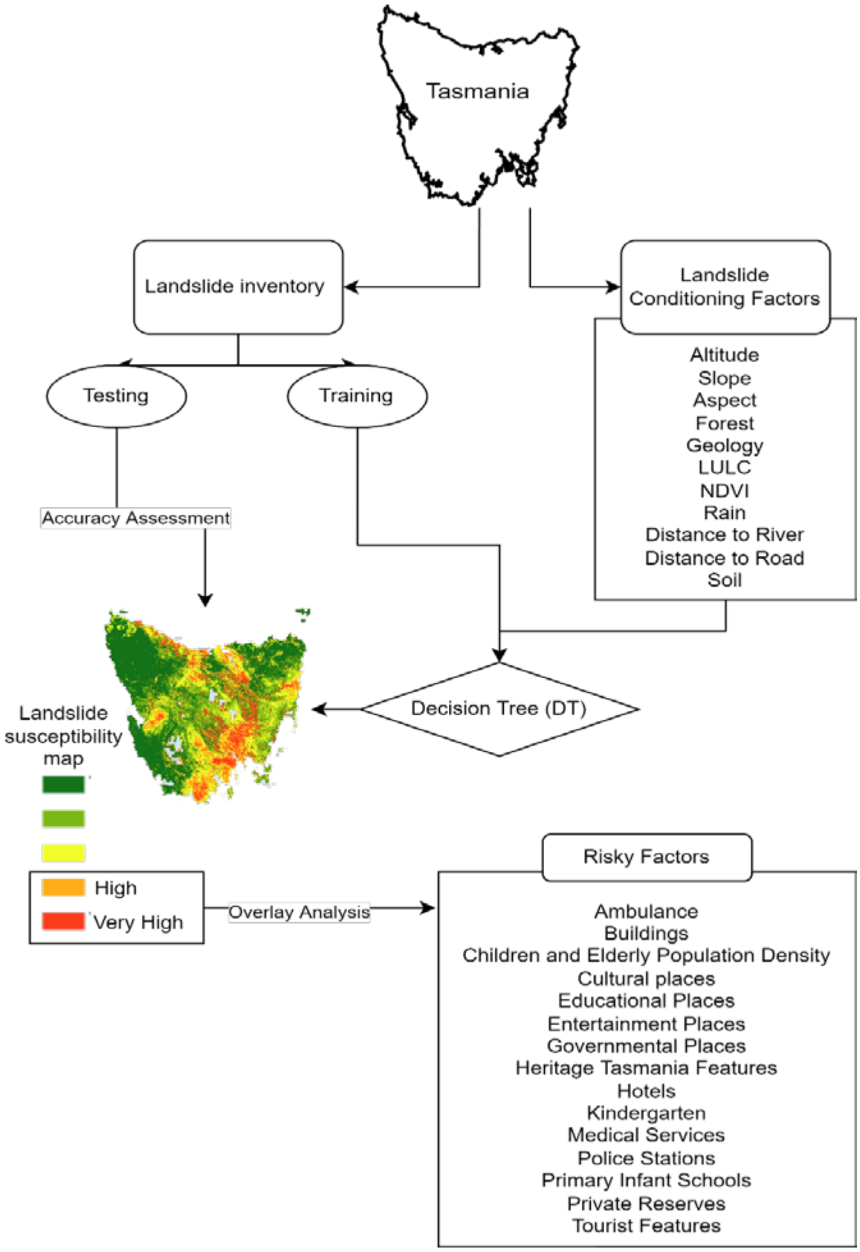

Figure 3. Flowchart

Methodology

Analyzing the correlation between "landslide conditioning factors" and "landslide inventory" is the first stage in landslide susceptibility analysis. Therefore, according to the flowchart (Figure 3), both datasets of conditioning and inventory have been produced. As has been mentioned landslide database has been received from MRT which includes the landslide locations since the 1950s. A total of 600 landslides were randomly selected; 70% of them were used as training data and 30% as validation data. The same number of non-landslide points were randomly selected from the free-landslide regions. Subsequently, values of 1 and 0 were assigned to landslide pixels and non-landslide pixels respectively. In order to perform DT, all dataset needs to be converted into ASCII (American Standard Code for Information Interchange) format. ArcGIS was used to convert all of the input data into ASCII data. Then, landslide training data and landslide conditioning factors were analyzed while using the DT method in the SPSS environment to calculate the landslide susceptibility index and build a andslide susceptibility map in the study area. Classes with the highest susceptibility were overlaid on risky features derived from different sources.

Decision Tree (DT)

DT is one of the machine learning methods that consider a predictive modeling technique. It can precisely identify the structural patterns in data and represent them graphically as tree structures. Another advantage of DT is that pre-defined correlation between the variables is not required (Saito et al., 2009). DT can explain data and use it predictively, it can also ingest data calculated at varying scales, purely on the non-linear relationship without the need for assumptions based on frequency distributions (Kheir et al., 2010). Consequently, each factor can be considered input into the model. DT has been used as a rule-based technique in numerous natural hazard studies (Chen et al., 2017; Jaafari et al., 2018; Tehrany et al., 2013). DT groups the landslide conditioning factors hierarchically according to levels of susceptibility. The aim is to create a set of decision rules that can form the basis for predicting the outcome from the input dataset. Thus, the rules are generated by the analysis of a set of conditioning factors, with the purpose of predicting an outcome from a similar set of variable factors. Due to the proficiency of DT, this method was used to analyze the correlation between the landslide conditioning factors and the training dataset. Using DT-CHAID the conditioning factor that is selected at each step is the one representing the strongest relationship with the landslide occurrence susceptibility.

Accuracy Assessment

AUC is a popular, comprehensive quantitative method of accuracy assessment, by which the prediction and success rates may be evaluated (Pham, Pradhan, et al., 2016). The proficiency of AUC in evaluating the susceptibility mapping outcomes has been demonstrated successfully in a number of studies (H. Pourghasemi et al., 2013; Pourtaghi et al., 2016; Xu et al., 2012). AUC evaluates the existence of the known landslide inventory data and the acquired probability map. It starts by dividing the landslide probability map into categories of equal area, and hierarchically ranking respective values from minimum to maximum in ArcGIS. AUC starts by sorting the calculated values of all cells into descending order, thus ranking each prediction hierarchically. Thereafter, the values of cells were divided into 100 classes with 1% accumulation intervals. The presence of landslide in each interval is measured using the “Tabulate area” tool in ArcGIS as the next step. The success and prediction curves determine the percentage of landslides in each probability category.

Results and Discussion

DT has been applied and a landslide susceptibility map has been created by classifying the derived map into five classes of “low”, ”very low”, ”moderate”, ”high”, and ”very high” (Figure 4) using a well-known quantile classification technique (Baeza et al., 2016). Based on the DT tree structure, the most influential landslide conditioning factors affecting the landslide distribution were geology and slope, as they were selected at the top of the branch. The most susceptible combination of conditioning factors contributing to the high landslide susceptibility was as follow: starting with slope (between 32-58°), as well as the decision root continued by the rainfall greater than 10mm, and NDVI <-0.1. Areas exhibiting these characteristics were classified as 100% susceptible to landslides (Table 1).

Table 1. The most susceptible combination of conditioning factors

Factors	Range	DT Rules
Slope	0-72°	32-58°
Rainfall	6.6-42.4mm	>10mm
NDVI	0-67°	<-0.1

The landslide susceptibility map is presented in Figure 4. It depicted where the slope failure may occur spatially in the future.

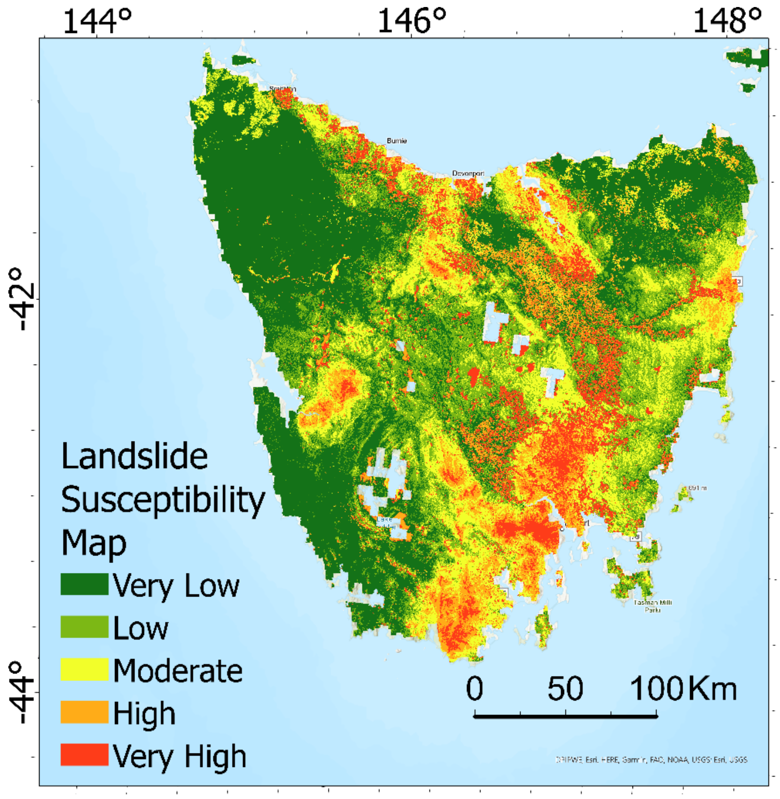

Figure 4. Landslide susceptibility map

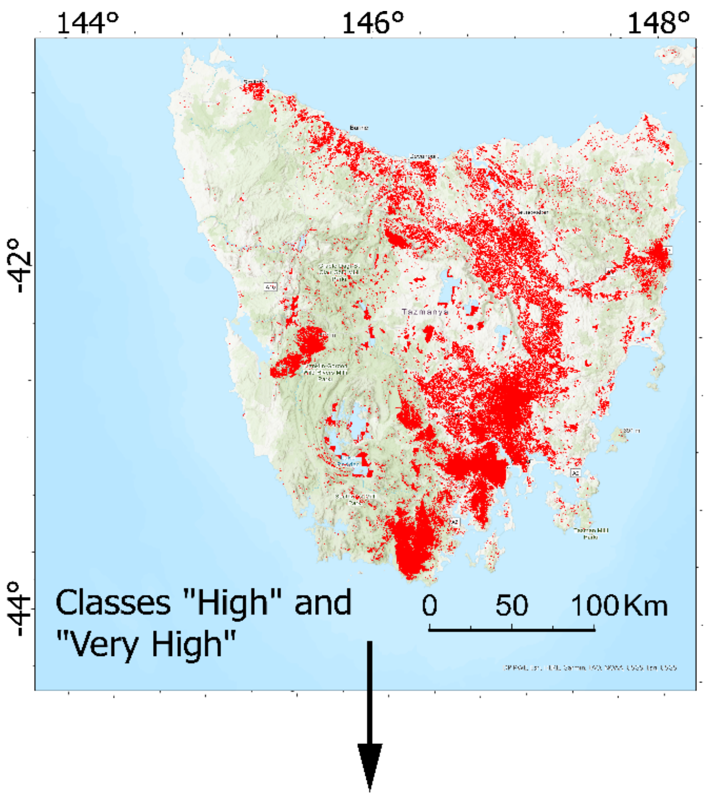

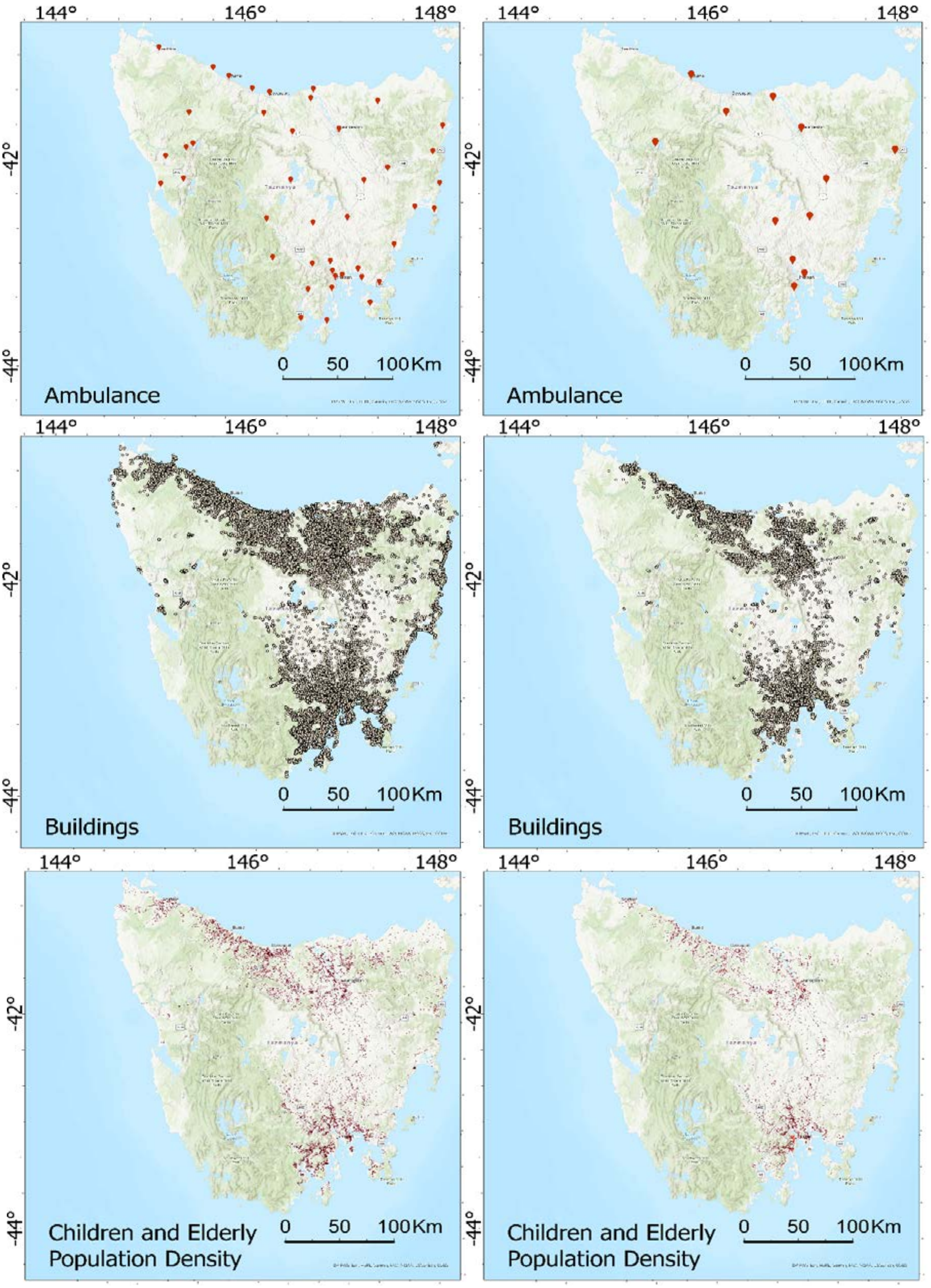
144°
146°
148°
-42°
-44°
0 50 100Km
Ambulance
144°
146°
148°
-42°
-44°
0 50 100Km
Ambulance
144°
146°
148°
-42°
-44°
0 50 100Km
Buildings
144°
146°
148°
-42°
-44°
0 50 100Km
Buildings
144°
146°
148°
-42°
-44°
Children and Elderly
Population Density
0 50 100Km
144°
146°
148°
-42°
-44°
Children and Elderly
Population Density
0 50 100Km

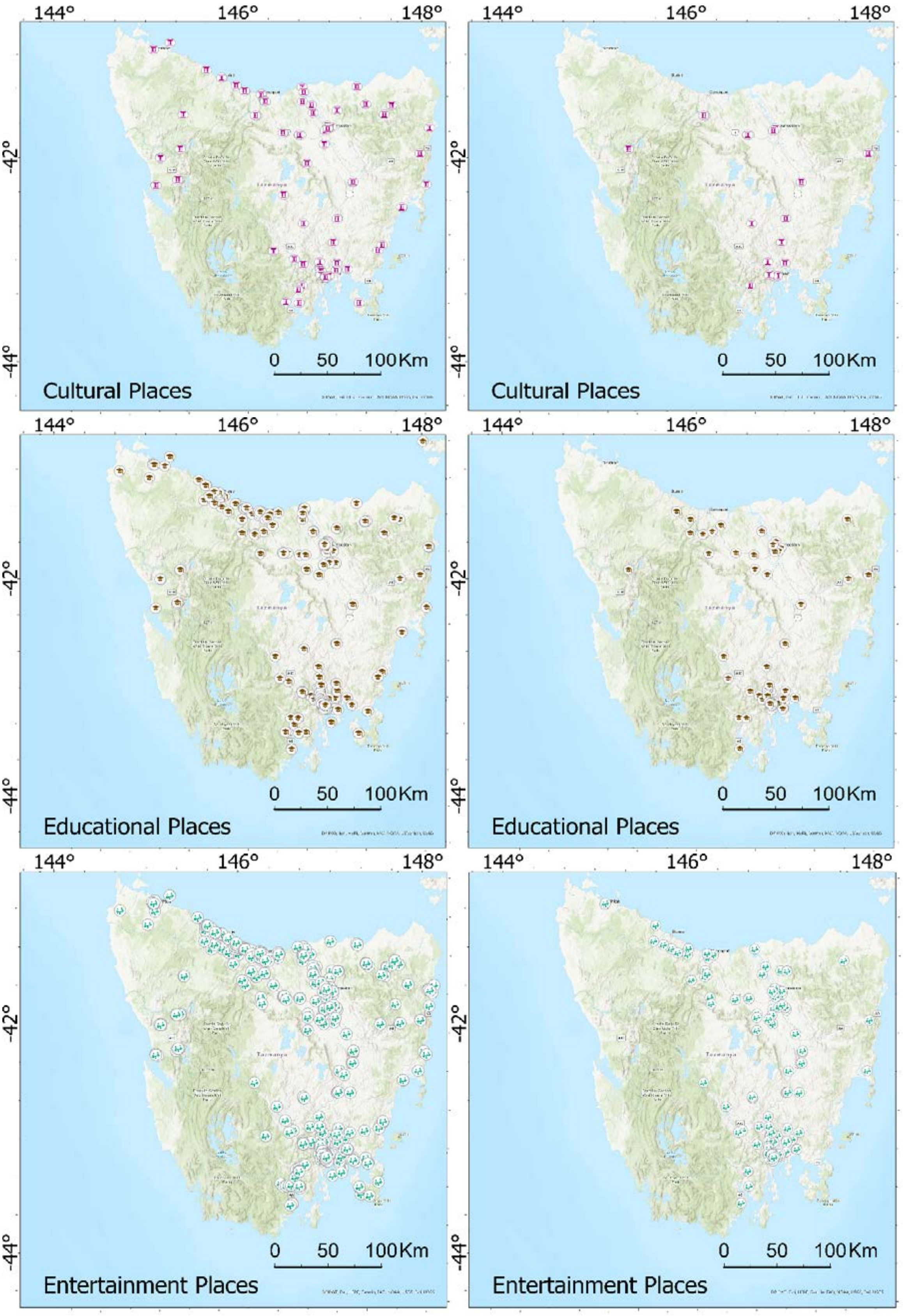
144°
146°
148°
-42°
-44°
0 50 100Km
Cultural Places
Cultural Places
Educational Places
Educational Places
Entertainment Places
Entertainment Places

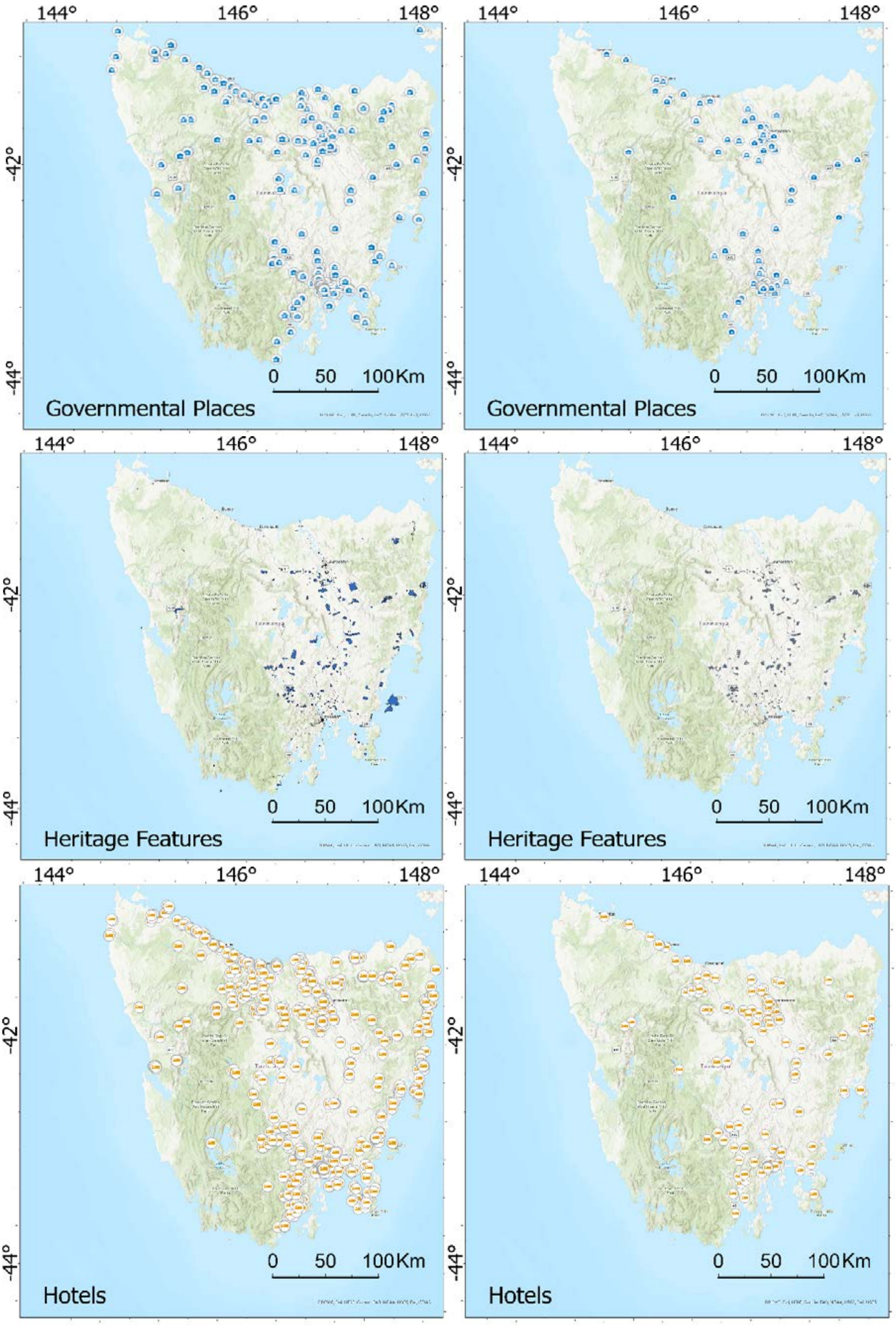
144°
146°
148°
-42°
-44°
0 50 100Km
Governmental Places
Governmental Places
Heritage Features
Heritage Features
Hotels
Hotels

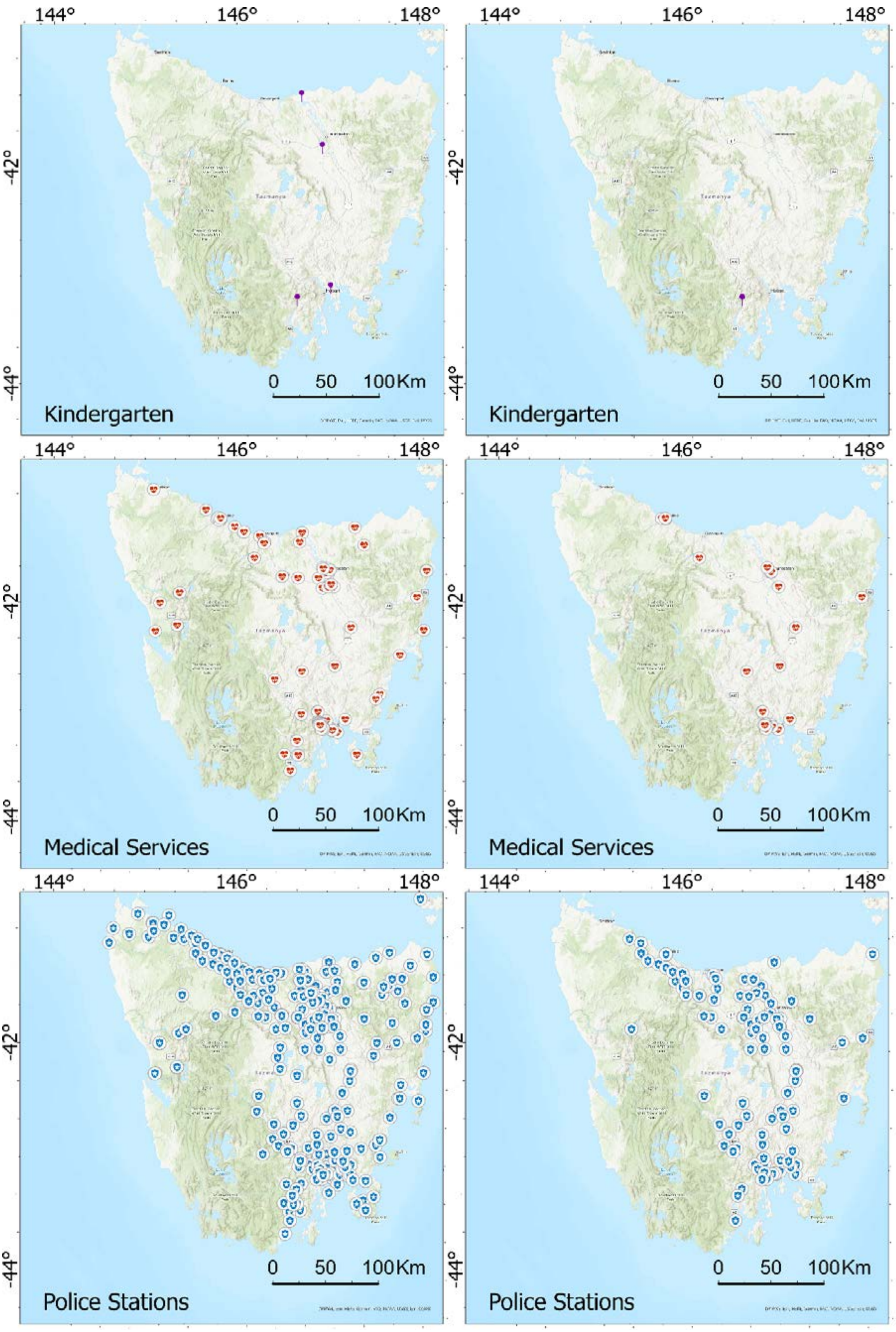
144°
146°
148°
-42°
-44°
0 50 100Km
Kindergarten
144°
146°
148°
-42°
-44°
0 50 100Km
Kindergarten
144°
146°
148°
-42°
-44°
0 50 100Km
Medical Services
144°
146°
148°
-42°
-44°
0 50 100Km
Medical Services
144°
146°
148°
-42°
-44°
0 50 100Km
Police Stations
144°
146°
148°
-42°
-44°
0 50 100Km
Police Stations

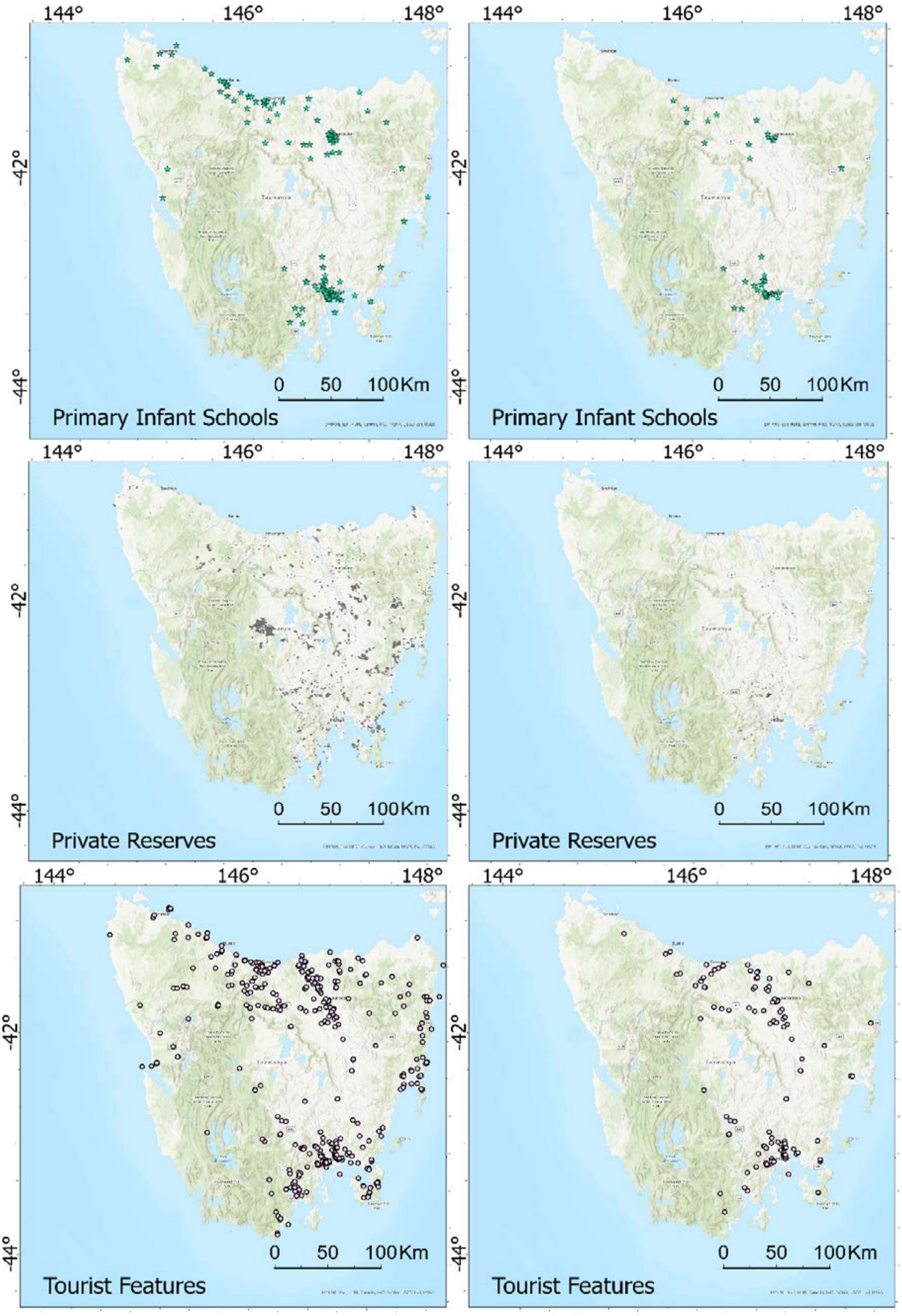

Figure 5. Risky features

As it can be seen in Figure 4, the majority of the susceptible areas are located southeast, center, and north regions. AUC has been applied and success and prediction rates were 87.64% and 84% respectively. In order to evaluate which features are at risk from these susceptible areas, overlay analysis has been implemented. The classes of “very high” and “high” have been used to be overlaid with ambulances, buildings, children and elderly population density, cultural places, educational places, entertainment places, governmental places, heritage Tasmania feature, hotels, kindergarten, medical services, police stations, primary infant schools, private reserves, and tourist features. Figure 5 represented the features that fall into the highest susceptible zones.

According to Figure 5, 142 touristic places; 39 primary and infant schools; 122 police stations; 45 medical services; Huonville Primary School Kindergarten; 210 hotels; 217 governmental places; 94 education places; 30 cultural places; 30% buildings; 12 ambulances; 186 entertainment places; 744 private reserves; and 2195 heritage features are located in highest susceptible zones. The derived output can considerably assist different sectors such as governments, insurance, tourism, and etc.

Conclusion

All societies are affected by natural hazards in one form or another. Whilst landslides do not present the most significant danger in Tasmania, the cost to the community over time from economic and social perspectives is considerable. This study aimed to evaluate the existence of risky features in high landslide susceptibility zones in Tasmania. DT as one of the robust machine learning methods has been used to evaluate the correlations among landslide conditioning factors and landslide inventory. Susceptible zones were detected and risky features such as hotels, children and elderly population, etc. have been overlaid with the produced map. Through this analysis, some risky features have been detected in classes of “very high” and “high” susceptibility. For instance, among all kindergartens in Tasmania, Huonville Primary School Kindergarten has been located in risky zones. From 291,698 buildings in Tasmania, 82,736 buildings have been located in risky zones. Such information can significantly be helpful in future management plans. It can be used as a basis for more detailed and deep risk assessments in Tasmania.

Scientific Ethics Declaration

The author declares that the scientific ethical and legal responsibility of this article published in EPSTEM journal belongs to the author.

References

Althuwaynee, O. F., Pradhan, B., & Lee, S. (2012). Application of an evidential belief function model in landslide susceptibility mapping. *Computers & Geosciences*, *44*, 120-135.

Baeza, C., Lantada, N., & Amorim, S. (2016). Statistical and spatial analysis of landslide susceptibility maps with different classification systems. *Environmental Earth Sciences*, *75*(19), 1-17.

Ballabio, C., & Sterlacchini, S. (2012). Support vector machines for landslide susceptibility mapping: the Staffora River Basin case study, Italy. *Mathematical geosciences*, *44*(1), 47-70. BAY, E. Landslide Map Series.

Chakraborty, D., & Anbalagan, R. (2013). Landslide hazard analysis and management: A case study from Nainital, India. In *Earth System Processes and Disaster Management* (pp. 141-154). Springer.

Chen, W., Xie, X., Peng, J., Wang, J., Duan, Z., & Hong, H. (2017). GIS-based landslide susceptibility modelling: a comparative assessment of kernel logistic regression, Naïve-Bayes tree, and alternating decision tree models. *Geomatics, Natural Hazards and Risk*, *8*(2), 950-973.

Chu, L., Wang, L.-J., Jiang, J., Liu, X., Sawada, K., & Zhang, J. (2019). Comparison of landslide susceptibility maps using random forest and multivariate adaptive regression spline models in combination with catchment map units. *Geosciences Journal*, *23*(2), 341-355.

Dai, F., Lee, C. F., & Ngai, Y. Y. (2002). Landslide risk assessment and management: an overview. *Engineering Geology*, *64*(1), 65-87.

Del Soldato, M., Bianchini, S., Calcaterra, D., De Vita, P., Martire, D. D., Tomás, R., & Casagli, N. (2017). A new approach for landslide-induced damage assessment. *Geomatics, Natural Hazards and Risk*, *8*(2), 1524-1537.

Hong, H., Miao, Y., Liu, J., & Zhu, A.-X. (2019). Exploring the effects of the design and quantity of absence data on the performance of random forest-based landslide susceptibility mapping. *Catena*, *176*, 45-64.

Jaafari, A., Zenner, E. K., & Pham, B. T. (2018). Wildfire spatial pattern analysis in the Zagros Mountains, Iran: A comparative study of decision tree based classifiers. *Ecological informatics*, *43*, 200-211.

Jain, P., Coogan, S. C., Subramanian, S. G., Crowley, M., Taylor, S., & Flannigan, M. D. (2020). A review of machine learning applications in wildfire science and management. *Environmental Reviews*, *28*(4), 478-505.

Jia, G., Alvioli, M., Gariano, S. L., Marchesini, I., Guzzetti, F., & Tang, Q. (2021). A global landslide non-susceptibility map. *Geomorphology*, *389*, 107804.

Kheir, R. B., Greve, M. H., Abdallah, C., & Dalgaard, T. (2010). Spatial soil zinc content distribution from terrain parameters: A GIS-based decision-tree model in Lebanon. *Environmental Pollution*, *158*(2), 520-528.

Korup, O. & Stolle, A. (2014). Landslide prediction from machine learning. *Geology Today*, *30*(1), 26-33.

Kumar, R. & Anbalagan, R. (2016). Landslide susceptibility mapping using analytical hierarchy process (AHP) in Tehri reservoir rim region, Uttarakhand. *Journal of the Geological Society of India*, *87*(3), 271-286.

Lee, S. (2005). Application of logistic regression model and its validation for landslide susceptibility mapping using GIS and remote sensing data. *International Journal of Remote Sensing*, *26*(7), 1477-1491.

Lee, S. & Choi, J. (2004). Landslide susceptibility mapping using GIS and the weight-of-evidence model. *International Journal of Geographical Information Science*, *18*(8), 789-814.

Lee, S., Ryu, J.-H., Won, J.-S. & Park, H.-J. (2004). Determination and application of the weights for landslide susceptibility mapping using an artificial neural network. *Engineering Geology*, *71*(3-4), 289-302.

Lee, S. & Sambath, T. (2006). Landslide susceptibility mapping in the Damrei Romel area, Cambodia using frequency ratio and logistic regression models. *Environmental Geology*, *50*(6), 847-855.

Mazengarb, C. (2005). *The Tasmanian landslide hazard map series: methodology*. Department of Infrastructure, Energy and Resources Hobart, Australia.

Mazengarb, C. & Stevenson, M. (2010). *Tasmanian landslide map series: user guide and technical methodology*. Tasmanian Geological Survey.

Meena, S. R., Puliero, S., Bhuyan, K., Floris, M. & Catani, F. (2022). Assessing the importance of conditioning factor selection in landslide susceptibility for the province of Belluno (region of Veneto, northeastern Italy). *Natural hazards and earth system sciences*, *22*(4), 1395-1417.

Merghadi, A., Yunus, A. P., Dou, J., Whiteley, J., ThaiPham, B., Bui, D. T., Avtar, R. & Abderrahmane, B. (2020). Machine learning methods for landslide susceptibility studies: A comparative overview of algorithm performance. *Earth-Science Reviews*, *207*, 103225.

Park, S.-J., Lee, C.-W., Lee, S. & Lee, M.-J. (2018). Landslide susceptibility mapping and comparison using decision tree models: A Case Study of Jumunjin Area, Korea. *Remote Sensing*, *10*(10), 1545.

Pham, B. T., Pradhan, B., Bui, D. T., Prakash, I. & Dholakia, M. (2016). A comparative study of different machine learning methods for landslide susceptibility assessment: A case study of Uttarakhand area (India). *Environmental Modelling & Software*, *84*, 240-250.

Pham, B. T., Tien Bui, D., Prakash, I. & Dholakia, M. (2016). Rotation forest fuzzy rule-based classifier ensemble for spatial prediction of landslides using GIS. *Natural Hazards*, *83*(1), 97-127.

Pourghasemi, H., Moradi, H. & Fatemi Aghda, S. (2013). Landslide susceptibility mapping by binary logistic regression, analytical hierarchy process, and statistical index models and assessment of their performances. *Natural Hazards*, *69*(1), 749-779.

Pourghasemi, H. R., Jirandeh, A. G., Pradhan, B., Xu, C. & Gokceoglu, C. (2013). Landslide susceptibility mapping using support vector machine and GIS at the Golestan Province, Iran. *Journal of Earth System Science*, *122*(2), 349-369.

Pourghasemi, H. R., Mohammady, M. & Pradhan, B. (2012). Landslide susceptibility mapping using index of entropy and conditional probability models in GIS: Safarood Basin, Iran. *Catena*, *97*, 71-84.

Pourghasemi, H. R., Pradhan, B. & Gokceoglu, C. (2012). Application of fuzzy logic and analytical hierarchy process (AHP) to landslide susceptibility mapping at Haraz watershed, Iran. *Natural hazards*, *63*(2), 965-996.

Pourtaghi, Z. S., Pourghasemi, H. R., Aretano, R. & Semeraro, T. (2016). Investigation of general indicators influencing on forest fire and its susceptibility modeling using different data mining techniques. *Ecological Indicators*, *64*, 72-84.

Regmi, A. D., Devkota, K. C., Yoshida, K., Pradhan, B., Pourghasemi, H. R., Kumamoto, T. & Akgun, A. (2014). Application of frequency ratio, statistical index, and weights-of-evidence models and their comparison in landslide susceptibility mapping in Central Nepal Himalaya. *Arabian Journal of Geosciences*, *7*(2), 725-742.

Reichenbach, P., Rossi, M., Malamud, B. D., Mihir, M. & Guzzetti, F. (2018). A review of statistically-based landslide susceptibility models. *Earth-Science Reviews*, *180*, 60-91.

Roodposhti, M. S., Aryal, J. & Pradhan, B. (2019). A novel rule-based approach in mapping landslide susceptibility. *Sensors*, *19*(10), 2274.

Saito, H., Nakayama, D. & Matsuyama, H. (2009). Comparison of landslide susceptibility based on a decision-tree model and actual landslide occurrence: the Akaishi Mountains, Japan. *Geomorphology*, *109*(3-4), 108-121.

Sim, K. B., Lee, M. L. & Wong, S. Y. (2022). A review of landslide acceptable risk and tolerable risk. *Geoenvironmental Disasters*, *9*(1), 1-17.

Slee, A. & McIntosh, P. D. (2022). History of slope instability in the Oldina plantation, Tasmania. *New Zealand Journal of Forestry Science*, *52*.

Sultana, N. & Tan, S. (2021). Landslide mitigation strategies in southeast Bangladesh: lessons learned from the institutional responses. *International Journal of Disaster Risk Reduction*, *62*, 102402.

Tehrany, M. S., Pradhan, B. & Jebur, M. N. (2013). Spatial prediction of flood susceptible areas using rule based decision tree (DT) and a novel ensemble bivariate and multivariate statistical models in GIS. *Journal of hydrology*, *504*, 69-79.

Xu, C., Xu, X., Dai, F. & Saraf, A. K. (2012). Comparison of different models for susceptibility mapping of earthquake triggered landslides related with the 2008 Wenchuan earthquake in China. *Computers & Geosciences*, *46*, 317-329.

Author Information

Mahyat Shafapourtehrany
Kandilli Observatory and Earthquake Research Institute,
Department of Geodesy, Bogazici University, 34680
Cengelkoy, Istanbul, Turkey
Contact e-mail: *mahyat.shafapour@boun.edu.tr*

To cite this article:

Shafapourtehrany, M. (2022). Exploring the risky areas due to landslide using decision tree analysis: case study. Tasmania, Australia The Eurasia Proceedings of Science, Technology, Engineering & Mathematics (EPSTEM), 18, 86-101.